LOW TEMPERATURE SHAPE MEMORY RECOVERY OF 3D PRINTED POLY(D,L-LACTIDE) NETWORKS: INVESTIGATING THE POTENTIAL FOR LONG TIME SCALE APPLICATIONS

ALBERTO DI BARTOLO

Submitted for the degree of Doctor of Philosophy

Heriot-Watt University
School of Engineering and Physical Sciences

August 2019

ABSTRACT

Shape memory polymers (SMPs) are materials able to retain a macroscopic deformed state until an external stimulus triggers recovery to the original geometry. Recent research on SMPs has shown how the recovery can be modelled *a priori*, so that an adequate thermal and mechanical conditioning can be imparted to obtain the desired behaviour. Whereas most applications of SMPs require the recovery process to be fast (seconds), it can be speculated that the right conditioning and the right chemistry of the material can promote a slow recovery behaviour (weeks). Such slow recovering SMPs could be exploited for tissue engineering applications. This field is constantly researching new *in vitro* strategies and processes that better mimic human tissues native environment and development, particularly by the use of polymeric scaffolds for three-dimensional cell culturing. Following the rationale of mimicking natural tissue development, it has been envisioned that a slowly expanding artificial microenvironment might promote the formation of an organised tissue. This strategy could be enabled by fabricating shape memory scaffolds and instructing the construct to slowly recover from a compressed state to the expanded one, with kinetic similar to the natural tissue growth. Furthermore, scaffold fabrication and shape memory properties, synergistically combine with the use of stereolithography 3D printing (STL). This additive manufacturing technology enables the production of 3D parts with complex geometries and microscale detail, making it the perfect candidate for the fabrication of microporous constructs. Additionally, STL printing results in highly crosslinked networks with innate shape memory properties.

Given the above considerations, it is the scope of this work to provide evidence of prolonged recovery kinetics – i.e. one week – of polymeric biomaterials suitable for the STL fabrication of porous scaffolds. This contributes the first investigation of its kind, independently from the field of application. The objective of this work is also to model the shape memory behaviour of the material through existing linear viscoelasticity approaches and predict experimentally observed behaviour during the prolonged recovery. The work will report the synthesis of the biomaterials and their formulation into photo-curable resins for STL printing, as well as the printing testing on a desktop and a professional apparatus.

Acknowledgements

Now that I can wrap-up the final version of my thesis and write this section, a lot of good people who have been close to me through these years come to mind. I will start by thanking my supervisor, Dr Ferry Melchels, who has been great to work with and has always offered full support and guidance. He even taught me how to make beer! Though I don't drink alcohol. I would also like to thank Dr Valeria Arrighi who generously allowed me to work in her lab, particularly at the beginning of my research, and later became my second supervisor.

Next, I thank all my colleagues from IB3. That's a lot of names so I won't really list them all, though there are a few special ones. Kyriakos Michail has been my breakfast buddy and my neighbour in the lab, which made things quite more interesting. Kerr Samson joined Ferry's group in my second year; he is such a nice guy, we had a lot of fun in the lab and supported each other, plus he likes good music so I didn't have to listen to K-pop in the lab. I should also thank Andrew McCormack, but I won't because I can't be bothered. Instead I will thank Ewa Guzniczak (the reader is advised to pronounce it as "goose-knee-chack") who has been always lovely to talk to and whose doodles are mesmerizingly relaxing. Thanks to Evangelos (Vangelis) Kanoulas who taught me at least three Greek sentences in four years. I will now be ungrateful and condense a few more names in this one sentence, so thank you to: Dean, Marta, Vaso, Matt, Hanna, Alfredo, Krystena, Ameya, Kate, Miguel, Allende, Cancan.

Also a big thank you is due to my friend Antonio who has been my flatmate since the beginning and I know since we were fourteen. Anna was also my flatmate for three years and a good friend as well.

Finally I will thank my parents, my brother and my dog for their support and encouragement. Thanks for all the kilograms of food you sent me!

Research Thesis Submission

Please note this form should be bound into the submitted thesis.

Name*:*			
School:			
Version: *(i.e. First, Resubmission, Final)*		Degree Sought:	

Declaration

In accordance with the appropriate regulations I hereby submit my thesis and I declare that:

1. The thesis embodies the results of my own work and has been composed by myself
2. Where appropriate, I have made acknowledgement of the work of others
3. The thesis is the correct version for submission and is the same version as any electronic versions submitted*.
4. My thesis for the award referred to, deposited in the Heriot-Watt University Library, should be made available for loan or photocopying and be available via the Institutional Repository, subject to such conditions as the Librarian may require
5. I understand that as a student of the University I am required to abide by the Regulations of the University and to conform to its discipline.
6. I confirm that the thesis has been verified against plagiarism via an approved plagiarism detection application e.g. Turnitin.

ONLY for submissions including published works

Please note you are only required to complete the Inclusion of Published Works Form (page 2) if your thesis contains published works)

7. Where the thesis contains published outputs under Regulation 6 (9.1.2) or Regulation 43 (9) these are accompanied by a critical review which accurately describes my contribution to the research and, for multi-author outputs, a signed declaration indicating the contribution of each author (complete)
8. Inclusion of published outputs under Regulation 6 (9.1.2) or Regulation 43 (9) shall not constitute plagiarism.

* *Please note that it is the responsibility of the candidate to ensure that the correct version of the thesis is submitted.*

Signature of Candidate*:*		Date:	

Submission

Submitted By *(name in capitals):*	
Signature of Individual Submitting:	
Date Submitted:	

For Completion in the Student Service Centre (SSC)

Limited Access	Requested	Yes		No		Approved	Yes		No	
*E-thesis Submitted (**mandatory for final theses)***										
Received in the SSC by *(name in capitals):*						Date:				

Inclusion of Published Works

Please note you are only required to complete the Inclusion of Published Works Form if your thesis contains published works under Regulation 6 (9.1.2)

Declaration

This thesis contains one or more multi-author published works. In accordance with Regulation 6 (9.1.2) I hereby declare that the contributions of each author to these publications is as follows:

Citation details	e. g. Author 1 and Author 2, Title of paper, Title of Journal, X, XX-XX (20XX)
Author 1	Contribution….
Author 2	Contribution….
Signature:	
Date:	

Citation details	e. g. Author 1 and Author 2, Title of paper, Title of Journal, X, XX-XX (20XX)
Author 1	Contribution….
Author 2	Contribution….
Signature:	
Date:	

Citation details	e. g. Author 1 and Author 2, Title of paper, Title of Journal, X, XX-XX (20XX)
Author 1	Contribution….
Author 2	Contribution….
Signature:	
Date:	

Please included additional citations as required.

Contents

Chapter 1 – Introduction

This Chapter presents an overview to the topics and motivations and to the findings and impact, of this PhD thesis. The objectives and hypotheses of the research work are defined and the undertaken approaches are briefly discussed.

1.1 Motivations to the research

Tissue engineering strategies are constantly evolving, assimilating new concepts, technologies and processes, native to engineering, material science and life sciences. Drawing from the spatially progressive nature of *in vivo* tissue growth, it has been hypothesised that providing a similarly dynamic, three-dimensional, scaffold microenvironment during *in vitro* cell culturing, might produce a more *in vivo-like* bioartificial tissue. The use of a shape memory polymer (SMP), as the scaffold bulk material, can be envisioned as part of the strategy to achieve such dynamic behaviour; where a compressed scaffold slowly expands, as shape recovery progresses. Still, there is no certainty that the SMP could be instructed to match the slow kinetics of tissue formation, as the majority of related research and applications, focus on fast shape recovery. Exact control and predictability of the shape memory behaviour is an additional requirement; this has been demonstrated through mathematical modelling of few materials, in the measure of shape recovery lasting up to one hour. Optimal control over the scaffold architecture would also be essential to the envisioned strategy. Modelling the shape memory response and the change in volume available to tissue growth, is much more reliably achieved when the tangible construct matches its intended, three-dimensional, design. Stereolithography 3D printing (STL) is the technology enabling such optimal control. STL can be exploited for the accurate fabrication of tissue engineering microporous scaffolds, displaying excellent design fidelity. Conveniently, polymeric materials printed through STL can be expected to display shape memory properties, as demonstrated by research on 4D printing.

The main motivation to this work is to demonstrate the prolonged (weeks) shape memory behaviour of a stereolithography printed polymeric biomaterial and to model such response through the application of linear viscoelasticity theory. This would deliver a first, fundamental, piece of evidence to support future research on the use of shape memory scaffolds as platforms to better recapitulate the dynamic, *in vivo,* tissue formation, during *in vitro* culturing. Furthermore, this study would contribute to the material science field the first experimental observation of prolonged shape recovery and

an investigation of the applicability of common linear viscoelasticity modelling to predict such long kinetics.

1.2 Objectives and hypotheses

Here, the main objectives and hypotheses of this research will be presented in a clear and concise way. Supportive evidence to the listed hypotheses will also be provided, as well as reference to existing research.

This research objectives are:

- Formulation of a photo-curable polymeric resin suitable for the stereolithography fabrication of biocompatible parts with shape memory behaviour;
- Conditioning the STL printed networks into displaying prolonged shape recovery of one week or longer, empirical observation of the behaviour;
- Modelling the shape memory behaviour of the networks by the use of linear viscoelasticity;
- Demonstrate the use of the developed photo-curable resin for the STL fabrication of parts with microporous architecture.

The main hypotheses to this work are:

1. Shape memory properties will be inherent to the STL fabricated networks;
2. Recently developed 1D linear viscoelasticity models for prediction of shape memory behaviour can be applied to the fabricated networks;
3. The shape recovery kinetics of the printed networks can be tailored from minutes to weeks through the thermo-mechanical history imparted to the material (programming) and the application temperature;
4. The influence of the programming on the recovery kinetic at a given recovery temperature, is limited. In particular, in terms of how slow the recovery can be made by changing the programming conditions.

Here I offer evidence and considerations with respect to the listed hypotheses:

1. Many polymeric materials can be instructed into exhibiting shape memory effect, the difference being in how well they perform this function. The ideal polymeric candidates have distinct transitions (glass or melting) and a crosslinked structure (chemical or physical)[1]–[3]. Because of the radical photo-polymerisation that is the basis of STL[4], parts obtained by this fabrication technology are amorphous and chemically crosslinked polymeric networks. This makes them very good candidates as SMPs with shape recovery activated by glass transition.

Research in 4D printing[5]–[7] is a clear demonstration of the shape memory effect obtained in STL printed materials.

2. The 1D linear viscoelasticity model taken as reference in this research was reported by Yu et al. in 2014[8]. The modelling should work for thermorheologically simple polymers[9]–[11] and at low imparted strain and it was applied to a photo-crosslinked acrylate based polymer. The STL printed networks are expected to be homogeneous, isotropic and amorphous, so that thermorheological simplicity applies; the testing will be performed at low strains.
3. SMPs retain the imparted deformation when kept at low enough temperature (fixed state) and start recovering once heated up. The time-temperature superposition principle[9]–[11] informs us that a viscoelastic behaviour over extremely long time at low temperature can match the behaviour at short time and high temperature. Analogously, one can look at the low temperature fixed state as a recovery process that proceeds over extremely long time. Increasing the recovery temperature reduces this time; it can be assumed that in doing so several slow recoveries might be unlocked, including one that fits our week criterion.
4. In reference to Yu et al. work[8], [12], [13] and viscoelasticity theory, the polymeric behaviour can be seen as resulting from the contribution of elastic and viscous components, that follow the generalised Maxwell model approach[10], [14]. The viscous parts contribute to the mechanical behaviour if the programming temperature is high enough for their viscosity to be low, if the programming time is long enough with respect to their relaxation time, or by a combination of the two. Two limit conditions can be identified: no deformation is stored by the viscous components; all deformation is stored by the viscous components. The second situation leads to the slowest recovery possible and any further increase in programming time or temperature has no effect. This is similar to what can be observed for the temperature memory effect of SMPs[13]. Additionally, we can consider that the reference work[8] showed that the value of shape fixity ratio is determined by the programming and that one value corresponds to one recovery behaviour. Since the ratio is bounded between 0 and 1, then follows that the recovery kinetics are bounded.

1.3 Note on methodology in use: tensile tests as opposed to compression tests

It should be noticed that this work made use of tensile testing methodologies for the material characterisation, including the shape memory experimental and theoretical

analysis. This is a limitation of this research work, since the envisioned application would work under compression. At the same time, the experiments required to characterise the material, from the thermo-mechanical point of view, are of dynamic nature. This means that an oscillating (sinusoidal) deformation is applied to the specimen, this is obtained by use of dynamic mechanical analyser. While this can done in compressive mode, it would not give good accuracy. This is because the machine cannot guarantee a good, constant, contact between the surface of the specimen under compression and the steel cylinder used to apply the oscillating deformation. On the other hand, the tensile set-up doesn't incur in these problems and, consequently, it is the typical testing methodology in use in literature. Furthermore, the specimens for compression testing need a certain cross-section area to work well with the machine. The machine can only produce a force of 18 N; given a glassy polymer (say modulus of 1000 MPa) and wanting to achieve at least a 10% strain, the maximum diameter would be 0.12 mm. This would not guarantee good contact with the machine and is not something easily fabricated. Additionally the shape memory testing includes steps at very low temperatures under isostrain conditions, this would not work well in compression as the specimen would undergo thermal constriction so that the contact between machine and material would be lost. To these considerations it should be added that given that this work focused on modelling from the experimental data obtained through dynamic analysis, favouring the methodology which produces the smoothest data is a logical decision.

Tests carried out outside of the dynamic mechanical analyser could also be considered for compression. At the same time, once the thermo-mechanical data is obtained through the use of tensile methodologies and a model is built on the obtained data, then any other experiment in use should follow a similar tensile set-up. Additionally, tensile states can be easily produced exploiting gravity and the strain and recovery for a film specimen are more easily monitored than for a compressed cylinder.

Finally, while tensile and compressive moduli (and other mechanical properties) are quantitatively different, the temperature-dependent response is not. For both strain conditions the shape recovery will have the same qualitative behaviour with respect to temperature. Interestingly, the one literature example that reports both tensile and compression shape recovery shows an almost identical strain change both qualitatively and quantitatively[15]. Additionally, one polymeric system first studied by Yakacki et al.[16], has been repeatedly used in shape memory research under both tensile and compressive strain. The exact material formulation might be slightly different and some parameters in the shape memory analysis vary, though it can be appreciated that the

experimental results of recovery are quite similar. For example, the results showed by Yu et al.[8] for recovery of a tensile strain are quite similar to the ones reported by Westbrook et al.[17] for the recovery of a compressive strain. What discussed is certainly not proof that the same similar behaviour will be shown by any given SMP, though it does support the assumption that a certain recovery obtained for tensile deformation can also be obtained for compressive deformation.

Given these considerations, the work was carried out by the use of tensile strain methodologies.

1.4 Main findings and impact of the research

In this work I demonstrated the shape recovery of photo-crosslinked networks of poly(D,L-lactide), over more than one week, when stored in unconstrained conditions at a temperature close to the onset of the glass transition of the material. The same networks were stored for up to six months at 20 and 37 °C and it was confirmed that they completely retain their deformation. I modelled the material through linear viscoelasticity and gave theoretical evidence that the shape recovery is not indefinitely influenced by modification of the programming conditions.

To the best of our knowledge, this is the only example of empirical research on the actuation of a shape recovery over such lengths of time. It is also the only example of linear viscoelasticity modelling that explicitly underlines the theoretical limit in the influence of programming on shape recovery.

Chapter 2– Background to the research work

This Chapter offers an overview to shape memory polymers research, linear viscoelasticity modelling of shape memory effect and stereolithography. Applications in medicine and tissue engineering are discussed and relevant references are provided.

2.1 Overview of shape memory polymers

The shape memory effect (SME) is the ability of a material to retain a deformed, temporary shape and recover to the original one in response to an external stimulus. Materials exhibiting this behaviour are a class of smart materials and referred to as shape memory materials (SMMs). The phenomenon can be observed in alloys, ceramics, polymeric systems or hybrids[3], [18], [19], with shape memory alloys (SMAs) being the SMMs most prominently studied to date. On the other hand, shape memory polymers (SMPs) have been receiving increasing interest in the last twenty years, as shown by the number of related publications and patents summarised in Figure 2-1. This interest arises not only from the stimuli-responsive behaviour, but from several desirable characteristics that are typical to many polymeric systems and that create the potential for applications in different fields. Most importantly, for biomedical applications, biocompatible and biodegradable SMPs can be fabricated [20]–[25]. Moreover, properties such as very high recoverable deformations[20], [26], [27] or high stress output during recovery[28]–[30] can be obtained by changing the polymer chemistry or by incorporation of nanoparticles. Tailoring the mechanical, shape memory properties and the geometrical design, can then lead to parts suitable for minimally invasive surgery[31]–[33] and clinical applications[34]–[36]. Polymers can also be designed as drug-eluting and drug-releasing systems, in addition to exhibiting shape memory behaviour[27], [37]–[39]. The polymers in use are, also, cheap (<10 $/lb)[2] and easily manufactured though a variety of techniques (from moulding to CNC machining and 3D printing), in addition to being light-weighted ($\sim$1 g/cm^3). Furthermore, different SMPs can be activated by application of different stimuli (e.g., heat, light, moisture, electricity, magnetic fields)[1]–[3], [40]–[45] which considerably contributes to their versatility. Most commonly the stimulus comes in the form of direct heating[2], [3], though indirect heating can be achieved by light irradiation (e.g. laser and IR)[35], [46]–[48], electric current[49]–[51], magnetic fields[52], [53]. Chemo-responsive polymers are also employed with some typical examples being SMPs responsive to water/solvents[54]–[58], pH[59], [60], redox reactions[61], [62]. Here we will focus on SMPs activated by direct heating, as it is the class we employ in our research and we will refer to them as thermo-responsive SMPs.

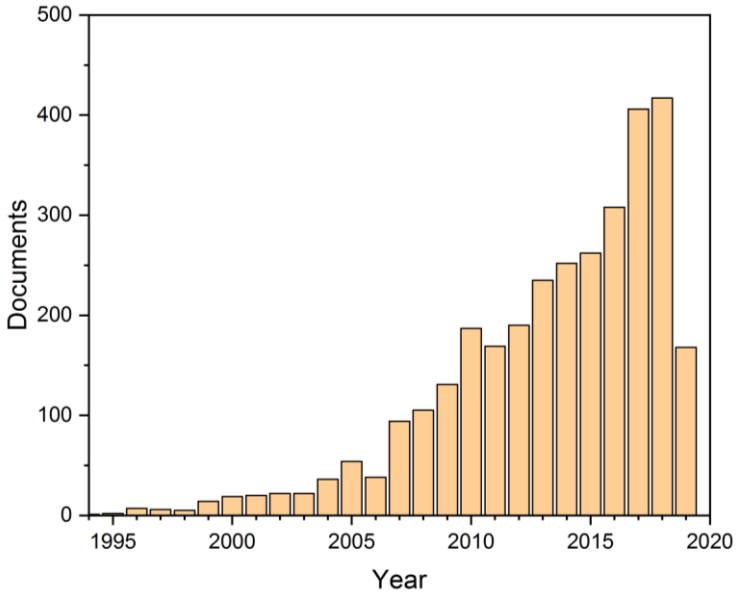

Figure 2-1 SMPs-related documents produced per year, from 1995 to early 2019.

2.1.1 Thermo-responsive SMPs: types and mechanics

Thermo-responsive SMPs will recover from the temporary shape to the permanent one upon heating to a certain transition temperature (T_{trans}). In a typical procedure, the SMP will first be deformed at a temperature above T_{trans} and subsequently cooled below T_{trans}, while the deformation is maintained, in order to fix the temporary shape. This step is normally called the programming step and sometimes the first part is referred to as the holding and the second part as the fixing steps. Upon fixing, the deformed state can be retained for a very long period of time as long as the material is maintained at low enough temperature. As already stated, the recovery can then be triggered by heating to T_{trans}. This transition temperature will depend upon the kind of polymeric system: typically, T_{trans} is either a glass transition temperature (T_g) or a melting temperature (T_m), respectively of amorphous or crystalline domains. From the SME point of view, the polymeric network of SMPs is usually described as made of netpoints and switching segments. The SME is then due to a duality, in the response to heating, of these different parts of the network. The netpoints are the parts that will not be affected by the thermal transition, therefore providing the three-dimensional stability required for the permanent shape to be "remembered" by the polymer. Both chemical and physical crosslinks can work as netpoints, though we can expect chemical crosslinks to display better thermal stability (because of the high energy required to break the covalent bonds). The switching segments, on the other hand, change their properties in response to the transition through T_{trans}. The change occurring can be summarised as a change in mobility, or flexibility, of the polymeric domains involved. Above T_{trans} these domains are flexible: they can be

oriented under an applied force and they can recoil from a deformed state towards the original one. Below T_{trans} their mobility is hindered and no change in conformation is possible, this allows for the deformed state to be locked in place. The driving force for the recovery mechanism can be addressed to the concept of entropy elasticity[3]. Specifically, the shape recovery is due to the entropy elasticity of the switching segments. A SMP in its rubbery state would assume the highest entropy conformation state, though when a strain is applied the polymeric chains will become oriented in the direction of the load, which results in an entropy loss. Since the polymer is cooled down under load, even after unloading the high entropy configuration cannot be regained. Once enough mobility of the switching segments is gained from the heating, the system will spontaneously move back to the highest entropy configuration.

As anticipated, depending on the polymeric system different type of netpoints and switching segments can be encountered. In reporting these differences it is convenient to follow some categorisation system for thermo-responsive SMPs. What we find most suitable for the present purpose is to categorise these SMPs on the basis of the nature of netpoints and switching segments, as already commonly found in literature[2], [3], [44], [63], [64]. The types of netpoints can be summarised in chemical and physical crosslinks, while the switching domains can be amorphous ($T_{trans} = T_g$) or crystalline ($T_{trans} = T_m$). A four class categorisation based on the different nature of crosslinks and phases, should serve the purpose of a brief review. Therefore we can identify: class 1 chemically crosslinked amorphous polymers, where $T_{trans} = T_g$; class 2 chemically crosslinked semi-crystalline polymers, where $T_{trans} = T_m$; class 3 physically crosslinked polymers, copolymers and blends, where $T_{trans} = T_g$; class 4 physically crosslinked semi-crystalline polymers, copolymers and blend, where $T_{trans} = T_m$. It should be noted that a crystal forming polymer could be potentially exploited as switching phase both through its glass transition and its melting transition.

The SMPs belonging to the first class are amorphous polymers and copolymers, they therefore display a glass transition behaviour around their T_g. While the chemical crosslinks provide the netpoints, the amorphous chains provide the switching mechanism. At temperatures above the glass transition, the polymeric chains have high mobility and can rearrange themselves under the applied stress. The deformation can be fixed by vitrification at low enough temperature (e.g., at T_g – 30 °C), the original shape can be recovered once the polymer is heated because of increased mobility and entropy elasticity. This class of SMPs has the advantage of its very good thermal stability and rubber elasticity, offered by the chemically crosslinked structure. Large deformations can also

be fixed and promptly recovered and the degree of crosslinking can be employed as a way to tailor thermo-mechanical properties such as moduli and T_g, resulting in better control over the shape memory behaviour. The main disadvantage is that, being chemically crosslinked, these SMPs cannot be reshaped or reprocessed once cured. Compared to the second class of SMPs, their memory response is also slower and the activation temperature can lie in a broad range, though these are not necessarily a disadvantage. For example Sharp et al.[65] investigated slow recovery rate SMPs, as actuators for implantation of electrodes into the brain. This class of SMPs can be obtained by different means of polymerisation in the presence of one or more monomers and macromers. In the vast majority of cases, a crosslinking agent is used to achieve the interconnected network. For example poly(ethylene glycol)dimethacrylate (PEGDMA) polymers with low molecular weight (300-1000 g/mol) have been frequently used as crosslinkers in the free radical polymerisation of acrylate and methacrylate monomers, to obtain crosslinked amorphous SMPs[21], [66]–[69]. Similarly, short reactive molecules can be used as crosslinkers, for example diethylene glycol diacrylate (DEGDA)[70] or dimethacrylate (DEGDMA)[67], [68]. By changing the concentration of crosslinker it is possible to tailor the thermo-mechanical properties of the polymeric network and therefore the shape memory response. Thiol-ene chemistries have also received attention for the synthesis of SMPs[71]–[73]. While acrylate and methacrylate systems are easily obtainable, cheap and have fast chain-growth polymerisation kinetics (acrylates being the most reactive), the thiol-ene step-growth polymerisation is not affected by oxygen inhibition and results in homogenous crosslinked networks that show much less shrinkage-induced stress after curing than the acrylate or methacrylate systems[72]–[74]. Epoxy-based SMPs belonging to this class are also commonly found in literature[15], [75] and commercially available. Polyurethane (and copolymers)[76]–[78] based SMPs are also typically found. Crosslinked networks can also be obtained from direct polymerisation of multi-functional macromers[79], without additional crosslinker.

The SMPs belonging to the second class contain crystallised domains characterised by a certain T_m, with crystallisation and melting of these domains being responsible for the switching mechanism. The deformation obtained at temperature above T_m is fixed by crystallisation below T_m, conversely, the recovery is activated once the crystalline domains are melted. This class of SMPs will typically show a sharper thermal activation than the ones from class 1, this is because the glass transition temperature range is generally broader than the one corresponding to the crystal-melt phase transition. Additionally, they might require longer time and slower cooling ramps in order to allow

the crystallisation process and successfully fix the deformed shape. The polymerisation routes followed in the synthesis of these SMPs are similar to the ones in use for the preparation of class 1 SMPs, as both classes are characterised by chemically crosslinked networks. Direct polymerisation of multi-functional macromers has been obtained for polycaprolactone (PCL) based SMPs[80], where the crosslinking was achieved through γ-radiation and the PCL provides a T_m around 55 °C; in a similar study PCL dimethacrylates were copolymerised (in the melt) by UV irradiation and the mechanical properties of the SMP were tuned by copolymerisation of n-butyl acrylate[81]. Thiol-ene chemistry was, again, employed for the crosslinking of macromers of diacrylated PCL and diallyl acrylamide poly(ethylene glycol)[82] and used for the preparation of shape memory foams with actuation around body temperature and high compressibility. Crosslinked polyurethanes can also be typically found in this category[83], [84], displaying almost completely recoverable elongations of up to 200%[83], at temperature 15 °C above T_m and very good retention of the deformed state when below T_m. Recently Li et al.[85] demonstrated shape memory activation at very high temperature for a series of polyamide (PA) thermosets, where the melt transition (~300°C) governs the SME activation. The chemical crosslinking was achieved by either introducing reactive groups on the polymeric chains ends (end-capped) or as side-groups. It was noticed that end-capped PA with M_n of 1000 g/mol resulted in two thermal activations, one because of glass transition at lower temperature and one because of melt transition at higher temperature. It is interesting to note that this behaviour can be tailored by increasing the average molecular weight to 3000 g/mol, which results in higher crystallinity degree, leading to the shape memory activation at lower temperature no longer being possible. Polycyclo-octene (PO) is another common example, where the crystalline part of PO undergoes melt transition around 60 °C and thermal crosslinking can be obtained by the use of peroxides[86]–[88].

The SMP belonging to the third class have physical crosslinks responsible for memorising the original shape and an amorphous phase that is responsible for the switching mechanism activated in proximity of its T_g. These SMPs are usually phase separated block copolymers, in which one block can form crystallinity or vitrified domains with a transition temperature T_{high}, higher than the T_g of the remaining polymer. Because of the thermoplastic nature of these SMPs, one advantage is that they can be reshaped at temperature higher than T_{high}. Copolymers and blends containing segmented polyurethanes can be commonly found in this class (as well as in the fourth class) [89]–[91]. Changing the concentration of soft segments (e.g. polycaprolactone segments) in

these polyurethanes can be exploited to produce different shape memory responses. For example, a polycaprolactone-based-polyurethane/phenoxy resin blend was prepared by Jeong et al.[89] were the soft segments of PCL in the polyurethane were miscible with the phenoxy, thus forming a phase with glass transition that could be exploited for the switching mechanism and that is separated from the netpoint phase formed by the hard segments in the polyurethane. The T_g could be tuned by changing the relative concentration of PCL and epoxy so that the recovery could triggered at different temperatures. Similar results were obtained for blends of poly(vinyl chloride) (PVC) and polyurethane[90], where once again phase-separation occurs between the phase of soft PCL segments and PVC (which are miscible) and the hard segments in the polyurethane. Copolymers of polyethylene (PE) and poly(methylene-1,3-cyclopentene) (PMCP) are an example of SMPs whose recovery can be activated either by the glass transition or the melt transition (in this case the two transitions are due to PMCP), as a result of the deformation being applied at certain temperatures[92].

The SMPs belonging to the fourth class are similar to the class 3 ones, though the switching mechanism is due to the presence crystalline phases with T_m lower than T_{high}. For example, multiblock copolymers of poly(L-lactide) (PLLA) and poly(glycolide-co-caprolactone) (PGC) are one example for this class of SMPs[93], where the PLLA form crystallinity with high melting temperature (120 °C ca.) while the PGC blocks offer the switching mechanism because of a low T_m tailorable by changing the composition. These SMPs in particular were thought for biomedical applications as all polymers in use have been abundantly studied for their biocompatibility and bioresorbability. In different studies, segmented copolymers of poly(ethylene glycol) (PEG) and poly(ethylene terephthalate) (PET), with physical crosslinks offered by the PET crystallinity and the switching domains offered by the PEG one[94], [95], display shape memory properties which can be varied by changing the PEG content. Polyurethane systems are also commonly found in related literature[96]–[100] since they consist of soft and hard segments (and usually extenders) that can be tailored in ratio to achieve different mechanical and shape memory properties. Kim et al.[96] presented an extensive study on a series of polyurethanes with soft segments of polycaprolactone (PCL), which can be exploited as switching segments due to its crystallisation and correlated the shape memory behaviour to both the length and the concentration of these segments in the polyurethane. Trans-polyisoprene (TPI) segmented urethane copolymers are similarly exploited to obtain shape memory behaviour, where the reversible phase is the crystal

domain of TPI while the hard segments are given by the urethane segments organising in spherulites[97], [98].

The majority of the reported polymeric systems with shape memory properties are able to store two shapes: the temporary and the permanent one. These kind of SMPs are therefore referred to as dual-SMPs. It is also possible to design the shape memory systems so that more than one temporary shape can be stored. These SMPs are usually referred to as multiple shape memory polymers (multi-SMPs)[45], [101], of which several examples can be found in literature[102]–[106]. Different ways to produce a multiple shape memory response have been reported in the last fifteen years. Probably the most intuitive approach is to design a polymeric system in which several thermal transitions coexist, so that an intermediate shape (or more) can be obtained at the lower transition temperature T_{low} and the original shape can be recovered at the higher transition temperature T_{high}. The different transitions can be, for example, the result of segregated crystallinity-forming domains with different melting points[107], or different glass transitions[108]. Furthermore, it has been observed that the multiple SME can be obtained in polymer networks characterised by broad glass transitions[101], [104], [109]. A broad glass transition relates to a large distribution of relaxation kinetics in the polymer network, such that at different temperatures belonging to the transition interval some kinetics would be already exhausted, others would start activating and the rest will not activate during the application time (nor, possibly, in decades). These SMPs can therefore store multiple temporary shapes because different kinetics become responsible for fixing and recovering different parts of the total deformation. The theory behind this kind of SMPs in particular, is strongly intertwined with the concept of temperature memory effect (TME), which will be discussed in the next paragraph.

Finally, it should be noted that, other than the polymers found in related literature, the shape memory behaviour can be expected in a multitude of researched polymers, blends, composites and so on. Of particular interest for our research, we can expect the SME to be inherent to parts obtained through stereolithography 3D printing, as this technique produces covalently crosslinked polymeric networks.

2.1.2 Shape memory polymers characterisation

SMPs are studied and conditioned into displaying a certain SME, by means of shape memory cycles (SMCs) which consist of a series of thermal and physical manipulations. In recent research the equipment used for SMCs is the dynamic mechanical thermal analyser (DMA), since it can impart strain, force and temperature controlled steps and

output continuous (1 data point per second) data. The SMC can be divided into two main stages, the first being the shape programming and the second the shape recovery. The aim of the shape programming is to deform and fix the material into the temporary geometry. When kept in the right conditions the SMP is then able to maintain this state for exceedingly long time. In the recovery step the material is then heated up to high-enough temperature for the permanent shape to be recovered. The material can be made to recover under no external force, in this case we will talk of free or unconstrained recovery. Conversely, enough force to maintain the deformed state can be externally applied to the material while heating up. This case is referred to as constrained recovery and provides information on the force that the material can exert against its environment during the recovery step. To summarise the entirety of the SMC, it is typical to refer to its Temperature-Strain-Stress 3D plot, similar to the representative one reported in Figure 2-2 (a). Additionally, a very straightforward visualisation of the SMC is the one reported in Figure 2-2 (b). From both schematics we can further discuss the SMC as made of four steps. In the deformation, or loading, step (1) the material is deformed to the maximum strain (ε_{max}) while kept at the temperature T_h. During this step the temperature can typically be high enough for the material to be in its rubbery state and therefore the stress required for the deformation will be low (e.g. <1MPa). The applied maximum strain can vary depending on the material; for example Voit et al.[26] reported a series of acrylate copolymers exhibiting recoverable strains of up to 800%. The loading is followed by the holding step (2), during which the deformation is maintained for a certain holding time t_h (while still at T_h). During the fixing step (3) the material is then cooled down to a certain temperature T_c – while still maintaining the strain – and held in isothermal conditions for a certain time (t_c). It should be noted that the stress, instead of the strain, can be maintained constant during the cooling step, though we find that isostrain cycles are more commonly adopted. In step (4) the material is then instantaneously unloaded, generally resulting in the loss of a certain amount of strain ($\Delta\varepsilon$). This phenomenon is usually referred to as bouncing back. The new strain $\varepsilon_0 = \varepsilon_{max} - \Delta\varepsilon$ is, therefore, the one at the beginning of the recovery process. The SMC ends with the recovery step (5) which, as discussed, could be unconstrained or constrained. During this step the material could be heated up to a certain recovery temperature (T_{rec}) and, henceforth, left to recover in isothermal conditions (as depicted in Figure 2-2 (b)), or could be constantly heated until full recovery is observed (Figure 2-2 (a)). To characterise the shape memory performance, two main parameters are extrapolated from the SMC data. The shape fixity, R_f, is mathematically defined as:

$$R_f = \frac{\varepsilon_0}{\varepsilon_{\max}} \quad (2.1)$$

Therefore, the parameter characterises the ability of the material to retain the prefixed deformation – or in other words the severity of the bouncing back – and assumes values between 0 and 1. SMPs that do not experience significant bouncing back, will be characterised by values of R_f close to 1. It should be noticed that the programming characteristics (programming temperatures and time but also heating and cooling ramps and strain ramps) have great impact on R_f and should be taken into account when evaluating the material performance.

The second parameter is the shape recovery ratio $R_r(t)$, which is a function of time (and temperature) defined as:

$$R_r(t) = 1 - \frac{\varepsilon(t)}{\varepsilon_0} \quad (2.2)$$

The parameter measures the percentage of recovered deformation with respect to the deformed state after the unloading. At time zero, the time at which the heating starts being applied, no deformation has been recovered and the recovery ratio is zero. As time goes by the strain will decrease and the value of $R_r(t)$ will grow. It should be noted that recovery ratio is a function of both time and temperature (the recovery process is a viscoelastic response, therefore inherently time and temperature dependent), though the temperature itself can be expressed as a function of time. Also, the value of R_r after a long time has elapsed is not necessarily equal to 1. Lower values can be due to part of the deformation not being recoverable and higher values can also be encountered as a result of thermal expansion of the specimen. In Figure 2-2 (c) and (d) we show examples of R_r and strain evolution under unconstrained and isothermal condition. Initially, the recovery takes a certain amount of time to activate and will later slow down as most of the deformation is recovered. Usually the initial time (time equal zero) is considered the time at which the heating starts being applied to bring the temperature from the cold one (used to store the part in the deformed state), to the recovery one. It is not unusual for the strain to initially increase near the onset of the recovery process, this can be addressed to the thermal expansion and results in an initial decrease of R_r to negative values. Furthermore, a certain percentage of retained strain at the end of the experiment can be observed, this translates into an ultimate value of R_r smaller than one.

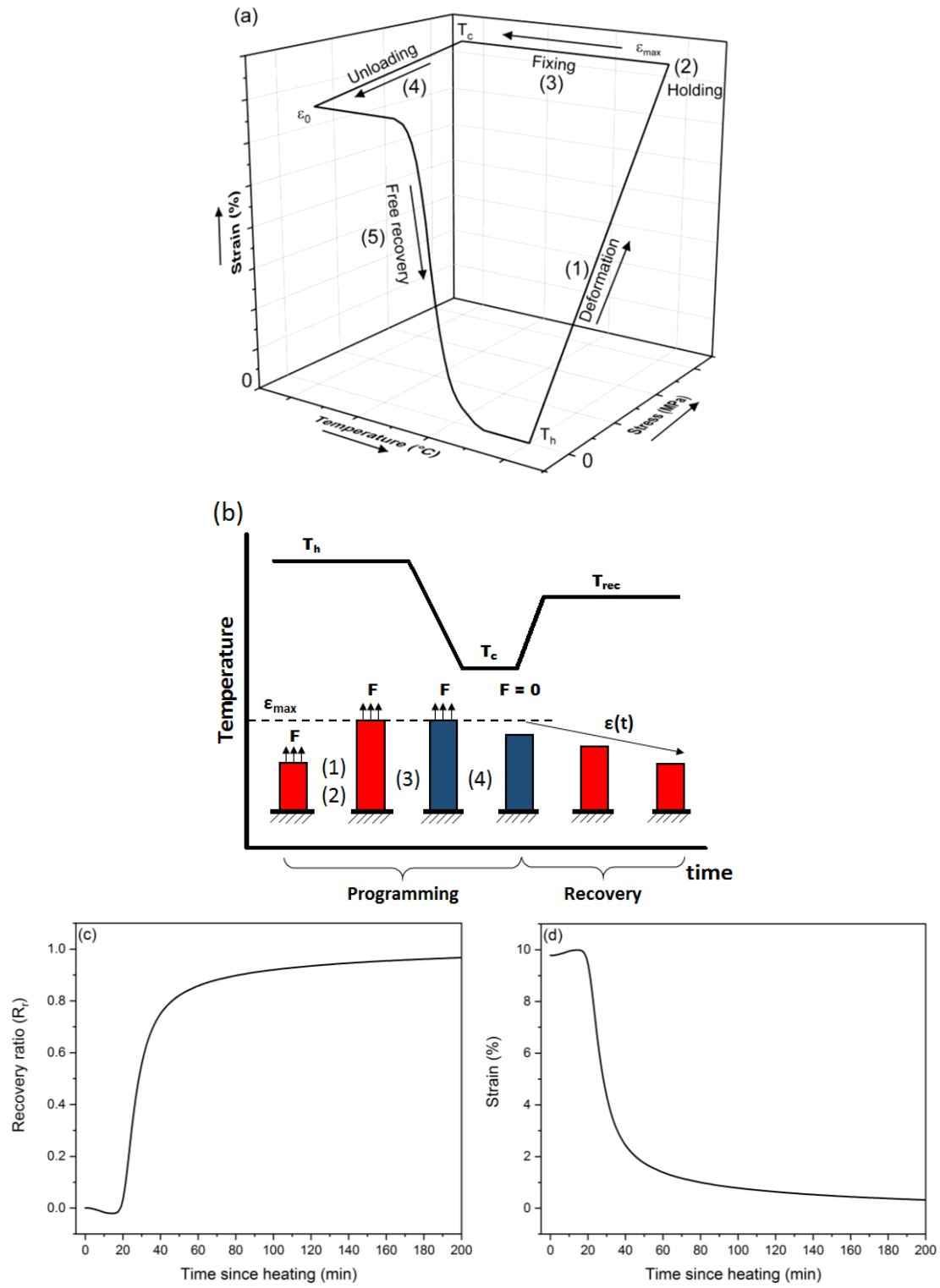

Figure 2-2 (a) Depiction of Temperature-Strain-Stress plot for a SMC. The plot assumes the cycle to be strain controlled so that the deformation is maintained constant during the fixing step, furthermore the depicted recovery is unconstrained and proceeds through application of a constant temperature ramp from T_c back to T_h. (b) Schematic of a SMC including the temperature evolution. In this representation the recovery takes place in isothermal condition. The numbers from (1) to (4) refer to the same steps depicted in image (a). (c) and (d) Respectively, example of shape recovery ratio and strain evolution during isothermal unconstrained recovery test.

As we noticed, the rate at which the recovery proceeds seems to go through a maximum. This recovery rate, or shape recovery speed, is usually calculated from the temperature derivative (non-isothermal recovery) or the time derivative (isothermal recovery) of the

strain and has been emerging as one important topic of investigation in SMP literature[13], [28], [110]–[112]. Furthermore, during constrained recovery testing, the stress produced by the material on the environment (the recovery stress) can be measured. These two parameters (recovery speed and recovery stress) are related to a relatively new phenomenon observed in SMPs and called temperature memory effect (TME), which was first (intentionally) described by Miaudet and Poulin[28] in 2007 for the recovery stress of CNTs-embedded poly(vinyl alchol) SMPs (for older literature where this observation could have been made, the reader is referred to Wache at al.[34]). Briefly, during non-isothermal recovery tests (i.e. a constant heating ramp is applied) the SMP displays its maximum strain recovery speed[28], [110], [112] or its maximum recovery stress[13], [28], [112] when close to the temperature applied during the deformation and holding process (T_h). The temperature corresponding to the maximum is referred to as switching temperature or shape recovery characteristic temperature (T_c), here we will prefer the latter nomenclature. More research showed that the validity of the TME seems to be relative to the SMC applied (other than to the polymeric system). In particular, Wang et al.[113] reported experimental studies on SMPs with broad glass transition region and noticed that a strain recovery TME could be observed only for deformation temperatures falling in the lower half of the glass transition (as defined from the temperature range of the tanδ curve obtained through DMTA analysis); any larger deformation temperature would result in the same T_c being obtained. During the same year Yu at al.[13] reported an experimental and modelling study on an acrylate SMP and demonstrated that its strain recovery speed T_c can be predicted by linear viscoelasticity modelling and time-temperature superposition, once the SMC conditions are set. Furthermore, they also observed that T_c is not affected by an increase in T_h once this temperature is larger than a certain value. Just like observed by Wang et al., this value falls in the lower half of the glass transition region, a few degrees lower than the polymer T_g and it could be predicted through the modelling. Furthermore the influence of heating rate was underlined and the influence of other programming conditions was discussed. In general it is accepted and demonstrated that the response of a SMP is affected by all parameters that characterise the shape programming. These include: the strain or force rate applied; the heat ramp applied during heating or cooling steps; the holding time and the fixing time; the holding temperature and the fixing temperature; the maximum applied strain or force. Undoubtedly, the parameters with largest influence are the holding time and holding temperature (t_d and T_d). The referenced work by Yu et al. on TME, was exploiting the theoretical framework developed during their research on modelling thermorheologically

simple SMPs. In particular they showed that the reduced holding time ($t_{r,h}$), obtained from the holding time and temperature t_h and T_h, can be used as the sole parameter determining the shape memory response. At the very least, this seems to be the case for the thermorheologically simple polymer in use in the paper. In paragraph 2.2 we will further discuss Yu et al. theoretical framework as part of the viscoelasticity to predicting the SME.

2.1.3 Biomedical research on SMPs and their use in medicine

Amongst SMMs, SMAs have been extensively studied in the past fifty or so years and find several applications, including clinical ones[19], [114]–[118]. In comparison, research on SMPs can be considered relatively new. A quick topic-search on Web of Science (© 2019 Clarivate Analytics) leads to 22,000 articles, reviews and proceedings, about SMAs and only 3,000 about SMPs (as of July 2019). Still, considerable efforts from several research groups have gone into better understanding the SME and, undoubtedly, the biomedical application topic has attracted a lot of interest from the scientific community. As we already discussed, SMPs present different appealing properties that can be exploited to obtain smart medical devices, deployable by minimally invasive surgery and that can potentially be resorbed in the body after fulfilling their function. Early research by Lendlein and Langer[20], [81] focused on investigating PCL-based biocompatible SMPs, later they patented a group of thermo-responsive SMPs characterised by linear degradability and underlined their potential as self-tightening sutures[119]. One possible advantage of this application is that the polymeric sutures could be programmed in a way that the most appropriate knot strength would be achieved, as both too tight and too loose suture points can result in medical complications. Around the same years, Metcalfe et al. carried out an *in vivo* study, in eight dogs, for a SM polyurethane foams (by Mitsubishi) used as self-deployable embolisation devices (for constructed carotid aneurysms). The material was found non-cytotoxic and non-mutagenic, the foam porosity allowed for cellular invasion and tissue formation, at the same time it could be inferred that some devices were not able to completely fill the aneurysmal cavity. This was, mostly, ascribed to the foam composition not being optimal. Modification of the polymer T_g was suggested as one way to achieve better results and diverse applications. Another polyurethane thermoplastic (also from Mitsubishi) was used for the fabrication of a mechanical thrombectomy device that could be delivered (through catheter) in its temporary rod-like form to the thrombus site and then activated by laser heating[35] to recover to its original, tapered corkscrew, shape, to capture and

remove the thrombus. The same year, the authors presented a similar study[36] where they synthesised a series of urethane systems, as the commercially available ones are not specifically designed for this biomedical application. For example, the commercial material was overheating near the optical fiber that connects to the device to give the light stimulus; conversely the heating was well distributed in the case of the custom material. In this case the optical properties were of great importance because of the type of actuation stimulus; furthermore the material displayed a sharp glass transition, which is ideal for fast actuation. In 2007 Yakacki et al.[67] reported the fabrication of a covalently crosslinked, acrylate-based SM cylindrical stent. The authors reported that the stents could be packaged in catheters with reduced thickness, so to enable less invasive surgery. They also showed that one polymer formulation could maintain a compressed state at room temperature for at least one month and then start recovering its original, uncompressed, shape when at body temperature. This specific composition resulted in a T_g of 55 °C and contained the minimal tested amount of crosslinking monomers. Both characteristics are important: the onset temperature for the glass transition cannot be too close to room temperature, in order to avoid premature activation and similarly the crosslink degree cannot be too high as this would accelerate the recovery from the compressed state even with low chain mobility available. Another interesting application is discussed and demonstrated by Bellin et al.[107], where a material displaying triple shape memory is formed into a cylinder that can be compressed into a temporary shape, recover towards an expanded intermediate geometry when at 40 °C and finally shrink to a third shape when at 60 °C. As the authors suggest, this kind of triple, non-unidirectional, shape memory properties could be exploited to fabricate stents that are easily deployed and easily retracted once their function has been fulfilled. Other examples for investigated biomedical applications include the use of SMPs as drug-diluting devices for the treatment of coronary artery disease[27], where elastomeric, hydrophobic, poly(caprolactone)-based polyurethanes were employed to achieve fast recovery and allow a slow release of lipophilic drugs and a slow degradation process. Finally, SMPs have been recently investigated for the fabrication of self-expanding scaffolds for tissue engineering. Zhang et al. proposed a photocrosslinked poly(caprolactone) based SMP as a self-fitting scaffold for treatment of maxillofacial geometrically irregular defects[120]. The material is pliable at temperature higher than the melt transition (>56 °C), which allowed fitting in geometrically irregular cavities, the stiffness and porosity where suitable for bone ingrowth and the construct was additionally coated with a bioactive layer to promote osteoblasts adhesion and proliferation. Liu et al. fabricated a series of

SMP porous scaffolds, also based on chemically crosslinked PCL and reported their *in vivo* use in mandibular defects of rabbits, where the use of SMPs was aimed at minimally invasive surgery. The cube-shaped porous scaffolds were prepared by sugar leaching, the constructs were compressed to 26%-33% of the original volume. The *in vitro* full recovery was observed in water after 60 seconds while it occurred after 10 minutes during *in vivo* experiments, this longer recovery was attributed to the different medium (water and air) and considered beneficial to allow more time for the operation to be performed.

Montgomery et al.[31] reported on the fabrication and application of a series of biodegradable SM scaffolds based on a chemically crosslinked elastomer, poly(octamethylene maleate (anhydride) citrate). In this case the SME was due to the micro-structure of the construct rather than to the polymer itself. The scaffolds were micro fabricated through a combination of soft lithography and injection moulding, to a size 1 cm × 1 cm × 0.1 mm and were used for the delivery of cardiac patches through minimally invasive surgery on rat and porcine models. Different scaffold designs were tested and the best ones could be inserted through a 1 mm orifice.

Other than potential applications, SMPs are, today, found in actual clinical products that are commercially available.

The IMPEDE®/IMPEDE-FX®[121] (Shape Memory Medical Inc.) series of endovascular plugs recently received CE mark and FDA 520(k) clearance. The devices are based on a polyurethane SM foam[122]–[124] that can be compressed and delivered to the affected site while in a rod-like shape and will quickly recover towards a porous, dome-like geometry, to occlude the aneurysm. The possible expansion ratio claimed for this foam 200% to 20000%, furthermore the activation can be achieved by multiple ways and the original patents covering the invention present a second SMP device that can be used to retrieve the first in the case of misplacement.

The ExoShape®[125] (CONMED co.) are a series of soft tissue fasteners (tibial and femoral) with FDA approval[126]. The devices are based on SM polyether ether ketone (PEEK) and are mostly employed in anterior cruciate ligament repair.

The same PEEK (PEEK Altera®) is used for the Morphix® suture anchors, produced by MedShape Inc., the same company that originally designed and obtained approval for the ExoShape. Similarly to the femoral ExoShape, this device comes in two parts, one having a set of shape memory wings that expand by 200% after insertion and ensure fixation.

The REMEDY^{TM}[127] (Kyoto Medical Planning Co., Ltd.) is a PLLA biodegradable stent for the treatment of peripheral arterial occlusions. It is the equivalent of the Igaki-Tamai^{TM} coronary stent, the first biodegradable (18-24 months) stent to be used in

coronary surgery[67], [128], [129]. The device is delivered in a (radially) compressed state; the expansion is initiated by the use of a warm balloon catheter (50 °C at the site), subsequently the mesh-like construct keeps expanding autonomously over 20-30 minutes, applying an adequate force to the vessel walls. The devices are CE approved, though only for the treatment of peripheral occlusions. Still, safety of use for coronary occlusions was corroborated by a ten-years study on 50 male Japanese men treated with the device[130].

2.2 Models to predict the SME

Modelling the shape memory effect is of fundamental importance to design any specific applications. Several research works have focused on this aspect, mostly adopting two approaches for the modelling of thermo-responsive SMPs: the phase transition approach[15], [131]–[134] and the viscoelasticity approach[8], [13], [135]–[140]. In the phase transition approach the SMP is considered as made of two separate phases: the active phase and the frozen phase. The volume fractions of the two phases are temperature dependent, in a way that near and above T_g the frozen fraction is converted to active fraction. Initial work making use of this approach was therefore modelling the glass transition as a time-independent thermodynamic transition. This produces, at times very considerable, errors, since the glass transition is typically a strongly kinetic phenomenon and in general it can be expected that the response of a material to a stimulus is time dependent. In more recent research this problem was addressed by introduction of a time-dependent factor for the frozen phase stress-release, which leads to improved prediction[133].

The viscoelastic approach makes use of combinations of the basic 1D linear viscoelasticity models made of spring elements, representing elastic responses and dashpot elements, representing viscous responses. The Maxwell model or the Kelvin-Voigt model[9] (Figure 2-3) are the typical starting points for the overall modelling and are expanded in different ways to try and encompass the rheological behaviour of the material.

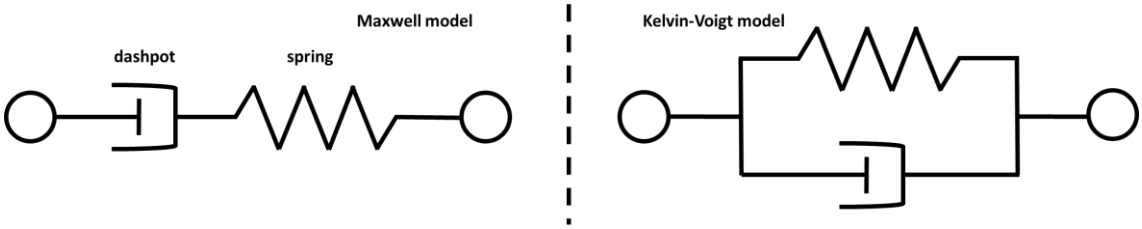

Figure 2-3 Maxwell and Kelvin-Voigt model are the two most simple models for viscoelastic materials. They comprise of one elastic part (spring) and one viscous part (dashpot) arranged in series (Maxwell) or parallel (Kelvin-Voigt).

Very often chemically crosslinked SMPs are modelled through the generalised Maxwell model (GMM), where one branch consists of one spring element and represents the rubber elasticity state while *n* Maxwell branches of spring and dashpots in series, represent generic *i-th* relaxation mode of the material, each characterised by constant elasticity moduli (E_i) and time-temperature-dependent viscosities (μ_i), though it is more convenient to consider the relaxation time of the branch $\tau_i = {\mu_i}/{E_i}$. for calculation purposes. The next paragraph will focus on further discussing this kind of modelling, as it is the one applied in our research. In concluding this overview we should also notice that recent research efforts aimed at unifying both modelling approaches, showing promising results.

2.2.1 Modelling the SME through the generalised Maxwell model and the time-temperature superposition principle

As already stated, the viscoelasticity modelling makes use of a combination of rheological models based on the spring and dashpot elements which are typically used to describe linear viscoelasticity. In addition the polymers modelled through this approach are T_g activated SMPs. In particular, the system first formulated by Yakacki et al.[16] has been extensively studied. Additionally the use of the generalised Maxwell model[14], [141] (GMM, also known as Wiechert model) is very commonly found to be successfully applied in related literature. Here, we wish to discuss this type of modelling, in particular in the form often found in Yu and Qi papers[8], [13], [138], [142], [143]. The theoretical framework behind the modelling comes from material science theory, for which we will offer some brief discussion and relevant references.

The GMM aims at describing the polymer viscoelastic response by use of one equilibrium branch and a series of non-equilibrium ones attached in parallel; the number of these branches is chosen following an "as-much-as-needed" approach, generally speaking more branches can better encompass the material viscoelastic behaviour but render the problem more computation-heavy. In Figure 2-4 we depict the GMM with one equilibrium branch and *n* non-equilibrium branches. The equilibrium branch consists of one spring and represents the polymer rubber elasticity behaviour, so that the elastic modulus E_{eq} is taken equal to the storage modulus in the rubbery plateau as obtained from dynamic mechanical analysis. This is the elastic contribution given by the crosslinked structure, which prevents the system from flowing when at high temperature (e.g. T_g + 25 °C). The non-equilibrium branches are each a Maxwell element, consisting of one spring and one dashpot in series. The *i-th* Maxwell element is described by the Hooke and Newton equations[9], [10] and by the resulting equation for the series arrangement:

$$\sigma_i = E_i \cdot \varepsilon_i^s \quad (2.3)$$

$$\sigma_i = \mu_i \cdot \dot{\varepsilon}_i^d \quad (2.4)$$

$$E_i \cdot \dot{\varepsilon} = \dot{\sigma}_i + \sigma_i/\tau_i \quad (2.5)$$

Where σ_i is the stress, which is the same for both the spring and the dashpot due to the series arrangement; ε_i^s and ε_i^d are the strain of the spring and the dashpot, respectively and their sum is equal to ε; τ_i is the relaxation time, i.e. μ_i/E_i; and the dot notation indicates the first order time derivative. The physical meaning behind these branches is usually not particularly discussed and the viscoelastic approach generally does not aim at achieving this, as opposed to the more meaningful concept of phase transition. A single Maxwell model can be taken as a fictitious representation of a material, analogously, the series of non-equilibrium branches can be taken as convenient, discrete, representations of chain relaxation dynamics, which overall manage to mathematically reproduce experimental data. Concerning the elastic moduli, including the equilibrium one, their summation ($E_{eq} + \sum_{i=1}^{n} E_i$) needs to equal the experimentally determined value of storage modulus for the polymer in its glassy state. This is because the dashpots viscosity at low temperature becomes too high for these components to have any impact on the overall mechanical response, which is therefore purely elastic. Concerning, the relaxation times, these give an indication of the time scale required for that dynamic to develop and go to completion; mathematically, τ_i is the characteristic time in all equations describing relaxation of that branch:

$$\sigma_i(t) = \sigma_i(0) \cdot exp\left(-t/\tau_i\right) \quad (2.6)$$

$$E_i^{relax}(t) = E_i \cdot exp\left(-t/\tau_i\right) \quad (2.7)$$

These are the equations describing the stress relaxation of the *i-th* non-equilibrium branch, which can be used to predict the decay in stress and relaxation modulus during a stress relaxation test. This is the case for most of the shape programming, since both holding and fixing are usually performed at constant strain. We can furthermore notice that, as already stated, the relaxation time is the characteristic time for these equations. In general we can expect that when the model is given a certain stimulus and the response is followed for a certain time Δt, branches with $\tau_i \gg \Delta t$ will contribute to the overall response in an elastic way, while if the relaxation time is of the same order or lower than Δt , the dashpot in the branch contributes to the mechanical response which is therefore viscoelastic. Similar outcomes are typically due to: an instantaneous stimulus, which does not allow time for the dashpots to relax; mechanical response at very low temperature, because the viscosity in the dashpots becomes extremely high. Usually the relaxation times of the

branches can be chosen in a convenient, arbitrary, way. For example, they are often taken *a priori* in a log-spaced order (e.g. 10^0; 10^1; 10^2) so that a large range of relaxation kinetics can be represented, without any of the branches being superfluous. We should now specify that these arbitrarily chosen values are the ones of the *reference* relaxation times and in doing so we should discuss how the temperature dependency is introduced in the model. This is achieved by the use of the time-temperature superposition principle (TTSP)[11], [14]. Briefly, some polymeric materials, known as thermorheologically simple, are characterised by a correspondence between the effect that time and temperature have on their viscoelastic behaviour, in a way that the material response over a long time at a certain temperature T_1 is the same as the response over shorter time at temperature $T_2 > T_1$. This means that the material response over inaccessible time scales can be studied over experimentally-feasible scale (say half an hour) by increasing temperature. The most common example of this principle is the construction of master curves that represent the, theoretically possible, evolution of a certain viscoelastic property over time lengths of years or much longer. This is achieved by repeating the same mechanical characterisation at different temperature values; the collected isotherms are then shifted horizontally with respect to one so that they superimpose one with each other forming a single master curve. The temperature corresponding to the reference isotherm is called reference temperature (T_{ref}) and the time axis (x-axis) in use needs to be logarithmic. The relaxation times that are chosen arbitrarily are the ones at the reference value of temperature and can be identified as reference relaxation times, τ^{ref}. The values at any other temperature can then be obtained from the reference ones, by applications of the TTSP through the equation:

$$\tau(T) = \alpha_T(T) \cdot \tau^{ref} \qquad (2.8)$$

Where $\alpha_T(T)$ is the shifting factor parameter function. Most typically this function is directly obtained by fitting experimental data collected during construction of a master curve. When performing the shifting of one isotherm of temperature T against the logarithmic time axis, the value of shift is defined equal to $-\log \alpha_T(T)$. The reference curve will therefore have shifting factor equal to one; the curves at higher temperature will need shifting to the right, which results in values of α_T between 0 and 1; curves taken at lower temperature will need shifting to the left, which results in α_T larger than 1. This gives a tabular collection of shifting factor and temperature values, which can be fitted by some mathematical equation. The most typical fitting equations for $\alpha_T(T)$ are the Williams-Landel-Ferry equation (WLF)[144], which is used when the temperature is

equal or higher than the T_g and the Arrhenius-type equation[11], [145]–[147], used below T_g:

$$\log(\alpha_T) = -\frac{C_1(T - T_M)}{C_2 + (T - T_M)} \quad \text{WLF} \quad (2.9)$$

$$\ln(\alpha_T) = -\frac{AF_C}{k_B}\left(\frac{1}{T} - \frac{1}{T_g}\right) \quad \text{Arrhenius-type} \quad (2.10)$$

Where C_1 and C_2 are material constants and positive; T_M is a reference temperature in use for the WLF equation, this is usually considered 10-15 °C below T_g; A is a material constant; F_c is the configurational energy[146]; k_b is the Boltzmann constant (~1.38×10^{-23} J/K); T_g is the glass transition temperature in Kelvin; T is the temperature. By fitting experimental data, e.g. making use of common software like Excel, one can obtain all the above unknown parameters. First guess values for C_1 and C_2 are usually taken as 17.44 and 51.6 °C, which are found to work well for several polymers when T_M is taken equal to T_g[144]. From SMP literature, the value of $-AF_C/k_B$ is usually around tens of thousands and has the dimensions of Kelvin (K). This set of equations (2.8, 2.9 and 2.10) is used to mathematically describe the temperature dependency of the system. We can complete the 1D linear thermo-viscoelastic description of the material by making use of all previous equations and considering the GMM arrangement. Since all branches are in parallel the total strain in each *i-th* non-equilibrium branch (ε_i) is equal to the strain in the equilibrium branch (ε_m), additionally for the stress calculation the modelling makes use of the Boltzmann's superposition principle[11], [141] so that the total stress of the system is taken equal to the sum of the stress in each branch. Therefore we correlate the stress and strain evolutions as:

$$\sigma(t) = E_{eq}\varepsilon_m(t) + \sum_{i=1}^{n} E_i\varepsilon_i^S(t) \quad (2.11)$$

Where the generic *i-th* branch has elasticity modulus E_i and elastic strain (strain in the spring element) ε_i^S and therefore is characterised by a stress equal to the product. In order to predict the shape memory behaviour, one needs to solve the strain evolution for each branch. The mathematics for each different step in a typical shape memory cycle is described in Chapter 8. Here we will report that the equations to be solved are usually exponential decays describing stress relaxation phenomena, in isothermal or non-isothermal conditions and that the strain evolution during free recovery at a certain temperature requires the solution of a system of *n* differential equations, where each

equation describes the strain function in one of the non-equilibrium branches and can be written in the form:

$$\varepsilon_i^s(t) = \int_0^t \left[\frac{d\varepsilon_m}{dt}(s) \cdot exp \int_s^t -\frac{dz}{\tau_i(z)} \right] ds \qquad (2.12)$$

Where *t* is a certain time point, *s* and *z* are dead variables for integration over the time interval [0 *t*] and τ_i is the relaxation time of the branch. Once the system of equations is solved, the total strain evolution is obtained from Eq.2.11 with $\sigma(t) = 0$, given the free recovery condition.

In applying this model to their acrylate polymer, Yu et al.[8] also showed, both theoretically and experimentally, that the influence of the holding time and temperature (t_h and T_h) over the shape fixity and the free recovery behaviour can be predicted by considering the reduce programming time. The reduced time itself is a non-physical time used during application of the TTSP and is calculated from the physical time and the shifting factor function as:

$$t_r = \int_0^t \frac{ds}{\alpha_T(T)} \qquad (2.13)$$

Where t_r is the reduced time corresponding to a certain physical time t. During the programming holding step the material can be expected to be already at thermal equilibrium before the deformation is applied, therefore the reduced programming time is simply the ratio of t_h and the value of shifting factor at the temperature T_h, meaning $t_r^h = t_h/\alpha_T(T_h)$. What was noticed is that the same reduced programming time will result in the same shape fixity and in the same recovery behaviour. We can notice that the reduced programming time is more exactly defined as the summation of the reduced times calculated for each programming step. Though it is very likely for all steps except the holding to be negligible since at low temperatures the values of shifting factors are very large. Additionally, we can notice that changing the holding temperature has much more influence on the reduced programming time than changing the physical holding time.

Furthermore, Yu et al. discuss how the same reduced programming time results in the same stress condition in the non-equilibrium branches, before the beginning of the recovery process. This internal stress regime is the driving force for the recovery process. Different stress-strain conditions in the Maxwell elements can result in faster or slower recoveries. One particular to notice is that, because of the viscoelastic nature of the model, the strains in the spring elements can be opposite to the main strain. For example,

the strain condition for the overall model can be tensile but the springs in the non-equilibrium branches can be under compression. If we consider the generic Maxwell element, when the holding temperature in particular is quite high (relatively to T_g), the dashpot is characterised by very low viscosity; this means that the entirety of the deformation during programming can be taken by the viscous component, while the spring is left at zero strain. After fixing the deformation, the unloading step will cause the SMP to lose a typically small amount of strain. The mechanical response to this stimulus can only come from the elastic components because the unloading is instantaneous and, furthermore, the fixing temperature is low, causing high viscosity and long relaxation times to characterise the dashpots. Therefore those springs that were in zero strain condition will be compressed by the unloading, while the others will lose tensile strain. The amount of strain change is the same for all springs, which is the $\Delta\varepsilon$ that determines shape fixity. The value can be calculated by solving the stress equilibrium right after unloading, which gives:

$$\Delta\varepsilon = \frac{E_{eq} \cdot \varepsilon_m + \sum_{i=1}^{n} E_i \cdot \varepsilon_i^s}{E_{eq} + \sum_{i=1}^{n} E_i} \tag{2.14}$$

This equation shows that the bouncing back is proportional to the stress right before unloading and inversely proportional to the glassy modulus. As a matter of fact, it is generally known that a material with high glassy modulus can make for a good shape fixing polymer[96]. With knowledge of this strain change, the stress-strain regime in all branches of the model can be determined. The evolution of this regime during free recovery is clearly more complicated and, as seen, takes the form of a system of coupled differential equations. The considerably different relaxation times of the branches result in the dashpots with higher relaxation time being able to retain their strained condition until the late stage of recovery while the ones with shorter relaxation will lose their strain in the early stages. Furthermore, as one branch relaxes, its stored aliquot of stress is partially redistributed to the next branches in order of increasing relaxation time. The complete stress-strain evolution will depend on programming and recovery conditions, though we can expect to encounter branches whose stress will just decay to zero, but also branches whose stress will go through an absolute maximum before decaying. Similarly, we can envision springs that will reverse their strain state (e.g. compression to tensile), before decaying to zero strain[12].

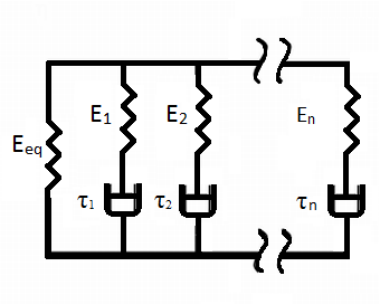

Figure 2-4 Generalised Maxwell model with n non-equilibrium branches and one equilibrium branch

2.3 Stereolithography 3D Printing

Stereolithography (STL) was the first additive manufacturing (AM) – nowadays typically referred to as 3D printing – technology to be developed[4], [148], [149]. Just like other AM techniques[148], STL is, in its essence, a well-controlled fabrication of a 3D part enabled by sequentially creating and joining together thin cross-sections of the final object. This is usually referred to as a layer-by-layer process, where each cross-section is one printed layer. The general process of printing a part by STL can be summarised in a few steps that are common for most 3D printing techniques.

- First a CAD design of the part to be printed is obtained. This could be an original design, but also achieved by imaging techniques, e.g. an MRI or CT scan;
- The CAD file is converted to a format that can be read by the printer, typically a ".stl" file;
- The printing settings are chosen, for example, the layer thickness and velocities for several mechanical movements;
- The printing is started and the part is built. Most commercially available machines and printing materials are well-optimised, so that the printing process does not require the user supervision.

The most evident difference between 3D printing techniques, is found in the way the layers are actually created. Figure 2-5 shows a schematic for a generic stereolithography apparatus. In STL, a photosensitive liquid resin is cured into a solid layer by spatially controlled light irradiation. The resins consist of reactive, low M_w, polymers and monomers, diluents that are typically also reactive, photoinitiators and UV-absorbers.

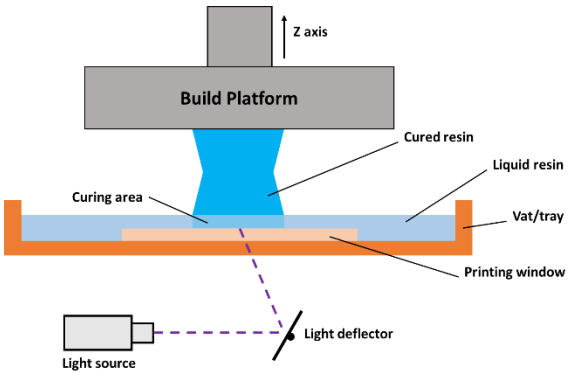

Figure 2-5 Schematic of stereolithography apparatus. This is today the most common set-up, where the light is irradiated through a transparent window and is usually referred to as top-down setup.

Curing proceeds through photo-initiated radical polymerisation, so that the final object is one highly crosslinked polymeric network. The resin is contained in a vat equipped with an optical transparent window and the light is irradiated from underneath the window. At the beginning of the printing a metal platform, the build platform or build head, is lowered into the vat and flushed to the window, so that the first printed layer can adhere to it. In the following printing the build-head is moved upwards by a certain Δz and each new layer is printed on top of the precedent one. This Δz is equal to the layer height and can be typically as small as 10 μm with no significant error. The described printing set-up is probably the most typical in nowadays printers; the alternative version works by projecting the light from above the resin vat and with the building platform getting lowered and submerged into the liquid at each new layer iteration. The part obtained right after printing is usually referred to as "green part" and generally it is not the final product. When one layer of resin is cured into a solid not all of the reactive species will be able to convert into the polymeric network. This is mostly because as the cured network is formed and the reaction environment becomes more and more solid, the mobility of the different compounds will decay, preventing them from interacting with each other and causing the curing to become diffusion-controlled. Therefore the green part will require post-processing, which comes in the form of additional curing inside a UV-box so that the overall conversion of reactive species to network can be increased.

The resin illumination during printing is obtained through three main approaches. One is the use of digital light processing (DLP) projectors, which resulted in the terminology DLP stereolithography. In these devices a projector irradiates light on top of a chip formed by millions of micro-mirrors that can be selectively tilted in on and off positions. The chip is commonly known as a digital micromirror device, DMD. DLP printers will work by illuminating a whole area of resin with a light pattern that corresponds to the cross-section to be printed; this is controlled by the selective actuation of the micro-

mirrors. Usually the size of the single pixel of projected light can be referred to as XY resolution, which primarily depends on the DLP resolution and the DMD features. It is typical to find relatively cheap DLP printers (3000-6000 £) with XY resolution of 50×50 μm. The resulting printed object is formed by millions of voxels with cross-section of 50×50 μm^2 and thickness determined by the layer height.

The second illumination approach consists of the use of a laser scanning system, where two galvanometers to rapidly draw a laser beam across the resin to cure the desired layer. This is typically referred to as stereolithography or typically SLA (which here refers to the technology but also stands for stereolithography apparatus), as it is the most similar to the original technology devised by Hull[4], [150]. The resolution of this technology can be intended as the minimum laser spot size, this can be typically around 100-150 μm for many desktop printers.

The third approach is known as mask stereolithography (MSLA). This technology makes use of a light array as the light source and a digital mask to shape the area to be printed. Typically the light array is an LED and the mask is an LCD photomask, which can be seen as an array of pixels that can be digitally activated in order to block or let the light pass. For these systems the XY resolution is therefore resulting from the photomask resolution, meaning from the size of the pixels.

Generally, all three types of stereolithography can be considered as the most accurate form of 3D printing; they enable the production of quite complex geometries with sharp detail in the 100 μm range. The noticeable exception to this is two-photon polymerisation (2PP)[148], [149], which is typically classified as a stereolithography technique (2PSL), though its nanoscale accuracy (100 nm or better) and its considerable higher cost, place it in a different league.

Another fundamental part of STL is the resin in use, this determines several parameters of the printing, for example the amount of light energy that needs to be provided for curing each layer. As previously explained, STL resins consist of several reactive moieties and photo-sensitive compounds. In the last two decades several commercial resins have been developed, following the increasing commercialisation of desktop STL printers. Similarly, different research groups have been working on photo-sensitive resins for 3D printing, adopting different kind of polymers and aiming at different mechanical properties. Most noticeably, in bioengineering related fields, we find research on poly(D,L-lactide) and copolymers[151]–[153], poly(ε-caprolactone)[154], [155], poly(ethylene glycol)[156], [157], trimethylene carbonate polymers[158]–[162], poly(propylene fumarate)[163]–[165], polyurethanes[166], polymers that are typically

studied for possible biomedical applications and therefore good candidates to be translated into the stereolithography-enabled fabrication of geometrically complex constructs like porous scaffolds for tissue engineering or even patient-specific parts. From the mechanical point of view, some efforts have gone into formulating resins with good flexibility; some of the reported research works feature the use of resins that can result in elastomers[153], [154], [160]–[162], [167] and make use of low-T_g polymers or copolymers, additionally to combining oligomers of different molecular weights to tailor elasticity and toughness of the material. Many elastic resins are also appearing more and more on the market, for example the ones commercialised by Formlabs or Henkel.

For the correct reproduction of the desired design, it is fundamental to have knowledge of the photo-curing behaviour of the resin in use, with the printer in use. The characterisation of such behaviour is usually carried out in a very empirical way by plotting a working curve. This is the trend-line fitting a collection of data points of the thickness of a cured layer of resin against the curing time. This is typically achieved by covering an optical transparent, thin, microscope slide with abundant resin, placing it on the printing window and projecting the light once with a certain exposure time. Typically, the working curve will have the formula:

$$C_d = D_p \ln\left({}^{E_0}/_{E_c}\right) \tag{2.15}$$

Where C_d [μm] is the cured depth, the thickness at which the resin is cured to the gel point; D_p is the penetration depth, a parameter that characterises how far the light can travel through the resin before its intensity drops to negligible values; E_0 [mJ/cm^2] is the energy dose received at the surface where the light enters the resin and is calculated from the power of the light source and the exposure time; E_c is the critical energy dose for an infinitesimal thickness to be cured, therefore equal to the minimal energy required to cause gelation. This equation relates to the Beer-Lambert law[150] of exponential absorption of light traveling through a medium so that we can write:

$$I(z) = I_0 exp\left({}^{-z}/_{D_p}\right) \tag{2.16}$$

Where I(z) is the irradiance at a certain depth z calculated from the point at which the light enters the resin, where it takes the value I_0. Therefore, D_p is often considered as the inverse of the absorption coefficient, though we will later discuss why this is an ill-posed definition. The value can still give an indication of the characteristic depth at which the light irradiance has decreased to 37% (1/e) of its initial value. This also means that we can consider $4D_p$ as the upper limit of printable layer thickness[168]; due to the exponential decay any further curing becomes extremely slow. Additionally, the lower

limit for printable cured thickness can be considered to be more or less equal to D_p, because at this thickness the green part is strong enough to withstand the printing process. Therefore, to be able to print at low layer thickness, enabling smaller features to be obtained, one needs to reduce the value of D_p. The most effective way to achieve this is by changing the composition of the resin, in particular the species that have the greatest effect on D_p are the ones that absorb light the most: the photoinitiator (PI), which absorbs light and in doing so it produces radicals that initiate the polymerisation and the UV-absorber, which absorbs light but causing no reaction. Increasing the concentration of both components should lower the D_p since they are both light-absorbing species[169], [170]. At the same time, addition of PI increases the rate of initiation[170] and therefore, the polymerisation rate; this can lead to larger cured thickness for the same values of energy dose (i.e. same values of exposure time), which means a larger slope of the working curve and therefore larger calculated D_p. These considerations suggest that D_p is not a good representation of the resin light absorption and should only be considered as the slope of the obtained working curve. Additionally, in the absence of UV-absorber, the cured thickness obtained for a certain curing time is a function of the PI concentration that goes through a maximum value[170], this can complicate the use of the working curve. Though this complication is generally avoided as STL resins contain UV-absorbers that are the main factor determining the light absorption. This can be desirable in order to make the printing faster, though we should notice that most of the printing time is actually determined by a series of mechanical movements that are basically independent from the photo-curing characteristics. Conversely to the addition of PI, the addition of UV-absorber, even in small quantities, can drastically reduce the value of D_p (increasing the concentration of absorber from 0 to 0.1 wt% can halve D_p). The result of a smaller value of D_p is that smaller features can be printed, though this is relative to the native resolution of the printer in use and to its minimum layer thickness. A smaller penetration depth results in less light over-curing past the layer thickness and into the preceding layer, therefore improving Z resolution. Additionally, any light scattering along the borders between illuminated and non-illuminated areas, is absorbed by the absorber, which greatly increases the level of detail on the XY plane. It should be noted that some extent of over-curing on the Z axis is desirable. Given a certain layer thickness, the curing time should be larger than the one required to reach the gel point at that thickness. This is because, slightly curing the precedent layer into the successive one guarantees good attachment and confers mechanical strength to the part, so that the printing process can be withstood. Very often, when working on the formulation of a

custom resin, these kind of considerations cannot be easily put into action because many STL printers do not allow for the curing time to be freely changed. Therefore, one has to adapt the resin to the available settings, by changing the UV-absorber and PI concentration. Primarily, this means that the resin should be tailored so that the energy dose inherent to the settings is enough to cure a layer thickness that is higher than the one predetermined by the settings. This can be achieved by first changing the PI concentration. Then, by changing the concentration of absorber, one can reduce D_p so that better detail resolution can be obtained by the already discussed mechanism.

Photo-initiators and absorbers are therefore the most impactful components for the resin photo-curing behaviour. The concentration and nature of polymers and monomers in use also have some influence in terms of resulting working curve, though they carry much more weight on the mechanical properties of the green part and final part. Additionally the concentration and molecular weight of the reactive polymers will have great influence on the viscosity of the resin. Several mechanical movements in a STL printer are dependent on the viscosity of the resin. For example, after each layer is printed the build platform moves in order to detach the printed layer from the printing window, which is commonly known as peeling step. Independently from the peeling mechanism (pulling, tilting, sliding etc.), the viscosity of the resin has great impact on the force involved in this step and a resin with high viscosity can cause the printer to jam or the part to break. A safe guess for upper boundary of viscosity (at 25 °C) that should work with several STL printers is 1 Pa·s, as many commercially available resins have viscosity in the 0.1-2 Pa·s range (e.g. Formlabs, EnvisionTEC, Kudo3D or Henkel resins). Changing the ratio of polymers to diluent is the most straightforward way to tune the viscosity. Higher amount of (low viscosity) diluent should decrease the viscosity; additionally the use of liquid monomers can have the same effect. Another possibility consists in operating the printer under heating, though this requires consideration over the volatility of the resin which can cause the properties to change during printing (which typically lasts for hours) and irritant or toxic fumes to be produced.

2.3.1 Applications of stereolithography to tissue engineering scaffolds

Considerable research in stereolithography is aimed at medical related applications, as a matter of fact the most highly cited papers on the topic are related to tissue engineering and medical applications[25], [163], [171]–[175]. Much of the research focus has gone into formulating resins that can be printed into biocompatible parts and that perform on similar level as the commercial standard. The complexity and accuracy of geometries

that can be printed by desktop printers, is particularly appealing to the fabrication of porous scaffolds in tissue engineering[7], [153], [154], [156], [164], [172], [176]–[182], where excellent control over pore size, geometry and interconnectivity is of great importance. Scaffolds employed in tissue engineering need to provide mechanical support and a suitable environment for seeded cells and any forming tissue, during either *in vivo* or *in vitro* applications. The porosity, pore size, surface orientation and the pores interconnectivity, are all factors that determine how cells distribute and if they can survive and proliferate in the scaffold microenvironment[153], [171], [177], [179], [181], [183], [184]. STL allows to optimise these parameters so that, for example, very narrow pore size distribution is obtained or that all pores are connected to each other. Additionally, *in vitro* cellular cultures are often employed to understand and model the cellular behaviour in response to their biochemical and mechanical environment; the control that STL provides over the construct geometry can be exploited to facilitate and render these studies and models more robust, as single variables can be reliably changed.

Besides having specific geometrical features, the scaffold should not induce a toxic or inflammatory reaction when *in vivo* and in general should not be cytotoxic. This can be summarised as being biocompatible, though we should acknowledge that the concept of biocompatibility is specific to the type of application and desired outcome[185]. The function of the scaffold is also a temporary one; once the tissue formation is such that the scaffold is not required, this should disappear completely from the body. Furthermore, the degradation products should also be non-toxic and should not accumulate in the body. Therefore, the STL resins used for the fabrication of tissue engineering scaffolds are composed of low molecular weight reactive polymers (macromers) that are known to be biocompatible and to degrade in the body into harmless products. Usually, the macromers need to be diluted by the use of appropriate diluents. In this respect we can differentiate between two approaches. One is to use a reactive diluents[152], [163], these are effectively liquid comonomers that will make part of the final crosslinked network in measure more or less equal to their weight percentage in the resin. The other is the use of non-reactive diluents, these are solvents that will not take part into the polymerisation reaction. The two approaches have both benefits and drawbacks to them. Changing the concentration or type of reactive diluent is quite effective to tailor the properties of the final polymer, for example reducing or increasing the glass transition temperature of the printed network. When using a reactive diluent the mechanical properties of the green part are reasonably close to the ones of the part after any post-processing. Conversely, a non-reactive diluent is effectively swelling the green part at all times, this can weaken the

part and cause tearing during printing. In our experience, when printing with a resin containing non-reactive diluents, the first ten layers should be considerably overcured to create a strong foundation for the remaining layer. During postcuring the non-reactive diluent needs to be extracted from the part in order to obtain the desired mechanical properties. This results in considerable shrinkage, though this is isotropical and can be taken into account by scaling-up the part design. The benefit of not using a reactive diluent is mainly related to biomedical applications. Reactive diluents are typically monomers that form non-degradable chains that will be left behind as macromolecules after degradation of the rest of the network. This is undesirable for *in vivo* applications, particularly because, to date, there is not much evidence and studies focusing on their physiological fate. The use of non-reactive diluents prevents the problem so that the only non-degradable macromolecules formed are the kinetic chains formed during polymerisation of the macromers, for which there are studies concluding that their molecular weight is below the renal clearance cut-off[186]–[188].

As just discussed the post-processing of the green part includes an extraction process. In general, non-biomedical applications of STL do not require any type of extraction and only washing of excess resin and (thermal) UV post-curing are performed. The extraction step is required in biomedical applications because all unreacted species are cytotoxic, toxic and irritant to different extent. This is typically very true for many photo-initiators, which can be severely toxic. The non-reactive diluents are usually chosen to be non-toxic and non-volatile, so that no harmful vapours are produced during printing and to make resins more appealing to the biomedical applications. Independently from biocompatibility considerations, their complete extraction is required to obtain the intended mechanical properties.

Chapter 3 – Materials and methods

In this Chapter we report the main materials and methodologies employed throughout our research.

3.1 Macromers synthesis and characterisation

3.1.1 Materials

D,L-lactide (DLLA), PURASORB® DL, was obtained from Corbion (The Netherlands); ε-caprolactone (CL), 1,6-hexanediol (HDO), tin(II) 2-ethylhexanoate ($SnOct_2$), triethyl amine (TEA), methacrylic anhydride (MAAh), were acquired from Sigma Aldrich (USA); potassium carbonate (K_2CO_3), tetrahydrofuran (THF) and 2-propanol (IPA) were obtained from Fisher Scientific (USA).

All chemicals were used as received. DLLA was stored under vacuum at -20 °C and allowed to reach ambient temperature before being used.

3.1.2 Synthesis of poly(D,L-lactide) hydroxyl terminated oligomers

Poly(D,L-lactide) (PDLLA) hydroxyl-terminated oligomers were synthesised through the ring opening polymerisation (ROP) of DLLA on a 100 g basis. HDO was used as initiator for the polymerisation reaction and $SnOct_2$ was employed as catalyst. Room temperature DLLA and HDO were added to a 1 litre round bottom flask (RBF) with a PTFE stirring bar. The moles of HDO were calculated on the basis of the desired molecular weight (M_n) of the polymer, dividing the total mass of monomer by the target M_n. This means that to obtain M_n equal to 5000 g/mol, 0.02 mol were added to 100 g of DLLA; for M_n of 3000 g/mol, 0.0333 mol of HDO were added to 100 g of DLLA. The RBF was connected to a Schlenk line and a nitrogen atmosphere was created by flushing three times. The reaction chamber was heated to 130 °C and after 30 to 60 minutes 5 droplets of $SnOct_2$ were added from the side neck of the RBF. The nitrogen atmosphere was re-created and the reaction was left to proceed at 130 °C and under N_2 flow for 72 hours. The RBF was insulated with glass wool to prevent the deposition of DLLA on the wall, which would affect the M_n. The conversion of DLLA and M_n were confirmed by proton-nuclear magnetic resonance spectroscopy (^1H NMR, $CDCL_3$, Bruker AVIII 300MHz), as discussed in the results section (Chapter 4).

3.1.3 Synthesis of poly(D,L-lactide)-ran-poly(ε-caprolactone) hydroxyl terminated oligomers

Poly(D,L-lactide)-ran-poly(ε-caprolactone) (PLA-ran-PCL), hydroxyl terminated, random copolymers of PDLLA and poly(ε-caprolactone) (PCL), were synthesised through the ring opening polymerisation of DLLA and CL, on a basis of 100 g of DLLA. The ratio of DLLA to CL was chosen in response to the desired glass transition temperature. The synthesis followed the same procedure as previously explained for the ROP of PDLLA. Briefly, DLLA, CL and HDO were added to the reaction flask and left to heat up at 130 °C for 30 minutes. Then, $SnOct_2$ was added (5-6 droplets) and the mixture was left to react at temperature, under N_2 atmosphere and stirring, for 72 hours. The conversion was monitored through ^{1}H NMR.

3.1.4 Synthesis of methacrylated macromers

After confirming sufficient monomers conversion through ^{1}H-NMR, the oligomers were reacted with MAAh to synthesise reactive macromers with methacrylate end groups. An excess of 50-100 mol% of MAAh per hydroxyl group was used, the moles of –OH were taken as twice the moles of HDO used during ROP. TEA or K_2CO_3 were used as proton scavenger in the same molar amount as the added MAAh. At the end of the ROP reaction, the heater was turned off and the mixture was allowed to cool down. After few minutes, dry THF was added from the top of a condenser attached to the RBF. Around 50 ml of THF were slowly added to the reaction chamber, followed by vigorous shaking, in order to effectively dissolve the polymer, so that around 120 rpm stirring velocity could be maintained. Once the solution was at room temperature, MAAh and the scavenger were slowly added and the RBF was vigorously shaken once again. The reaction was left to proceed for typically 5 days, with the heating plate set at 20 °C. The functionalisation degree (DF) was followed through ^{1}HNMR as discussed in Chapter 4.

3.1.5 Precipitation and purification of macromers

The macromers mixture was precipitated in cold (-80°C) isopropanol, under stirring. The supernatant was discarded and the precipitated mass was left to dry overnight. The mass was then frozen by liquid N_2 and crushed into small particles. The powder-like compound was split in two and slowly poured in 4L cold (3-5°C) water under stirring. This water-washing was performed at 3-5 °C for 24 hours. The stirring was then stopped and the powder was left to precipitate while at cold temperature. Most of the water was discarded, the remaining water/powder mixture was filtered through vacuum filtration in different stages. The resulting cake was scraped and moved to vacuum bags. The macromer was

eventually freeze dried, producing the final product. The obtained macromers were named ALDP#, where # was an identification number (e.g. ALDP007).

3.2 Resins formulation and network preparation

3.2.1 Materials

Diphenyl(2,4,6-trimethylbenzoyl)phosphine oxide (TPO), 2,5-Bis(5-tert-butyl-benzoxazol-2-yl)thiophene (BBOT), hydroquinone (HQ), isobornyl methacrylate (IBMA), methyl methacrylate (MMA), diethylene glycol diethyl ether (DEGDEE) were all obtained from Sigma Aldrich (USA). Benzyl alcohol (BnOH) was obtained from Alfa Aesar (USA). All other diluents that are mentioned in the results section were obtained from Sigma Aldrich. All chemicals were used as received and stored accordingly to MSDS available from vendors.

3.2.2 Formulation of resins containing non-reactive diluent only

The required amount of macromer was weighted and added to a 50 mL round bottom flask. The required amount of photoinitiator, TPO, UV-absorber, BBOT and inhibitor, HQ, were added to the required amount of non-reactive diluent, either BnOH or DEGDEE and stirred until completely dissolved. The macromer was slightly warmed up while stirring using a dry block fitting the flask and a hot plate. The diluent mixture was slightly warmed up by heat gun and added to the macromer. The mixture was kept stirring until the macromer was completely dissolved. For resins were small traces of solid matter could be discerned after long stirring, a filtration step was performed through a nylon paint mesh. The glassware in use was typically covered in aluminium foil to avoid exposure to ambient light. The resins were identified by the diluent nomenclature followed by an identification number, for example BnOH025 identifies the 25^{th} composition based on the non-reactive diluent benzyl alcohol. Compositions were deemed different if any concentration was changed or if any component was changed, including different batches of macromer.

3.2.3 Formulation of resins containing reactive diluent

The required amount of macromer, non-reactive diluent, TPO, BBOT and HQ were mixed as previously described. The mixture was left to cool down, then the reactive diluent was added and the resin was stirred until clear from solid parts. The amount of reactive-diluent to be added was calculated on the basis of the desired glass transition temperature to be obtained and in measure to obtain a certain ratio between macromer and total mass of diluent, as discussed in the results section.

3.2.4 Preparation of photo-crosslinked networks

Glass microscope slides of 73x52 mm were covered in a uniform thickness of 500 μm of resin by casting knife (Elcometer 3580). The slide was placed on the window of an Ember DLP printer (Autodesk, 405nm, 22.5 mW/cm^2) to be cured by the pattern shown in Figure 3-1. Each cured network had size of 50x4 mm, the light exposure was set at 60 seconds. After curing, excess resin was absorbed on paper, then the films received a quick rinse in isopropanol. The excess solvent was absorbed on paper and the films were left to dry for few minutes. The films were then placed straight on a Teflon sheet (Kudo3D Inc., Titan Replacement Teflon Films), a second sheet was placed on top and two glass slides were placed below and above. The sandwiched films were post-cured for 20 minutes in a UV-box (VWR International, UV crosslinker CL-1000L 356nm), then the other side was post-cured for 20 more minutes. The post-cured networks were weighted and moved to a Soxhlet apparatus were they were extracted by isopropanol for at least 72 hours. The extracted networks were left in their thimbles and left to dry while in the leftover isopropanol. When dry they were placed on PTFE sheets (RS Components Ltd., opaque fluoroplastics sheet 3mm thick) and moved to an oven at 80 °C (SciQuip, SQ-4845) for at least 72 hours or until dry (i.e., negligible mass change over 24 hours). Thicker networks were obtained by UV-box curing (same model as above) of resin injected in PTFE moulds, where the resin was free from UV-absorber to enable curing of the entire thickness. The main mould geometry in use was 40x13x3 mm (LxWxT). The curing was performed for 45 minutes. The networks were extracted in a Soxhlet apparatus, by boiling isopropanol, for approximately 96 hours. The extracted network were moved to an oven and dried until no change in mass was observed over 24 hours. The networks were identified by the name of the resin followed by an identification number, e.g. BnOH025-007. When the specimens were cut in two halves, one would also be identified by the letter "b" (e.g. BnOH025-007 and BnOH025-007b).

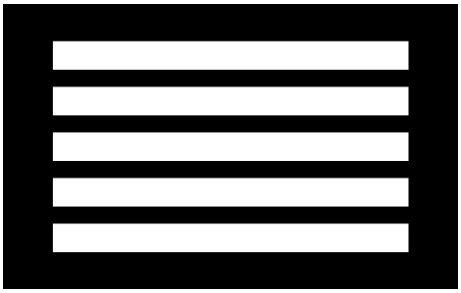

Figure 3-1 3D printing pattern. Five rectangular shapes of 50x4 mm, out of a 64x40 mm area at 1280x800 pixel resolution, are printed.

3.3 Thermo-mechanical analysis and shape recovery characterisation

All thermo-mechanical characterisations were performed on a DMA Q800, dynamic thermal mechanical analyser (TA Instruments) equipped with the ACS-3 air chiller for sub-ambient temperature control. The shape memory cycle and shape recovery characterisation were performed on the same DMA Q800 and also in a laboratory oven (SciQuip, SQ-4845). Differential scanning calorimetry was performed on a DSC 2010 (TA Instruments).

3.3.1 Temperature sweep test

Temperature sweep tests were performed on the Q800 with tension clamp (film), in the multi-frequency – strain module. The specimens in use were the prepared film networks, the clamped length was approximately 7.5 mm with the other dimensions being dependent on the specimen; average width was 3.45 mm and average thickness was 0.25 mm. A small force of 0.01 N was given as preload to keep the film straight. The oscillation was performed at 1 Hz and at 15 μm amplitude, force track was kept at 125%. The method was custom made. A 15 minutes equilibration at 80 °C was followed by a 2 °/min temperature ramp to 0 °C. The temperature was ramped from 0 °C to 80 °C three times. The data was acquired at 1 point per second, analysed and exported by the TA Universal Analysis suite of software. Only the data from the last cooling and heating ramps was used in the discussion of the results. Figure 3-2 reports a schematic for the test set-up with tension clamps on the DMA Q800.

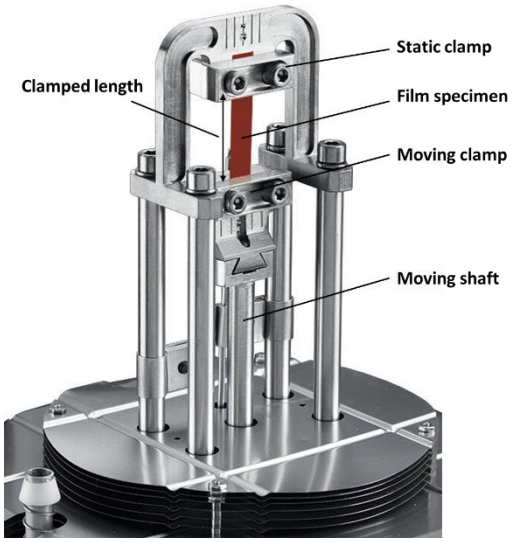

Figure 3-2 Schematic of tension clamp set-up on the DMA Q800. The shaft can impart static or dynamic forces or deformations. Image reproduced from tainstruments.com.

3.3.2 Stress relaxation tests

Stress relaxation tests were performed on the DMA Q800 with dual/single cantilever clamps (35 mm) in the stress relaxation module. The specimens were slabs of approximately 32x10x2.4 mm (LxWxT) though the single cantilever length is the experimentally relevant one, for this model of clamps it is about 17.5 mm. The specimens were equilibrated at 80 °C in the DMA for 10-15 minutes previous to the test (the segments for thermal equilibration are motor off followed by the equilibration step). The method was a time-temperature superposition stress relaxation, which consists of a series of stress relaxation tests performed in succession over the same specimen and at incremental temperatures. Each stress relaxation cycle is formed by an isothermal segment of 5 minutes, then followed by the displacement and relaxation for 10 minutes. One method was performed at temperatures from -20 °C to 40 °C at 5 °C increments, with 0.1% displacement. A second method was performed at temperatures from 35 to 100 °C at 5 °C increments, with 0.5% displacement. The data acquisition was same as previously stated. The output of the test is typically referred to as relaxation modulus, this is equal to the instantaneous value of the stress to strain ratio.

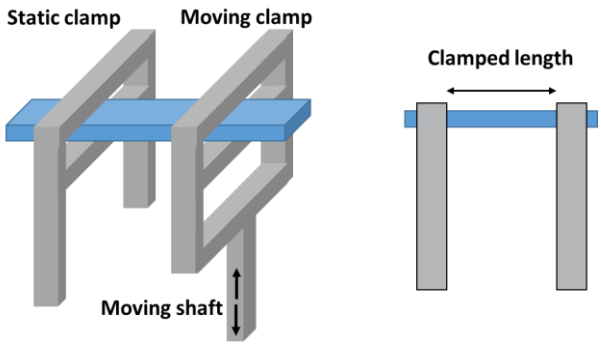

Figure 3-3 Schematic of single cantilever set-up on the DMA Q800.

3.3.3 Shape memory cycle on DMA Q800

The shape memory cycle was performed for film specimens (same geometry as previously described), with tension clamps and multi strain module. The module in use was strain rate; this module allows for strain and force control segments to coexist in a method. The method was custom made. We report one example with recovery at 45 °C:

```
Method Log:
1: Data storage: On
2: Force 0.010 N
3: Ramp 3.00°C/min to 80.00°C
4: Equilibrate at 80.00°C
5: Isothermal for 60.00 min
6: Measure length
7: Mark end of cycle 0
8: Strain 10.0 %
9: Isothermal for 60.00 min
```

```
10: Mark end of cycle 1
11: Equilibrate at 0.00°C
12: Isothermal for 60.00 min
13: Mark end of cycle 2
14: Force 0.000 N
15: Isothermal for 1.00 min
16: Ramp 5.00°C/min to 45.00°C
17: Isothermal for 74.42 min
18: End of method
```

The method makes use of the strain segment to impart an isostrain condition, then of the force segment to unload the specimen. The last isothermal segment did not have fixed time length and the log reports the elapsed time from the moment the temperature is stable at the recovery value (here 45 °C), until the last recorded data point. As a note, the reported value is one tenth of the actual value (the reason for this, eludes the author).

3.3.4 Differential scanning calorimetry

The DSC was performed with aluminium pans and lids (TA Instruments, DP-TA-STD). Samples with mass between 10 and 15 mg were obtained from cured networks, the exact weight was measured for each run. A first heating ramp was performed at 5 °C/min, from room temperature to 80 °C, a second one was repeated after cooling down the cell back to room temperature. The cooling accessory was not available for this machine; the cooling was obtained by indirect contact with cold water. Before the second heating, the cell was equilibrated at 25 °C. The data sampling was left standard at 0.2 sec/pt. The data from the second heating ramp was used for discussion purpose. The data was imported to OriginPro (OriginLab Co.); the heat flow was differentiated to the 2nd derivative, with respect to the temperature, by the Origin tool suite (Analysis: Mathematics: Differentiate).

3.3.5 Oven/freezer/oven shape memory cycles

Shape memory cycles were performed "manually" with the use of a laboratory oven and laboratory freezer (-20 °C). Film specimens were first labelled and marked for dimensional reference as in Figure 3-4 and images (about 2200x500 pixels) were taken at relevant time points to be processed on ImageJ (https://imagej.nih.gov/ij/). The lengths were also measured by calliper (Mitutoyo 150mm Digital Caliper). The films were equilibrated in oven for one hour at 80 °C, then left to stretch under a 0.08 N force by clamping both ends with binder clips. After one hour the specimen was quenched in icy water while still clamped, blotted dry and moved to the -20 °C freezer for at least one hour. For the recovery, the oven was set at the recovery temperature for one overnight, one paper clip was removed and the specimen was left to recover. The measurements

and images were taken: after equilibration at 80 °C, after one hour deformation (once quenched), before the start of the recovery process and at different time points during the recovery process.

The same procedure was repeated for specimens that were stored at 37 °C (in an incubator) and 20 °C (in a temperature-controlled microscopy room).

At the end of the experiments all specimens were heated up (80-100 °C) for around 30 minutes and then left to cool down. Any residual strain recovery was measured by calliper.

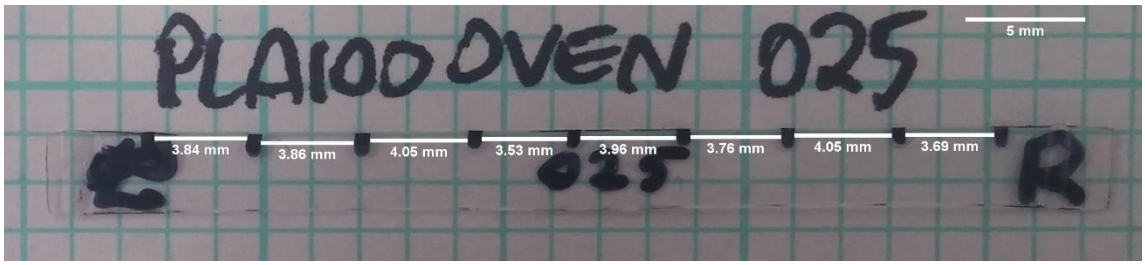

Figure 3-4 Film specimens were labelled and marked to take dimensions on ImageJ additionally to calliper measurements. The images were taken before the start of the shape memory cycle, after equilibration at 80 °C, after imparting the deformation for one hour, before the start of the recovery process and at different time points during the recovery process.

3.4 Tests on the Ember DLP printer

Here we describe relevant testing procedures performed on the Ember DLP printer by Autodesk. The printer is now out of production, which is unfortunate as it was one of the few really open source stereolithography printers in the market. It runs the DLP4500 .45 WXGA DMD by Texas Instruments, that should result in 50x50 μm resolution on the XY plane. The LED in use produces blue light centred on 405 nm, at 22.5 mW/cm^2 power. The CAD files are fed to the printer after processing on Print Studio, a software by Autodesk that is also not supported anymore. The processed file is a .zip containing the print settings and a series of 1280x800 pixels .png black and white images for each layer to be printed (the white is where the light will shine). The printing window is 64x40 mm, the bulk material is glass and the surface that comes in contact with the resin is PDMS; the tray containing the resin is in polypropylene (originally polycarbonate). The build head surface is anodized aluminium. The minimum step increment for the movements along the Z is 10μm. A typical printing job starts with the calibration step, meaning that the build head is lowered into the resin, almost in contact with the window. Once this is performed the printing continues automatically in the typical layer by layer fashion. The peeling mechanism works by rotating the tray clockwise, so that the build head relative position is away from the window. This allows the head to be pulled up with no considerable suction force. Theoretically, the PDMS acts as an oxygen buffer to prevent

polymerisation on top of the window by oxygen inhibition, hence avoiding jamming during peeling.

3.4.1 Printability tests

To improve build head to resin attachment a single layer of commercial resin was printed on the head, with slightly less curing time than what suggested by the standard settings. To reduce attachment between printed part and window, this was coated in Teflon sheets (Kudo3D) cut to fit the correct size. The first layer printing test was done with only the amount of resin required to cover the window area, the test part was a 15x5 mm rectangle. The CAD for the printing jobs were produced on AutoCAD (Autodesk) and exported as .stl files (STL out command). The parts with gyroid geometry were produced on k3dsurf (http://k3dsurf.sourceforge.net/), a surface generator based on mathematical syntax. The code for the structure is as follow:

if(abs(x)<6*pi & abs(y)<6*pi & abs(z)<12*pi, cos(x) * sin(y) + cos(y) * sin(z) + cos(z) * sin(x)-0.6, 0)

This example results in a geometry made of 6x6x12 repeating units.

3.4.2 Working curve tests

The build head was removed from the printer. A thin microscope coverslip (thickness around 100 μm) was measured for its thickness, then placed at the centre of the printing window and covered with a thick layer of resin (~1mm). A print job was created that would expose a 5mm diameter full circle. Each layer in the job file was the same circle and had a different exposure time (e.g. 5, 10, 15 seconds). Every printed circle was measured for its thickness (Mitutoyo Dial Thickness Gauge 7301) and the process was repeated. The thickness values plotted against the irradiated maximal dose (time x power) where fitted by logarithm fitting on Excel to obtain the working curve equation.

3.5 Tests on Perfactory 4 Mini

The Perfactory is a professional DLP printer by EnvisionTEC. The DLP system allows for 1280x1024 pixels to be projected, with size of 32x32 μm. The printer is not open source in any aspect. Information on the settings were directly retrieved from the vendor, additional information on the exposure time were extrapolated by direct observation. The chosen setting was: PIC100 50 μm no basefilm. The power of the apparatus was set to 1800 mW/dm^2. We here discuss only the difference in working curve test; once the resin composition and settings were decided we simply proceeded to print different parts.

3.5.1 Working curve test

The lamp power can be calibrated by the user, this works by a spot being illuminated on the printing tray until the user confirms that the next calibration spot should be turned on. We exploited this feature to get cured thickness values against exposure time. The step are the same as for the Ember, though in this case the exposure time could not be controlled and we used a stopwatch to measure the elapsed time.

3.6 Plots and data manipulation

Any data manipulation (e.g. normalising) is expressively stated and performed on Microsoft Excel or OriginPro. Most data is reported as obtained from the raw file. The box plots used in the thesis are produced on OriginPro; the figure below describes their meaning, where SD is the standard deviation (Origin makes use of the sample SD).

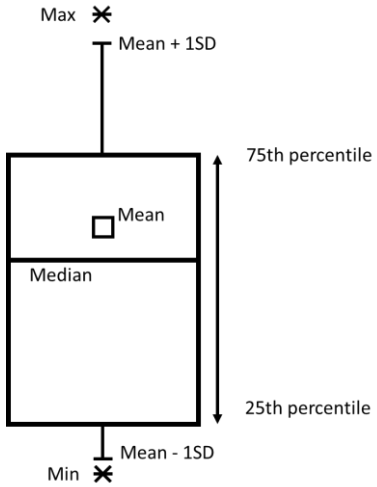

Chapter 4 – Synthesis of macromers, preparation of resins and specimens for the characterisation of the polymeric material

4.1 Introduction

In this Chapter we discuss the synthesis and characterisation of the main macromers in use, the preparation of photo-polymerisable resins and the preparation of the specimens used for the thermo-mechanical analysis.

We developed resins that could be specifically used for stereolithography, under the requirement of the printed material being bioresorbable of the resin system being not toxic. Aiming at the fabrication of shape memory polymers (SMPs) with different recovery behaviour, we worked on copolymerising or blending different monomers to obtain a range of networks with different glass transition temperatures. We pursued this objective as the application temperature is a pre-determined factor, around which the polymer chemistry and thermal history (i.e. the shape programming) of the SMP need to be tailored. In preparation for the material characterisation we tested different approaches to obtain specimens, which included the curing and post-curing process and extraction of soluble part from the cured network. We can summarise these objectives as:

1. Preparation of photo-curable resins suitable for stereolithography and bioengineering applications. This requires:
    a. Biodegradable and bioresorbable polymer/s with appropriate molecular weight and functionalities
    b. Low-toxicity non-reactive diluent, photo-initiators and UV-absorbers with light absorbance suitable to control the photo-polymerisation process
2. Tailor networks with different glass transition temperatures by copolymerisation, with the purpose of unlocking a large range of shape recovery response at body temperature

The product of a stereolithography printing process is a chemically crosslinked amorphous network. It is safe to assume that the printed parts would display shape memory properties, as also found in the steadily increasing number of research works on 4D printing[5]–[7]. We focused on the use of low molecular weight poly(D,L-lactide) (PDLLA) and poly (ε-caprolactone) (PCL) as both hold the potential for bioresorbability and have been widely studied and applied as biocompatible materials for example in the fabrication of tissue engineering scaffolds and also in clinical applications. The mechanical properties of PDLLA are particularly desirable for the tissue engineering of hard tissue as the material is rigid at body temperature with elasticity modulus of 1-3 GPa.

We synthesised macromers with low molecular weight of 3000 and 5000 g/mol and linear structure. Both choices help with keeping the resin viscosity low, which in turn facilitates the stereolithography process. This printing process is, in its essence, a series of geometrically controlled photopolymerisation steps. The key items are a photo-initiator and oligomers and/or monomers that are able to undergo the polymerisation process. Therefore the macromers are functionalised with a methacrylate group at both ends, which enables photo-initiated free radical polymerisation. The use of dimethacrylate (also acrylate) systems results in chain-growth radical polymerisation that is known to lead to relatively broad glass transition region of the final network, due to heterogeneity of the polymerised networks (e.g., unevenly distributed crosslink density) [74], [189], [190]. In this case the broad glass transition region is a desirable property in order to achieve long recovery time. A broad temperature interval of the glass transition is, in fact, associated with the mechanism of multiple shape memory effect for amorphous SMPs [12], [104], [109]. Achieving multiple shape memory effect is not an objective of our research, what is relevant is the idea that given a broad glass transition the material can recover from the deformed state at temperatures that are quite lower than T_g (as defined from tanδ peak), exactly because the glass transition region is large, and this should provide us with slow recovery kinetics. At the same time, we planned to obtain networks with different glass transition temperatures because we assumed that the shape recovery cannot be influenced to a large enough extent by changing the shape programming conditions during a shape memory cycle. This is an assumption we derive from the available literature on shape memory polymers and we will later show it to be correct (in Chapter 8). To control T_g we copolymerised D,L-lactide and ε-caprolactone, this gives access to T_g's lower than the one of PDLLA. To obtain larger T_g's we made use of reactive diluents mixed in the stereolithography resins. We chose methacrylate monomers that form high T_g polymers, namely methyl methacrylate (MMA) and isobornyl methacrylate (IBMA). Generally we worked with non-reactive diluents as doing so would limit the amount of non-hydrolysable mass in the networks. Additionally the use of non-reactive diluents increases the mobility of the components involved in the photo-polymerisation process, so that we can expect to achieve higher conversion and gel content than what usually found for stereolithography resins [151][169].

4.2 Synthesised macromers

The macromers were synthesised by ring opening polymerisation or copolymerisation (ROP) in the presence of 1,6-hexanediol (HDO) as initiator and stannous octoate as

catalyst. The products of the ROP were then functionalised with methacrylate moieties at both ends by reaction with methacrylic anhydride (MAAh). The standard procedures are reported in the Materials and Methods section of the thesis. Proton nuclear magnetic resonance (^{1}H-NMR) spectroscopy was used to determine monomers conversion (χ), number average molecular weight (M_n) and degree of functionalisation (DF), as well as to check for impurities in the final products.

4.2.1 Dimethacrylate terminated poly(D,L-lactide)

Figure 4-1 reports the nomenclature of the protons for the oligomer, PDLLA-2OH and macromer, PDLLA-2MA and the respective ^{1}H-NMR spectra. The spectra we used for the PDLLA-2MA are from purified specimens, as it can be noticed from the absence of peaks corresponding to the solvent in use during the functionalisation reaction. The monomer conversion was calculated from the peak integral corresponding to the lactide monomer –C**H**COO– proton (5.05 ppm) and the oligomer repeating unit –C**H**COO– proton (**d,** 5.2 ppm). The conversion was found to be 94%, at the lowest, at 72 hours of reacting time. We reacted samples of PDLLA-2OH with trifluoroacetic anhydride, this results in the disappearance of the peaks **b** and **d'** as showed in Figure 4-2 and is used to confirm the nature of the protons; it should be noticed that the **d'** peaks shift to the left of **d**. After sufficient reaction with MAAh, the degree of functionalisation was calculated from the integral corresponding to the leftover –O**H** moieties, labelled as **d*** in Figure 4-1 (ii)**.** The value of DF was found to be at least equal to 92%. The M_n was calculated from the integral of the **d** peaks and the hexanediol protons –C**H**$_2$O – (**c**, 4.13 ppm) and was found to be equal to the desired one within a 15% error. Here we report the calculation formulas:

$$\chi_{DLLA} = \frac{\int \boldsymbol{d}}{\int \boldsymbol{d} + \frac{1}{2}\int 5.05ppm} \tag{4.1}$$

$$M_n = \frac{\int \boldsymbol{d}}{\frac{1}{4}\int \boldsymbol{c}} \cdot 72 + 116 + 2 \cdot 68 \tag{4.2}$$

$$DF = 1 - \int \boldsymbol{d}^*/2 \tag{4.3}$$

Where 72 is the molecular weight of the repeating unit, 116 of the reacted initiator, 68 of the ends and the integral is just a symbolism for the value of the area calculated on ACD/NMR Processor (Advanced Chemistry Development, Inc., ACD/Labs). The ratios in the formulas account for the different number of protons, for example the **f** peaks corresponds to four protons per chain while the **d'** to two, hence the 1/2. In Table 4-1 we

report the calculated values of M_n, χ_{DLLA} and DF for eight batches of PDLLA-2MA that were prepared with target M_n of 3000 g/mol.

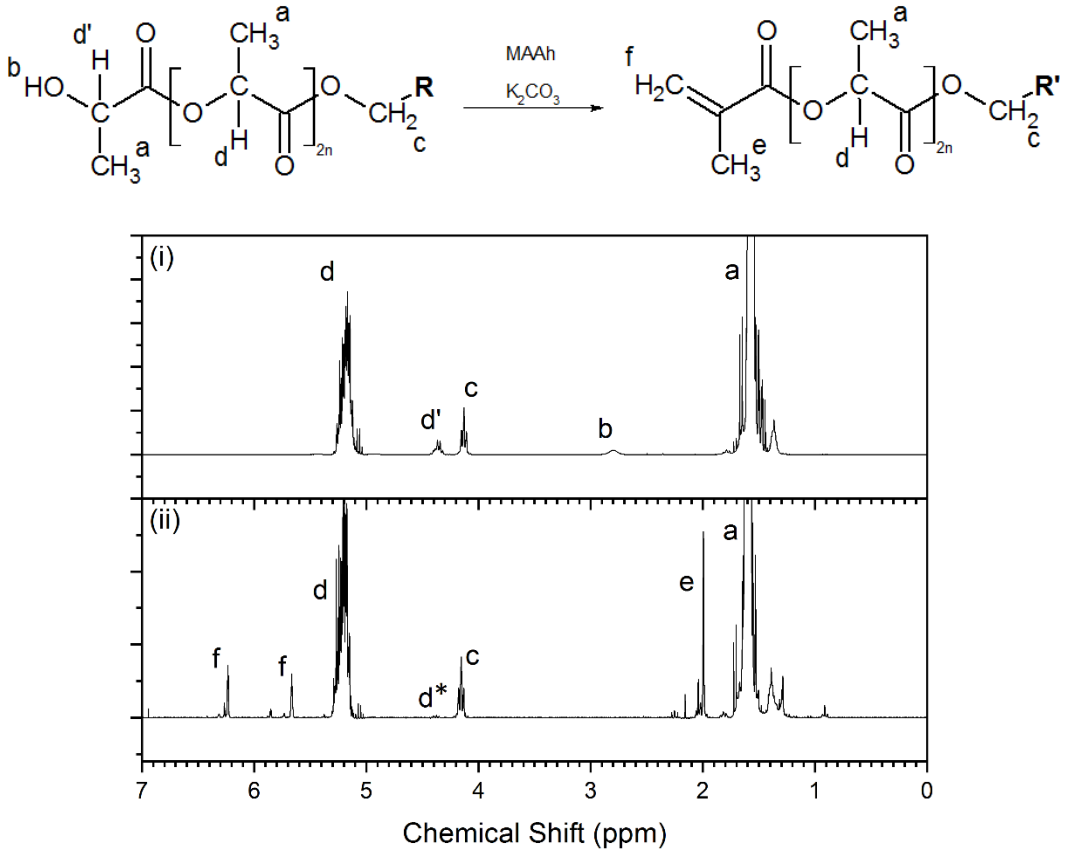

Figure 4-1 The PDLLA-2OH oligomer is reacted with methacrylic anhydride to yield the macromer PDLLA-2MA. The ^{1}H-NMR spectra of the oligomer (i) and macromer (ii) are studied to calculate χ_{DLLA}, M_n and DF.

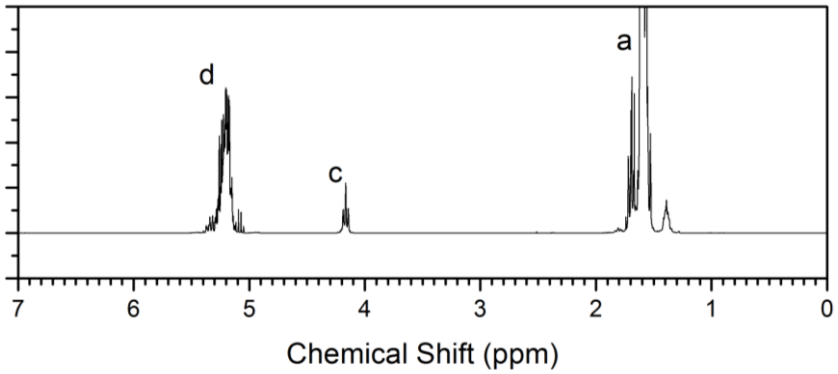

*Figure 4-2 An oligomer sample is reacted with trifluoroacetic anhydride. The disappearance of the peaks at **b** and **d'** confirms the nature of the protons. The peaks can be seen to shift to the region near **d**.*

Code	M_n (g/mol)	χ_{DLLA}	DF
aldp08	3020	NC*	94%
aldp09	2804	94%	97%
aldp11	2740	94%	92%
aldp12	3170	99%	93%
aldp13	2863	98%	95%
aldp14	2890	97%	95%
aldp17	2610	98%	92%
aldp18	2707	99%	NC*

*Table 4-1 Prepared polymer batches of PDLLA-2MA, their calculated M_n, conversion of monomer and DF. * Value was not calculated.*

4.2.2 Dimethacrylate terminated poly(D,L-lactide-ran-ε-caprolactone)

The weight concentration of D,L-lactide (DLLA) and ε-caprolactone (CL) monomers were calculated accordingly to the glass transition temperature (T_g) to be obtained. The T_g of the random copolymer (PLA-ran-PCL) is approximated to the weight average of the homopolymers T_g's, therefore:

$$DLLA\ wt\% = \frac{T_g - T_{g,PCL}}{T_{g,PDLLA} - T_{g,PCL}} \tag{4.4}$$

With $T_{g,PCL}$ and $T_{g,PDLLA}$ the T_g's of, respectively PCL (-60 °C) and PDLLA (55 °C). The wt% of CL is then the complementary percentage to DLLA wt%. The ^{1}H-NMR spectra were obtained for the copolymer before and after reaction with MAAh. The calculations for monomers conversion, M_n and DF are similar to what reported in the previous paragraph. The additional peaks, corresponding to the labelled protons in the PCL units, are showed in Figure 4-3. The peaks corresponding to protons **c** and **g** (4.15 and 4.07 ppm, respectively) superimpose on the ^{1}H-NMR spectra, therefore we did not make use of the area at **c** and preferred to use the area at **d'** for the M_n calculation. The peaks corresponding to the **h** protons, show on the spectra at 2.32 and 2.41 ppm. The conversion of CL monomer was calculated from the residual area at 2.68 ppm, corresponding to the alpha hydrogens on the caprolactone ring. The DF was calculated from the area at **d',** before and after reaction with MAAh and also from the areas for the peaks at **f**. The values of DF were very different when calculated by the two methods.

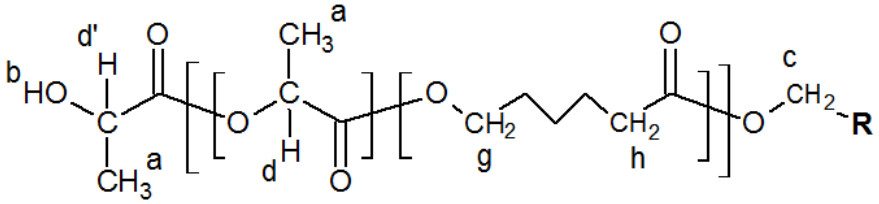

Figure 4-3 Representative structure for the hydroxyl-terminated copolymer. It should be noticed that the chains do not necessarily end with a PLA unit and that single units of PLA surrounded by PCL units will not be present as DLLA is a dimer.

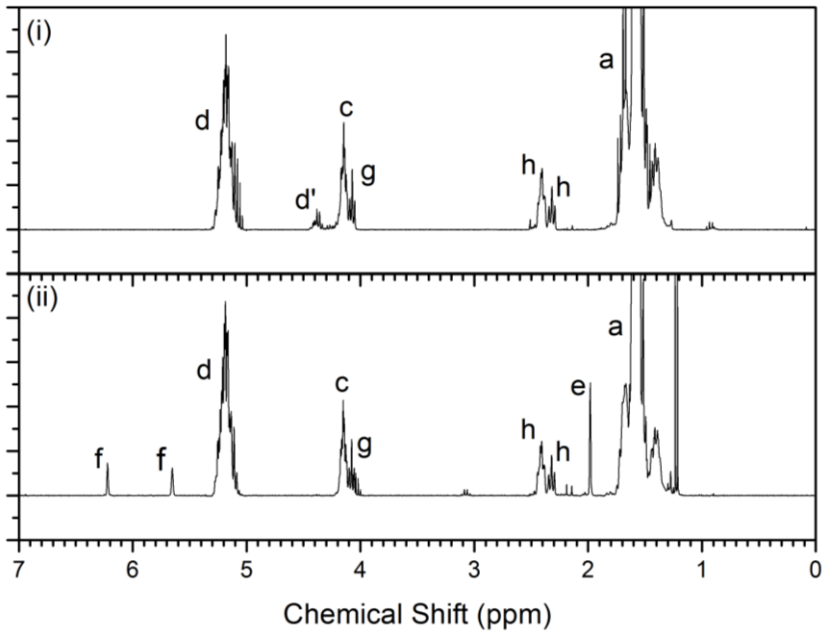

Figure 4-4 The ^{1}H-NMR spectra for the PLA-ran-PCL are studied before and after reaction with MAAh, to calculate monomers conversion, M_n and DF

Code	M_n (g/mol)	χ_{DLLA}	χ_{CL}	DF*	T_g (°C)**
aldp01	4997	99%	97%	100% (77%)	37.9 (37)
aldp02	4548	99%	87%	100% (90%)	47.1 (37)
aldp03	5068	99%	100%	100% (93%)	34.5 (37)
aldp04	5007	98%	96%	72% (72%)	33.5 (37)
aldp05	5217	99%	95%	87% (77%)	30.1 (30)

*Table 4-2 Values of M_n, monomers conversion, DF and theoretical T_g, calculated from the ^{1}H-NMR spectra. *The value between parentheses is the DF calculated from the integer of peaks at **f**, as opposed to the one calculated from the residual area at **d'**. **The value between parentheses is the target theoretical glass transition for the batch of polymer.*

4.3 Choice of the non-reactive diluent

In Table 4-3 we report the chemicals that were tested as possible non-reactive diluents for the preparation of stereolithography resins from the PDLLA or PLA-ran-PCL macromer. The table reports the quantitative and qualitative observations that were involved in the final choice of the solvents. We report tetrahydrofuran (THF) as a potent solvent that easily dissolves the macromers, photo-initiator (TPO) and UV-absorber (BBOT). This solvent is clearly too volatile and toxic to be used and just provides a baseline for qualitative comparison. Table 4-3 reports five of the solvents we tested and their qualitative assessment. None in particular was found to well solubilise the random copolymers. Diethylene glycol diethyl ether (DEGDEE) and benzyl alcohol (BnOH) gave good results when dissolving the poly-lactide macromer. The highest concentration of macromer in diluent was of 60:40 (wt:wt), above this concentration the macromers cannot be fully dissolved. BnOH and DEGDEE were chosen as diluents for most resin compositions. We tend to prefer BnOH as the low volatility is very desirable, considering

the long printing time typical of stereolithography. All diluents could dissolve suitable amounts of TPO and BBOT, respectively, 3 wt% and 0.3 wt% in a 60:40 resin. In particular, the saturation of BBOT in BnOH was found to be equal to 1.75 wt%, or 0.69 wt% when in a resin containing 2 wt% of TPO. To resins containing 2 wt% of TPO, 0.2 wt% of BBOT, 58.7 wt% of PDLLA-2MA and 39.1 wt% of BnOH, we mixed small quantities of hydroquinone as inhibitor (< 0.1wt%). These resins could be safely stored at room temperature, in the dark, for several days, showing no signs of premature polymerisation. The same was found for one resin stored at 5 °C for two months.

Chemical	**v_p**	**μ**	**Hazard**	**H_2O**	**TPO**	**BBOT**	**PLA**	**PLArPCL**
THF	143	0.45	carcino.	++	n.a.	n.a.	++++	++++
Ethyl Lactate	2	2.4	unsafe+	++	+	+	+/-	-
Butyl Lactate	0.4	3.6	unsafe+	-	+	+	+	+
Ethyl Benzoate	0.18	1.7	safe	+	+	+	+/-	+/-
DEGDEE	0.37	3.6	safe	+	+	+	++	+
BnOH	0.1	5.3	unsafe	+	+	+	++	+

Table 4-3 Solvents tested for resin preparation and their properties (physical properties around room temperature). v_p is the vapour pressure in mmHg; μ is the viscosity in 10^{-3}Pa s. Hazard in order of gravity: carcinogenic>unsafe+>unsafe. H_2O column refers to solubility with water: (++) miscible, (-) very low or no solubility. TPO and BBOT: (+) the component is easily dissolved in amounts larger than what would be needed for a resin. PLA and PLArPCL: (+/-) macromer is not easily dissolved and resin is very viscous, (+) more easily dissolved but still too viscous, (++) more easily dissolved and relatively low viscosity.

4.4 Resins containing reactive diluents

The copolymerisation of DLLA and CL provides glass transition temperatures below the PDLLA one. We wished to also obtain networks with higher glass transition temperature, for this purpose we mixed reactive diluents in the resin formulations. We employed methyl methacrylate (MMA) and isobornyl methacrylate (IBMA), both PMMA and PIBMA have T_g around 110 °C or larger. MMA is the monomer most similar to the reactive end of the macromer but both its liquid and gaseous form are very flammable and toxic. IBMA is safe to use, has very low vapour pressure (0.01 mmHg @ 25 °C) and is derived from bio-based precursors, though it is very viscous (~0.01 Pa·s). The prepared resins (PDLLA/MMA, PDLLA/IBMA) contained a weight ratio of PDLLA-2MA to reactive diluent equal to 82:18, which places the theoretical T_g of the cured network at 65 °C. The macromer to diluent ratio was 60:40 wt:wt, with the diluent being a mixture of reactive and non-reactive (BnOH). In Figure 4-5 (a) we report the temperature sweep results from dynamic analysis for specimens obtained from PDLLA/MMA and PDLLA/IBMA resins by UV-curing in UV-box; in (b) the same traces are normalised. The PDLLA/MMA specimen shows T_g (defined at the tanδ peak) of 62 °C while the PDLLA/IBMA one shows higher T_g at 68 °C. In particular we can notice how the tanδ

curve of the PDLLA/IBMA specimen is much broader than the one observed for the PDLLA/MMA specimen. In Figure 4-5 we also report the average curves for PDLLA specimens as a reference. The average is obtained from eight tests for which we report the results in Chapter 6.

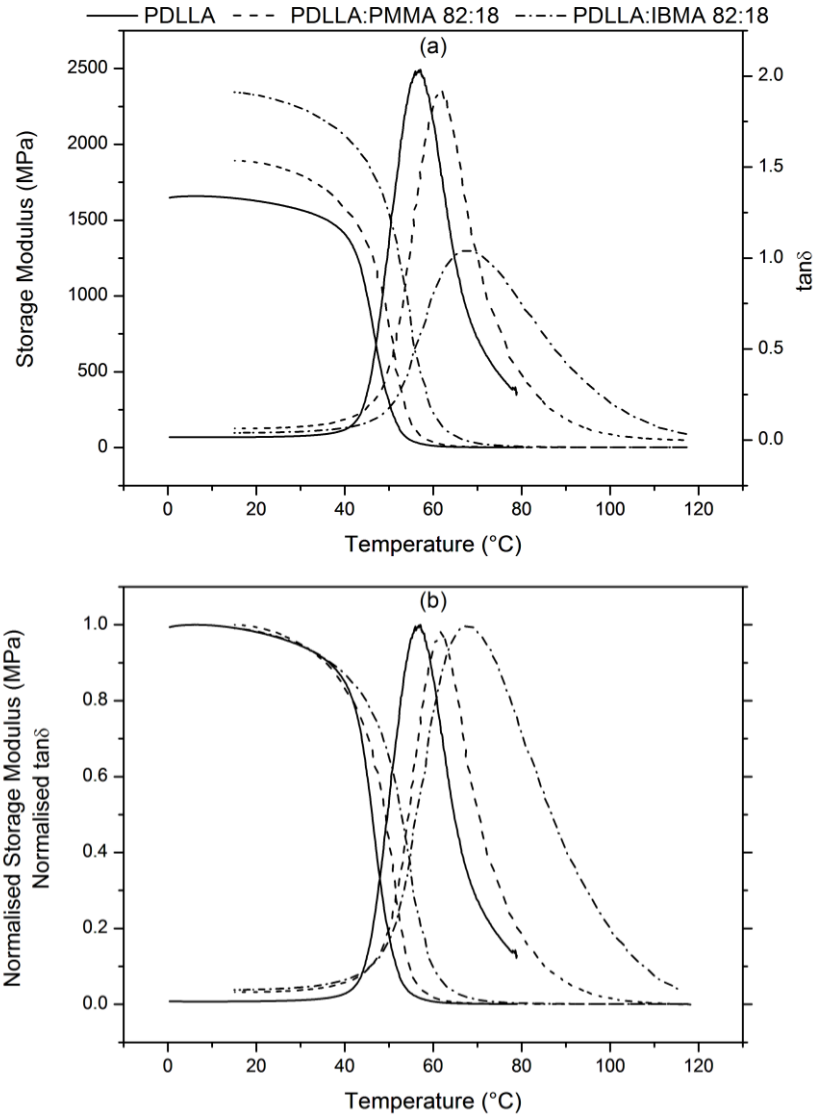

Figure 4-5 (a) DMA traces for film specimens from PDLLA/IBMA, PDLLA/MMA and average traces for PDLLA. (b) The same curves are normalised. The tests are run with film tension clamps on a DMA Q800, at 1Hz 15 μm oscillation, at 2 °C/min heating rate.

Specimen	T_g (°C)	E'_{glassy} (MPa)	$E'_{rubbery}$ (MPa)	FWHM
PDLLA/IBMA	67.6	2344	2.06	30 °
PDLLA/MMA	61.8	1892	1.86	16 °

Table 4-4 Properties from dynamic analysis: T_g is defined at the peak of tanδ; E'_{glassy} is the value of storage modulus at the glassy plateau; $E'_{rubbery}$ is the value of storage modulus at the rubbery plateau; FWHM is the full width at half maximum of tanδ.

4.5 Choice of standard procedure for the preparation of specimens

We fabricated specimens by either curing of an exact geometry by use of the Ember 3D printer projector followed by post-curing, or by the use of moulds and curing in UV-box. Stereolithography parts will generally need post-curing to achieve high gel part. In Figure 4-6 we report the gel part results for five specimens cured on the Ember for 60 seconds, against the results for five different specimens obtained with the same curing followed by post-curing in a UV-box with a curing time of 20 minutes per side. All specimens are from the same batch of resin (BnOH035). The post-curing step does not influence much the specimens mass (M_0) before extraction of the sol part. After extraction and drying we calculate the percentage of gel mass with respect to the maximum value that can be theoretically obtained:

$$w_{gel} = \frac{M_{dry}}{M_M} \tag{4.5}$$

Where M_{dry} is the value of mass after extraction once the specimen can be considered dry (the mass change over one day is negligible) and M_M is the mass of macromer contained in the specimen before extraction, which is calculated multiplying M_0 by the weight concentration of macromer in the resin used for the specimens' fabrication. The average value of w_{gel} for non-post-cured specimens is 74.2% with a standard deviation of 3.86% while for the post-cured ones it results in 96% and 2.16% standard deviation. Additionally to this experiment, we investigated the use of one hour long thermal post-curing (80 °C) following the UV post-curing. For a population of ten, specimens we did not notice a significant difference in w_{gel}.

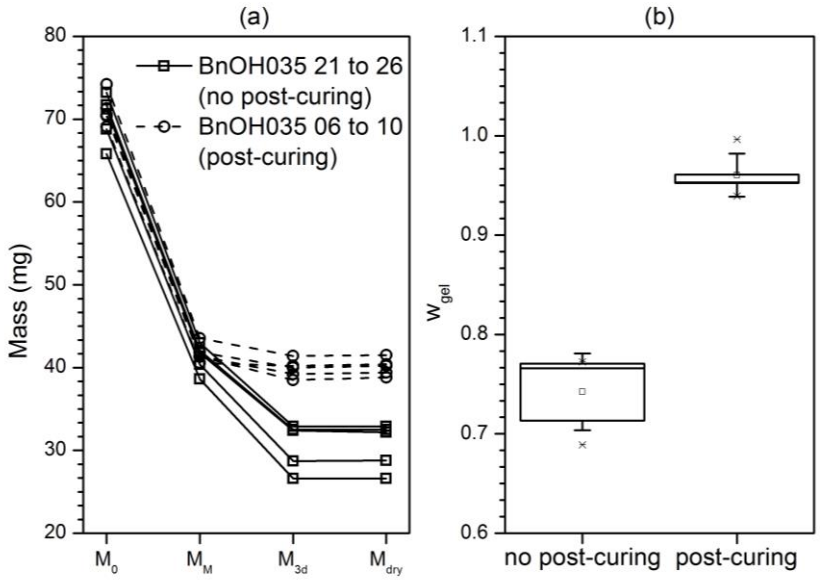

Figure 4-6 (a) The mass of the specimens is taken right before Soxhlet extraction (M_0), after 3 days of extraction and 3 days of drying in oven at 80 °C (M_{3d}) and at steady state (M_{dry}). (b) Distribution of w_{gel}, the ratio of M_{dry} to the mass of macromer theoretically contained in the specimens (M_M).

4.6 Discussion

4.6.1 Changes in molecular weight, synthesised polymers and synthesis procedures throughout the research

We started our research synthesising random copolymers of PDLLA and PCL with target M_n of 5000 g/mol and target glass transition temperature of 37°C. These are not easily dissolved in non-reactive diluents. On the other hand the PDLLA macromer were much more easily dissolved, particularly in DEGDEE and BnOH. To lower viscosity, without lowering the amount of dissolved macromer, we reduced the target molecular weight to 3000 g/mol. This allowed us to formulate resins that can be used on the Ember 3D printer as the viscosity is low enough for any mechanical jamming to be avoided. The main drawback we experienced was a drop in macromer yield as the precipitation process is hindered by the lower molecular weight, leaving part of the polymer in the supernatant. A percentage of this can potentially be recovered by centrifugation, though the benefit in yield hardly compensates for the time and consumables required, as the synthesis of 100 g of macromer results in >2.5 litres of supernatant. During our research we carried out the macromer synthesis employing triethylamine (TEA), which is often used as a proton scavenger for the functionalisation of hydroxyl groups with anhydrides. Still, the use of TEA seems to cause an undesirable yellow colourisation of the final products (and also the formation of some toxic compounds), as suggested in literature [191]. Following what

proposed in the same paper, we switched to the use of K_2CO_3. This, indeed, solved any colourisation issue and fits in our synthesis as this includes a step of washing in water (two consecutive one-day washes in 5 litres of water). The use of K_2CO_3 also presents some advantage if the functionalisation was to be carried out in the melt (120-130 °C) as evaporation is not a concern. In this case the addition of hydroquinone as inhibitor can also help to prevent crosslinking. We did experiment with this and found that the functionalisation time can be cut to around 4 hours. In our circumstances this was not particularly useful as the freeze-drying service would normally take weeks.

4.6.2 Resins containing reactive diluents

The use of methacrylate monomers as reactive diluents is a straightforward way to control the glass transition temperature of the cured networks, additionally it helps in dissolving the macromers given the similarity between the macromer end groups and the monomers. The addition of either MMA or IBMA increased T_g increased towards the target value of 65 °C, though the exact value was not obtained. We can notice that the tanδ curve for the PDLLA/IBMA specimen is much broader than the one of PDLLA/MMA, which has the same shape as the PDLLA average. Furthermore we can notice very similar onset temperatures for tanδ. Usually a broad tanδ curve hints to heterogeneity in the network, for example unevenly crosslinked regions will result in higher and lower mobility and therefore a range of relaxation times (or temperatures). Here we can assume that the PDLLA/IBMA network presents regions poor and rich in PIBMA (the length of PIBMA segments on the kinetic chain is non-uniform) and therefore the heterogeneity of the network is increased which broadens tanδ. At the same time we can assume that the shape of tanδ for the PDLLA/MMA network is the same as the PDLLA one because the MMA monomers react more uniformly with the macromers or the growing chain causing the kinetic chain length and the length between crosslinks to change in a uniform way; additionally, the polymerisation of MMA results in the same structure as the kinetic chain. This would give a similar distribution of relaxation behaviour, only shifted to higher temperatures. The increase in high T_g part might also have less of an effect on the network T_g because of the crosslink points being farther apart which would increase mobility. As for the onset in tanδ being similar for all networks we can assume that this corresponds to the faster relaxation behaviours resulting from the PDLLA chains softening. The temperature for this to happen might not change too much from one network to the other, particularly if the same batch of polymer was employed. Overall we observe two different results that could be exploited in different ways. The simple increase in T_g obtained

through MMA addition might be used to maintain the recovery mechanics of the original network while changing the activation temperature. On the other hand the tanδ broadening through addition of IBMA might be used to change the recovery behaviour. As we already reported, a broad glass transition temperature is associated to multiple shape memory effect.

4.6.3 Specimens curing time

In choosing the specimens preparation procedure we took into account the gel mass as the parameter to confirm good conversion of the macromer into network. When using the Ember 3D printer the steps for the fabrication are necessarily two. First the specimen geometry is formed by spatially-controlled illumination achieved by the printer projector. This step does not reach full conversion, this is generally true for stereolithography. In our case a relatively high (over)exposure time of 60 seconds was used and resulted in only 74% of the macromer mass being converted to network. A post-curing step is therefore required to complete conversion. In our experience longer than 20 minutes post-curing time per side of the specimen does not increase the gel part past the 95%, nor does applying up to one hour of thermal curing at 80 °C following the UV post-curing. The specimens that did not get post-cured show a larger distribution of mass with respect to the post-cured specimens. This most likely relates to optimisation problems with the printer. In particular factors like window clouding (the window is PDMS), uneven light projection and the lack of a levelling legs, mean that not all spatial coordinates are illuminated the same way, affecting the photo-polymerisation.

4.7 Conclusion

We synthesised macromers suitable for the preparation of stereolithography resins. The poly(D,L-lactide-ran-ε-caprolactone) macromers are not easily dissolved in the tested non-reactive diluents and result in viscous resins that easily jam the Ember 3D printer. We could obtain suitable resins from the PDLLA macromers by dissolving in diethylene glycol diethyl ether or benzyl alcohol. Of the two, the BnOH was chosen for most resins because of its very low volatility. The prepared resins were observed to have very good shelf life and maintain their appearance and colour when properly stored in the dark or at low temperature. We investigated the use of reactive diluents to increase the networks T_g and access more shape recovery kinetics than what can be obtained from 100% PDLLA networks. We found that adding methyl methacrylate is a viable option to rise T_g while leaving the material dynamic response qualitatively unchanged. We think this might be exploited in cases in which the PDLLA network shows a desirable recovery behaviour at

a temperature lower than the application one. The addition of IBMA results in higher T_g but also broadens the tanδ curve. In this case we think this could be exploited to achieve multiple-shape memory effect. In isothermal applications this could result in a series of recovery processes activating with the passing of time, which would considerably delay the overall recovery.

Chapter 5 – Evaluation of resins photo-curing behaviour and printing feasibility

5.1 Introduction

This Chapter presents the results obtained from the characterisation of the photo-curing behaviour for the formulated stereolithography resins. It also discusses the results obtained from the printing tests performed in order to evaluate the printability of the resins. The resins were tested and employed to print on two different systems: the Ember, a (out of production) desktop 3D printer by Autodesk and the Perfactory 4 Mini, a professional 3D printer by EnvisionTEC. The photo-curing behaviour was studied by means of stereolithography working curve tests [149], [150]. The resins composition was changed with the objective to obtain light penetration depth (D_p) in the 100 μm range. These compositions were used as starting point for practical printing tests and further modified to enable printing. The printing tests aimed at the fabrication of porous scaffolds and were performed in two phases: first the resins were tested for adhesion to the printer build-head and modified accordingly to the results, then print test parts were printed to test printing feasibility and resolution. In this context printing feasibility means that the process should be obtained with as little as possible supervision from the user, with good reliability and reproducibility. Minimising the printing time was also taken into consideration but it was not one of the main objectives. The printed parts resolution was mostly judged in terms of the overall architecture being reproduced and in terms of porosity occlusion.

5.2 Effect of single components on the photo-curing behaviour and optimal resin composition choice

Each component in the resin mixture influences the photo-curing behaviour and this influence must be understood in order to prototype the best possible resin. These components are: the macromer (PDLLA-2MA); the non-reactive diluent (BnOH); the photo-initiator (TPO); the UV-absorber (BBOT). Of all these components the weight ratio of macromer to diluent should be maximised in order to guarantee that the printed part is mechanically strong so that it withstands the printing process itself and the post-printing process. This is particularly true given the adopted diluent is not reactive and will keep the cured network swollen at all time. We started by adopting a weight ratio of 1.5 as at higher values the macromer starts precipitating. The effect of photo-initiator and UV-absorber will be discussed in the following paragraphs. As a reminder we report the

working curve empirical equation that correlates the cured thickness, C_d, to the dose of energy, E, used to obtain that thickness:

$$C_d = D_p \ln\left({E}/{E_c}\right) \quad (5.1)$$

Where D_p is the above mentioned penetration depth and E_c is the dose of energy that, theoretically, corresponds to the formation of an infinitesimal cured thickness.

5.2.1 Effect of photo-initiator concentration

Figure 5-1 reports the working curves for a resin containing 1, 2 and 3 wt% (mass with respect to total mass of resin) of photoinitiator (TPO). All three resins contain around 0.69 wt% of BBOT as UV-absorber, this is the saturation limit and it is used as standard concentration given that the resins will require UV-absorber to be able to cure into accurate geometries. The results show that increasing concentration of photoinitiator leads to increased penetration depth (D_p) values. On the other hand increasing the photoinitiator concentration decreases the printing time. For example we can observe that printing a 100 μm thick layer will require approximately 10 seconds of exposure time as opposed to around 18 seconds when increasing the photoinitiator concentration from 1 to 2 wt%.

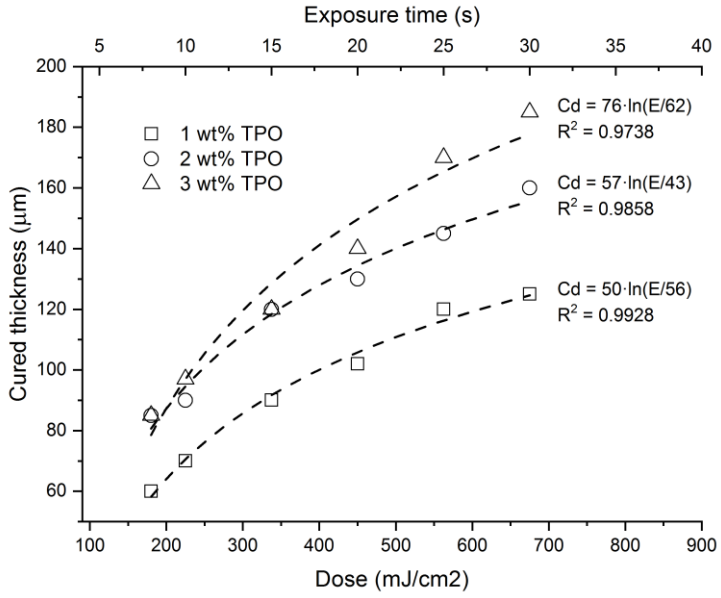

Figure 5-1 Stereolithography working curves for varying concentration of photo-initiator TPO expressed in weight percent with respect to total mass of resin: 1 wt%; 2 wt%; 3 wt%. Higher amount of TPO results in higher values of Dp, while no clear trend can be seen for the critical dose. The dashed lines represent the logarithm fitting which results in Cd = Dp·ln(E/Ec). The amount of BBOT UV absorber in each resin is equal to the saturation concentration, which is around 0.69 wt%. Each data point represents one measurement.

5.2.2 Effect of UV-absorber concentration

Figure 5-2 reports the working curves for resins containing 2 wt% of photoinitiator and concentrations of 0.00, 0.10, 0.15, 0.20 and 0.30 wt% of UV-absorber (BBOT). Increasing the concentration of absorber results in lower values of D_p. With respect to the value of D_p for the absorber-free resin, the addition of 0.10, 0.15, 0.20 and 0.30 wt% UV-absorber results, respectively, in a 54%, 62%, 66% and 71% decrease in D_p. Increasing the weight percentage of UV-absorber also increases the exposure time required to print a layer. From the working curves we can notice that a 100 μm thick layer would be printed in around 7 seconds and 13 seconds for resins containing, respectively, 0.10 wt% and 0.30 wt% UV-absorber. In Figure 5-3 we report the effect of UV-absorber addition on the lateral (XY plane) resolution. A single layer containing a cross-shaped negative detail (a hole) was printed on a microscope glass using a resin containing no UV-absorber (left-most image) and one containing 0.2 wt% of BBOT (right-most image). Using the first resin results in undesirable overcuring along X and Y, drastically lowering the printed layer resolution while the addition of BBOT prevents overcuring so that the edges and corners of the hole are well-reproduced. Additionally the area surrounding the hole, which is a uniform layer of cured resin, is smooth and the voxel pattern can also be discerned.

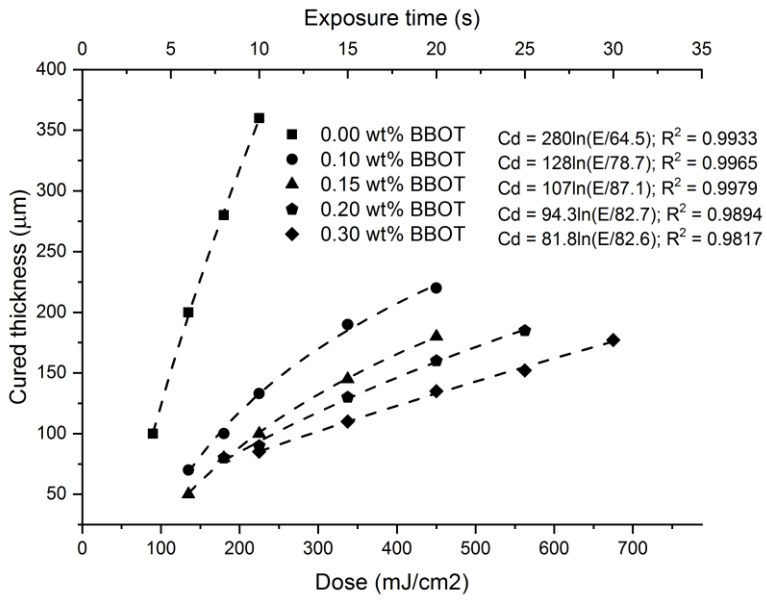

Figure 5-2 Stereolithography working curves with varying BBOT concentration with respect to total mass of resin: 0.00 wt%; 0.15 wt%; 0.20 wt%; 0.30 wt%. The dashed lines represent the logarithm fitting which results in the empirical equation $C_d = D_p \cdot \ln(E/E_c)$. The concentration of photo-initiator TPO is 2 wt% for each resin.

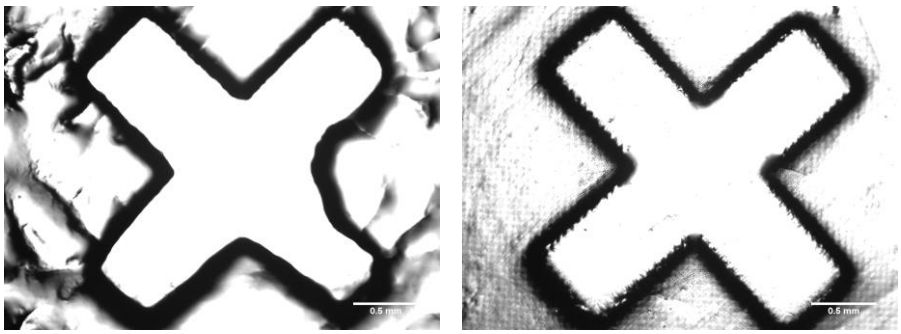

Figure 5-3 Single layer printed on microscope slide. The exposure time was set to 20 seconds. The cross in the middle is a negative detail (a hole), while the rest is solidified resin. The image on the left shows the result obtained when using a resin without UV-absorber; the image on the right shows the same when adding 0.20 wt% of BBOT as UV-absorber. The addition of BBOT results in a much higher level of XY detail as showed by the straight, sharp edges of the cross. Scale bars are 0.50 mm.

5.2.3 Optimal resin composition and print settings choice

The optimal resin composition is reported in Table 5-1, along with the values of photo-curing parameters D_p and E_c and the exposure time required to obtain a 50 and 100 μm thick cured layer (respectively t_{50} and t_{100}). In stereolithography the printed layer height is determined by the build-head step height, since this is the available space for the resin to be cured into a solid layer. The value of light exposure to be used is determined on the basis of the working curve and the chosen step height. The exact value of light exposure to cure a layer of thickness equal to the step height is usually increased by 10% to 100% and as such is used to print. This ensures that each new layer partially cures inside the previous one so that the layers attach to each other and the overall part is mechanically strong. We focused on printing at 50 μm step height, in terms of cured layer thickness, this would correspond to 6.2 seconds of light exposure. We decided to increase this value by at least 50% since the cured networks in our research are swollen by non-reactive diluent and will need more overexposure to form strong parts. The overexposure should be even larger when printing the first layer and few of the succeeding layers.

Resin composition		**Printing parameters**		
Component	**wt%**	**on Ember Desktop 3D Printer**		
PDLLA-2MA	58.6%	**D_p (μm)**	**t_c (s)**	**E_c (mJ/cm^2)**
BnOH	39.1%	90	3.6	82.7
TPO	2.00%	**t_{50} (s)**	**t_{100} (s)**	
BBOT	0.20%	6.2	10.5	

Table 5-1 Optimal resin composition and values of photo-curing parameter relative to tests performed on the Ember 3D printer. Concentrations are weight percentage calculated with respect to total mass of resin. D_p is the penetration depth of the light in the resin; t_c and E_c are, respectively, the critical exposure time and the critical energy dose required to cure an infinitesimally thin layer; t_{50} and t_{100} are, respectively, the exposure time required to obtain a cured layer thickness equal to 50 and 100 μm.

5.3 First layer to build-head attachment and resin composition correction to enable printing

The first layer needs to strongly adhere to the printer build-head for the fabrication process to be successful. Depending on the resin and the print settings the first layer can detach from the build-head right after printing or stick to the tray window causing the printer to jam during the peeling step or causing the part to break. The jamming can also occur because of the resin viscosity being too high depending on the peeling mechanism. The resin reported in Table 5-1 was tested on the Ember 3D printer. Table 5-2 reports the result for seven exposure times. If the first layer printing resulted in detachment from the build-head the exposure time was increased, while it was decreased if the test would result in jamming. After six iterations the change in exposure time giving the two opposite negative results is negligible (0.10 seconds), we can infer that no exposure time will result in successful printing. After testing different compositions it was found that the UV-absorber concentration was the main factor causing the inability to print. It was found that successful attachment to the build-head could be, only sporadically, obtained at very low concentrations of UV-absorber (lower than 0.07 wt%). Considering that a lower value of resin viscosity will reduce the chance of jamming during the peeling mechanism, the macromer to diluent weight ratio was reduced to 1.0. The UV-absorber concentration was also reduced to 0.10 wt% as higher values would still result in the inability to print. Figure 5-4 reports the working curve obtained for the resin after changing the composition as discussed. The value of penetration depth is slightly above 100 μm and from the observed cured thickness values this resin can be expected to work when setting the printer at 50 μm Z step and light exposure between 10 and 15 seconds. Setting the exposure time to 20 seconds, this formulation was found to successfully adhere to the build-head during first layer printing and it was employed to print test parts as reported in the next paragraph.

Iteration	Exposure time (s)	Result
I	10.00	DETACHED
II	11.00	JAMMING
III	10.50	DETACHED
IV	10.75	DETACHED
V	10.90	JAMMING
VI	10.80	DETACHED
VII	10.85	DETACHED

Table 5-2 First layer to build-head attachment results for seven iterations. It is impossible to pin-point a value of exposure time that would result in successful attachment.

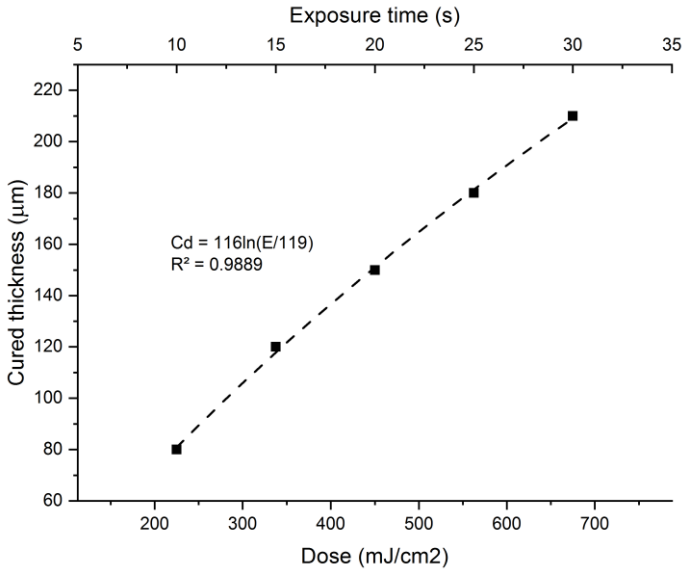

Figure 5-4 Working curve for modified resin. The resin contains 2 wt% of TPO, 0.10 wt% of BBOT, 48.95 wt% of PDLLA-2MA and 48.95 wt% of BnOH.

5.4 Evaluation of continuous printing feasibility on the Ember 3D Printer

Figure 5-5 reports images of two printed test parts. The first is a porous slab of 15x7.5 mm^2 cross-section. The top view reported in image (a) is the last layer to be printed. It can be noticed (image (b)) that the pores edges are straight and the rectangular geometry is well reproduced. From the side view in image (c) it can be observed that the pores are partially occluded. This area corresponds to the first 10 layers that were printed at 20 seconds of light exposure to ensure good adhesion to the build-head and good mechanical strength of the part base. After these ten layers the printing continued with 10 seconds of light exposure. As a result the pores are correctly produced and it is also possible to tell each layer apart from the neighbouring ones. Image (d) shows a magnification of (c) where the voxel pattern forming the part can be noticed. Image (e) shows a 5x5x5 mm^3 cubic pyramid. The printing was completed despite the evident defect propagation. With respect to the correctly printed portion, we can see that the sloped edges are sharp and accurately reproduced. Figure 5-6 reports the top view of a scaffold print test with base of 5x10 mm^2, for a total of 3x6 repeating gyroid units. The part was printed at 12 seconds of light exposure since the very first layer in order to increase accuracy. It can be noticed that the period between each unit is approximately 1.6 mm which corresponds to the designed value. The printing did not progress past 20 layers of 50 µm each. In the right hand image in Figure 5-6, the last layer projected during printing is superimposed onto the scaffold top-view. The areas inside the green contour would typically white while the rest black, here we made both colours transparent. This layer was not successfully printed on top of the previous one, as can be noticed from the top-view of the part. The top-view

of the scaffold was also analysed on ImageJ to evaluate the two-dimensional porosity. In Figure 5-7 we report the cropped section that was used to calculate the porosity on MATLAB by the following script:

```
Img = imread('A051-crop-threshold.png');
Total_area = numel(Img);
Porous_area = numel(find(Img==0));
Porosity = Porous_area/Total_area;
```

The porosity of the cropped section is equal to 70.78% while the design porosity is 70%. The porosity calculated for the entire top-view is higher, 74.83%, as part of the external perimeter seems to be missing. For all tests the printing process was found to be extremely unreliable with parts breaking after few layers. This results in the process needing to be supervised at all times and in considerable volumes of material being wasted. Printing on the Ember can be considered impossible, given that most of the problems can be retraced to the machine jamming during the peeling step the research continued by employing a professional printer.

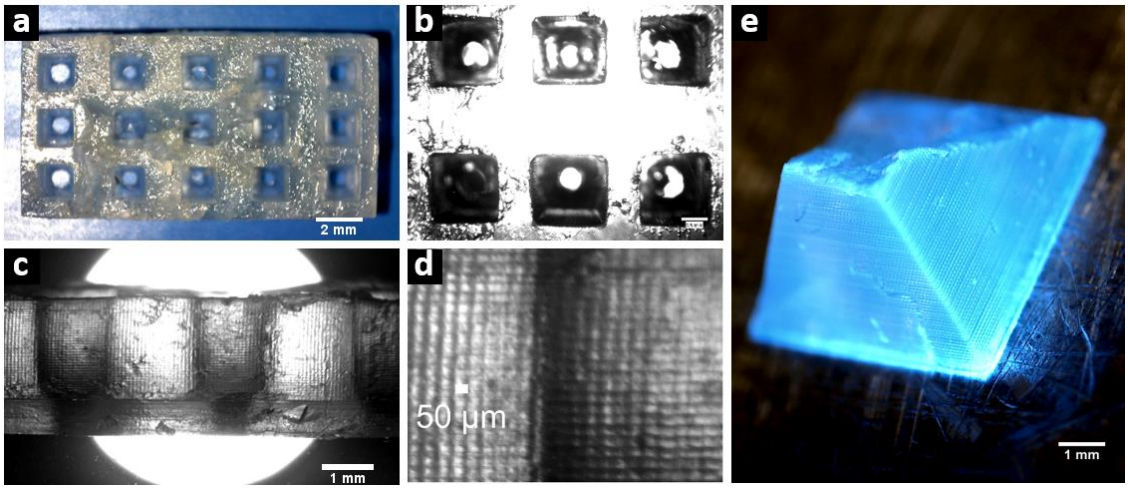

Figure 5-5 Results from printing test parts: a) XY plane view of printed slab with 15x7.5 mm^2 cross-section and 1.5x1.5 mm^2 rectangular straight pores; b) XY plane view under microscope; c) side view under microscope showing the difference in pore size along the Z axis due to overexposed layers; d) magnification of picture c showing the voxel pattern; e) pyramid print test

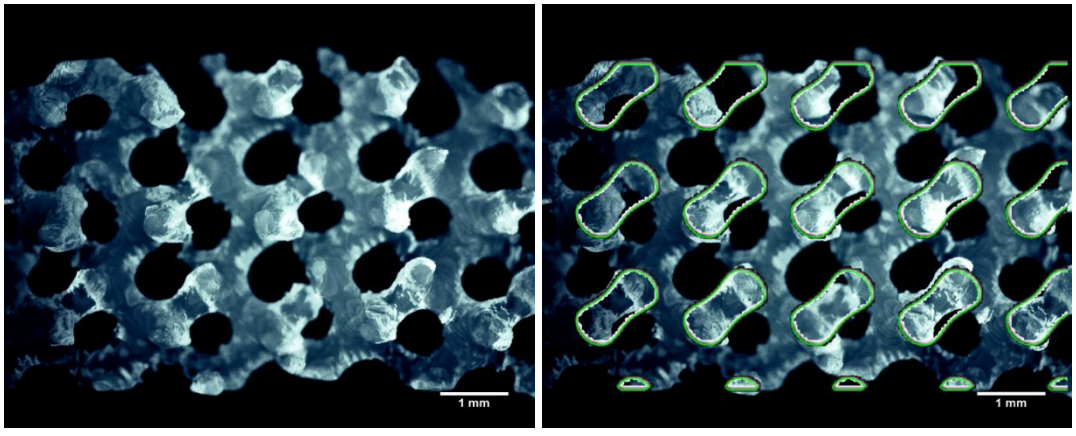

Figure 5-6 XY view of gyroid geometry scaffold print test. On the right the image corresponding to the last layer illuminated was superimposed to the scaffold top-view.

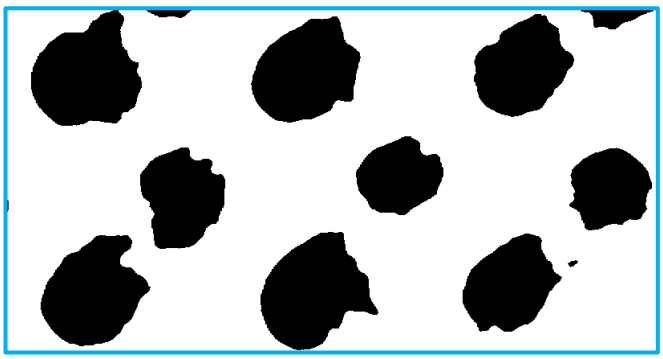

Figure 5-7 Cropped section of scaffold top-view after conversion to 8 bit and application of default threshold on ImageJ.

5.5 Evaluation of printing feasibility on the PerFactory 4 Mini

The Perfactory 4 Mini is a closed source professional DLP printer by EnvisionTEC. There are few factory settings that can be used to start a print job but none of the parameters, such as the exposure time, can be freely changed. The resins were therefore modified in order to cure into a layer thicker than the factory Z step, when exposed to the factory exposure time. Figure 5-8 reports the working curves for the resins compositions that gave the best results. For both resins the weight ratio of macromer to diluent was set to 1.5. The two resins slightly differ for the use of TPO-L or TPO as photo-initiator and the use of different concentrations of both UV-absorber and photo-initiator. Nonetheless they show very similar photo-curing behaviour and gave very similar results so that could be considered interchangeable. With the resins it was possible to readily print test parts of different geometry. Figure 5-9 reports some of the printed parts. Image (a) and (b) are side views of a structure with 0.5x0.25 mm windows. It can be noticed that the windows are partially occluded, though the overall geometry was well reproduced. Image (c) reports a 5x10x5 mm^3 scaffold part made of 6x12x6 gyroid units right after printing, it was found that part of the porosity was occluded. As printing proceeds the resin is trapped inside the geometry which facilitates undesired curing. Image (d) reports a similar structure after extraction of unreacted resin. Some parts of the structure were damaged and the porosity was partially occluded, on the other hand the period between each gyroid unit was well reproduced.

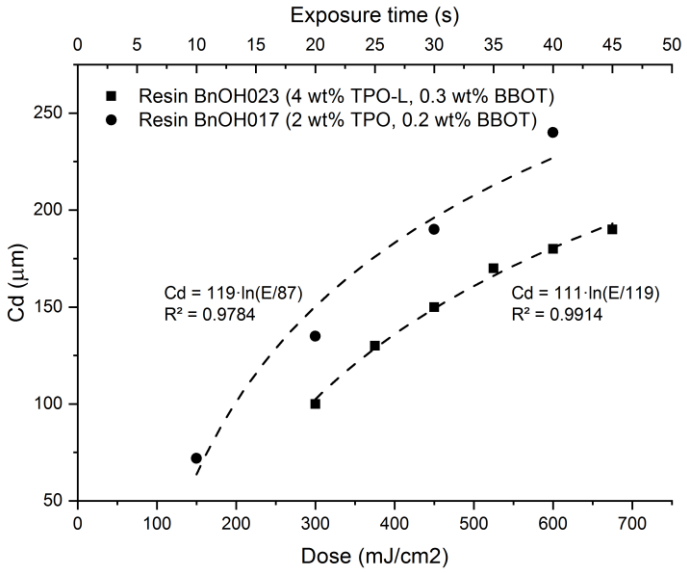

Figure 5-8 Working curves obtained on the Perfactory 4 Mini for resin BnOH017 and BnOH021. The dashed lines represent the logarithm fitting which results in $Cd = D_p \cdot \ln(E/E_c)$. *The obtained equations are reported near the respective curve fit.*

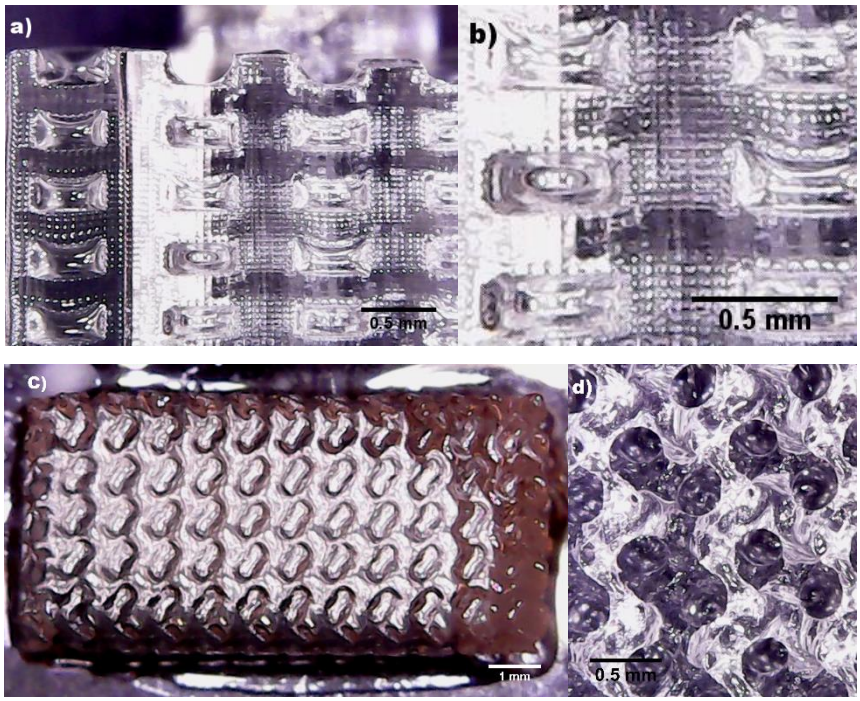

Figure 5-9 Test parts printed on the Perfactory Mini 4: a) structure with windows, the windows are partially occluded as can be seen in magnification b; c) scaffold structure made of 6x12x6 gyroid units just after printing; d) magnification of a similar gyroid architecture after partial extraction of the unreacted resin.

5.6 Discussion

5.6.1 Choice of photo-initiator and UV-absorber concentration

TPO and BBOT were chosen, respectively, as photo-initiator and UV-absorber given that they both absorb in the light spectra of the printers in use and, generally, of many stereolithography printers. In particular we were sure the two components would work with the Ember printer as they are used at least in one of the official Autodesk resins[192].

To test the effect of the TPO concentration on the working curve we decided to use resins containing the maximum possible amount of BBOT as a baseline, as opposed to resins not containing any absorber. It is more significant to carry out the tests this way as the UV-absorber is required to obtain porous structures with good resolution. As we reported the increase in TPO decreases the curing time to cure a certain thickness, this is because the rate of polymerisation is dependent on the concentration of photo-initiator [170], so that larger concentrations will result in the same cured thickness of resin being obtained in less printing time. In our research, we are interested in printing 50-100 μm layer thickness. The results showed that with a 2 wt% concentration of TPO the exposure time required to obtain a 100 μm cured thickness is around 10 seconds. This value is more of an indication of the exposure time per layer and is found to be more than acceptable. There is therefore no gain in increasing the TPO concentration as doing so has the drawback to increase the chance for undesired curing. Decreasing the layer exposure time is also not an effective way to decrease overall printing time as most of this is determined by the printer mechanical movements. For the UV-absorber concentration study we therefore continued to use a 2 wt% concentration of TPO. To choose the BBOT concentration we initially relied on the concentration used in the Ember PR48 resin, which is 0.16 wt% and therefore worked around this value. Clearly adding more BBOT results in a more flat working curve, meaning lower D_p. This helps in terms of obtaining finer details, since a rule of thumb for stereolithography is that $D_p < C_d < 4D_p$ [168], at the same time, as the slope decreases, even small changes in cured thickness will require larger changes in exposure time. This is not practical as, very often, the exposure time needs to be fine-tuned and increased in order to achieve good layer-to-layer attachment. We also considered minimising the risk of toxic species being leftover in the final parts. The final concentration of BBOT was therefore 0.2 wt%, which results in low enough value of D_p and should not require longer than 20 seconds exposure time even when overcuring the resin.

5.6.2 First layer adhesion: use of coatings for build-head and printer window

As we reported, the concentration of BBOT had to be drastically decreased to be able to print on the Ember. Before resorting to this, we tried to work around the problem by changing both the substrate at the build-head and at the printing window. When UV-curing a thin layer of commercial resin PR48 deposited onto the build-head, the cured solid adheres strongly to the surface while our resin prototype can be easily detached by slightly pushing on the side. This is likely due to the fact that the commercial resin is

completely made of reactive material, oligomers and monomers, while our resins form highly swollen networks, therefore creating less adhesive bonds (mechanical bonds) per unit of surface. At the same time, our resin has stronger adhesion to some commercial resins in our possession than to the build-head aluminium surface. We therefore printed a single layer of commercial resin PR48 on the head, this can increase adhesion as any unreacted part on the surface contains unsaturated moieties that can form chemical bonds with our curing resin. With respect to the jamming, this can be caused by excessive viscosity or it can be the result of the cured layer strongly adhering to the printer window. In theory, the PDMS surface of the Ember window acts as an oxygen buffer which creates a dead zone for the polymerisation reaction due to oxygen inhibition. In our experience, this system is not particularly effective and several commercial resins including the Autodesk ones can adhere to the window causing printing failure. We therefore decided to coat the window with Teflon (replacement films for Titan, Kudo3D; sheets from Chemours, Dupont). We tested the first layer printing with all combinations of coated build-head and Teflon coated window. In the end the BBOT concentration still had to be lowered to notice any difference resulting from the two modifications, at the lower concentrations of absorber the use of Teflon did make the printing more reliable while coating the build-head did not have a significant effect.

5.7 Conclusions

It was found that the desired resin formulation could not be employed to print on the Ember desktop 3D printer. The results show that this is due to the UV-absorber concentration being in excess of very low values (0.07 wt%). To achieve printing the content of diluent needs to be increased by around 10 wt% and the concentration of UV-absorber needs to be reduced by 0.10 wt%. The obtained formulation cures into weaker networks and the overall printing process is too unreliable to consider. We can conclude that printing with our resins on the Ember is not feasible. On the other hand printing on the Perfactory 4 Mini is readily achievable without any supervision from the user, aside from the initial steps. In this case the resins were changed in order to match the factory settings of the printer, though the use of custom settings should not be excluded as it is a service that EnvisionTEC can provide.

Chapter 6 – Thermorheological characterisation of PDLLA networks: acquisition of experimental data for modelling and evaluation of reproducibility of the material properties

6.1 Introduction

In this Chapter we discuss the results from the material characterisation obtained mostly through means of dynamic mechanical analysis on the DMA Q800. We also report the results from the investigation of the gel part for a large population of UV-cured specimens with focus on the ones that were used for the material shape memory behaviour modelling; as the gel content has influence over the material properties we find these results are best to be reported in this Chapter. Moreover, our investigation showed a large spread in the specimens' response to dynamic analysis, with the values of glass transition temperature and moduli in the glassy and rubbery region all varying in large ranges. This Chapter, therefore, focuses on evaluating if this result can be correlated to the specimens' fabrication methodology or other possible causes of error. Subsequently we also report experiments we carried out on the DMA Q800 employing a factory-produced material to evaluate if significant errors can be introduced by the equipment itself. Additionally we originally intended to quantitatively study the shape memory behaviour of the material on the DMA Q800 – as often found in literature, e.g. [8], [13], [75], [104], [193]–[197] – though the results obtained from the free recovery analysis (recovery in unconstrained conditions) were not consistent with what observed for experiments carried out in oven, incubator or controlled temperature room. Here we present these results, focusing on discussing how they are unexpected given other experimental observations, if they can be considered valid at least from the qualitative point of view and the possible cause behind the inconsistency.

We can summarise the objectives for the research here reported as:

1. Characterisation of the material viscoelasticity behaviour in order to obtain the experimental data required for the predictive model;
2. Analysis of reproducibility for the obtained material properties to establish if the results are suitable to accurately model the material viscoelasticity;
3. Investigate the error intrinsic to the characterisation methodology adopted including errors related to the equipment employed, with focus on the 3D printing device and the dynamic mechanical analyser in use;

4. Investigate the shape memory behaviour of the material by means of shape memory cycle on the DMA Q800: originally with the main intention of comparing the experimental results to the model predictions;

Here we briefly recapitulate the tests and methodology we carried out in this part of the research.

We characterised the specimens by Dynamic Mechanical Thermal Analysis on the TA Instruments DMA Q800. We chose to run most experiments in tension mode as this is a typical methodology found in shape memory polymers related literature (e.g. [8], [104], [113], [198]). Some of the advantages of using this mode lies in the fact that the specimens required have film-like geometry. This means that they can be regarded as two dimensional which could simplify future modelling, they also require very low amount of resin so that a large amount of specimens can be obtained from the same batch of resin, eliminating one possible variable from the reproducibility analysis. Furthermore the specimens can be obtained by curing on the Ember 3D printer using exactly the same resin that one would use for continuous printing. As opposed to this, thicker specimens should be obtained by UV-box curing in a mould with resin not containing UV-absorber to allow for the entire thickness to be cured. Additionally the films do not require long extraction nor long drying time.

For the viscoelasticity characterisation, we ran temperature ramp tests on the DMA by cycling three times between 0 and 80 °C at 2 °C/min with a frequency of 1 Hz and 15 μm oscillation amplitude; we obtained the values of glass transition temperature as well as the values of storage modulus and of loss modulus from the third heating ramp, which is common practice. We also investigated the glass transition temperature by means of differential scanning calorimetry through cycles of heating and cooling ramps at 5 °C/min.

We carried out stress relaxation tests at different temperatures in order to build a relaxation modulus master curve which could be used in the material modelling. Even though we report these results in this Chapter and their use later in Chapter 8, we should notice that the tests were carried out for a different specimen geometry, i.e. slab-like, obtained by UV-box curing only, employing an older resin prototype and on the DMA in single cantilever mode. The tests were deemed to be not material-effective, nor time-effective and were discontinued. Nonetheless they represent one way to obtain the experimental data required for modelling, particularly to obtain experimental values of shifting factor and are worth discussing and being contextualised with the other results from dynamic analysis.

We also employed the DMA to characterise the shape recovery behaviour of the networks. Although we did perform these characterisations and obtained results for different recovery temperatures that are qualitatively and quantitatively consistent when compared one to each other, the recovery was found to proceed at relatively fast pace for temperatures well below the average $T_{g,}$ at which one would expect the shape to be fixed. Finally, we kept track of the mass of several specimens during the fabrication process so that we could calculate the gel content and make sure that the specimens would be free from solvent.

6.2 Mass distribution before and after extraction and after drying for 30 specimens produced from resin BnOH035: calculation of gel part

In this section we present the results relative to the mass of the networks after UV curing and postcuring and after extraction and drying. All specimens here reported and generally all specimens employed for the characterisations, were obtained following the same procedures as per the Material and Methods section of this Thesis. The mass values of interest are: M_0 the mass of the specimen after curing and post-curing; M_M the maximum mass of gel we can expect to have in the cured specimen, which is obtained from the weight percentage of macromer in the resin; M_{3d} the mass after Soxhlet extraction followed by 3 days of oven drying at 80 °C; M_{dry} the value of mass reached once the mass change due to drying is negligible, this is usually the mass after 4 days of drying for the film-shaped specimens. From the value of M_{dry} and M_M we calculate:

$$w_{gel} = M_{dry}/M_M \qquad (6.1)$$

This value is the percentage of gel mass with respect to what could be theoretically measured given the concentration of polymerisable material initially contained in the resin. Figure 6-1 (a) reports the distribution of the values of M_0 for 30 film-shaped specimens. In Figure 6-1 (b) we report the distribution of $M_{M,}$ M_{3d} and M_{dry}. The distribution of w_{gel} is reported in Figure 6-1 (c). The 30 specimens are all obtained from the same stereolithography resin, BnOH035. The specimen's mass is stable after 3 days of drying so that the mass at the fourth day can usually be taken as the dry one. The remaining mass after extraction is lower than what could be expected if all the macromer was to react and form a crosslinked network. We measured w_{gel} = 92.3% ± 2.65% SD. This means that 54.2 wt% ± 1.55 wt% SD of the resin mass was crosslinked, whereas the theoretical fraction of macromer in the resin is equal to 58.68 wt%. In Figure 6-2 we report the distribution of and the exact values of M_0, $M_{M,}$ M_{3d}, M_{dry} and w_{gel}. for the 7 specimens that were characterised on the DMA to obtain the temperature sweep data for

the model parameters identification. These specimens (BnOH035: 004, 006, 007, 008, 010, 028, 029) belong to the same population as for Figure 6-1. As we can notice the specimens belong to the higher range of w_{gel} values of the entire population (around the +1.5 SD range, with respect to Figure 6-1 (c). This was not intended, the choice of the specimens was related to the absence of defects on the same and to the thickness being mostly constant across the length. We should also notice that each film specimen that went through curing and post-curing was then cut in two halves and each half was used for DMA or other characterisations. The values of mass are relative to each single film before being cut.

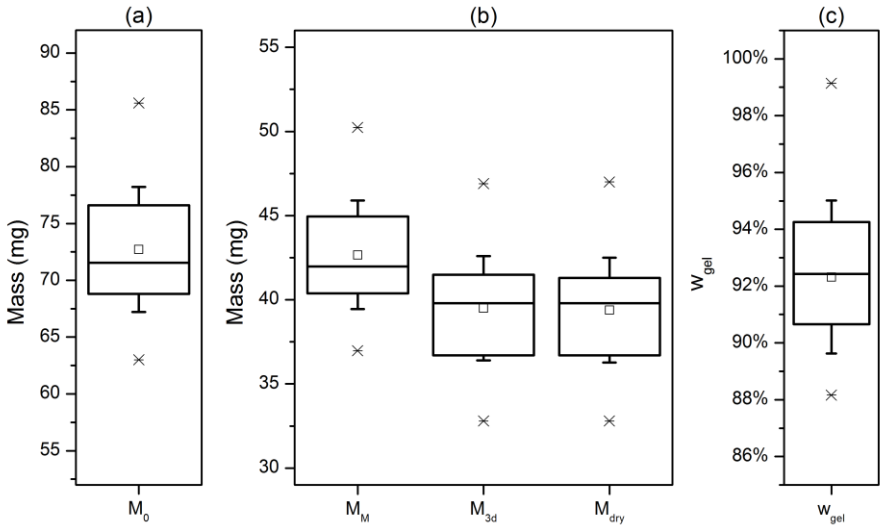

Figure 6-1 Mass data for n=30 PDLLA film specimens. (a) Distribution of M_0, the mass of the specimen after UV curing and post-curing. (b) Distribution of: M_M, the theoretical maximum value of polymerisable mass; M_{3d}, the specimen mass after extraction and 3 days of drying at 80 °C; M_{dry}, the specimen mass after 4 days of drying. (c) Distribution of w_{gel}, the ratio M_{dry}/M_M.

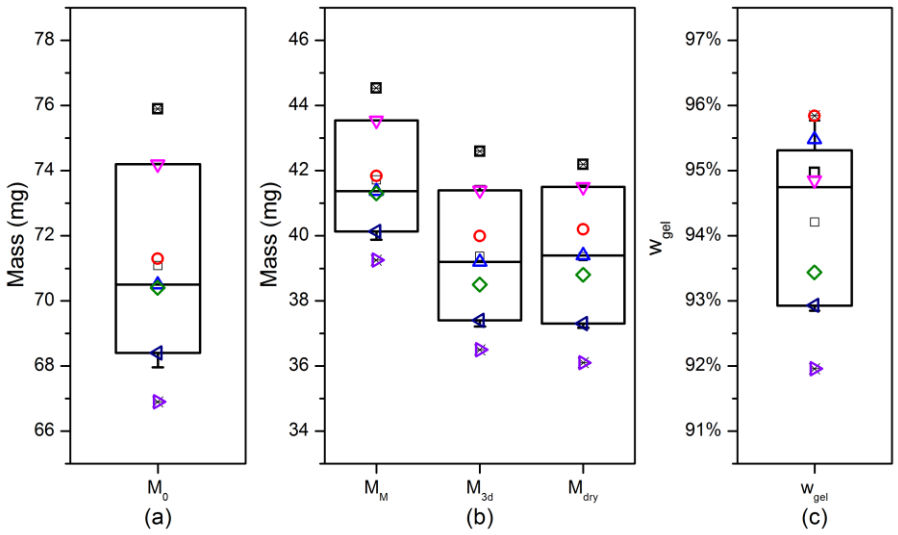

Figure 6-2 Mass data for n=7 specimens belonging to the same data-set of Figure 6-4 and that were used for the main temperature sweep characterisations in order to identify the model parameters. (a), (b) and (c) defined as per Figure 6-4. Each symbol represents one of the specimens.

6.3 Results from the temperature sweep dynamic analysis for 8 specimens with film geometry obtained from resin BnOH035: acquisition of experimental data required for the material modelling and observations over the reproducibility of the material mechanical response

In this section we present the dynamic analysis results obtained from the temperature sweep tests conducted for eight film-shaped specimens. The data obtained from these specimens was later employed to model the viscoelastic behaviour of the material. The eight film-shaped specimens are part of the population discussed in the previous paragraph and were chosen primarily because free from defects and uniform in thickness and width. Specifically, these are the specimens whose mass values distribution during fabrication is represented in Figure 6-2. During processing the films have a length of 50 mm and are then cut into two halves to be used in DMA analysis, as already explained. Figure 6-2 reports seven data-points and not eight because specimens 029 and 029b are the two halves of the same film. Figure 6-3 represents the typical plot of storage modulus (E′) and tanδ against temperature, as obtained from a heating and cooling cycle between 0 and 80 °C on the DMA. Labelled in the plot are the parameters: E'_{glassy} and $E'_{rubbery}$, respectively, the plateau value of storage modulus at low temperature and the value of the plateau at high temperature; T_g, the value of temperature corresponding to the peak in tanδ during heating, which is taken as the value of glass transition temperature. We can notice that the cooling curves are shifted to the left, which results in the value of temperature at the tanδ peak, $T_{g,c}$, being around 20 °C lower than T_g. As previously stated,

we performed three consecutive cooling and heating temperature sweeps for each specimen characterisation. Here, we take into consideration the data from the last heating ramp; even though the full cycles are not here reported, we can notice that the values of $E'_{rubbery}$, E'_{glassy} and T_g are close to constant throughout the three heating ramps. In Figure 6-4 (a) and (b) we report, respectively, the curves of storage modulus against temperature and of tanδ against temperature for the eight specimens. The values of E'_{glassy}, $E'_{rubbery}$ and T_g were extrapolated for each specimen and their distribution is reported in Figure 6-4 (b), (c) and (d), respectively, while the exact values are reported in Table 6-1. The results are not reproducible within each other, all three sets of data are spread over large ranges, in particular the values of T_g cover a 8 ° range with a standard deviation of 2.3 °C. It is worth noticing that all measured values of glass transition temperature are close or above 56 °C except for one which is noticeably lower at 53.3 °C. In Figure 6-5 we plotted the values of E'_{glassy}, $E'_{rubbery}$ and T_g against the values of w_{gel} for the specimens. There is no significant correlation between the values of w_{gel} and the values of either E'_{glassy}, $E'_{rubbery}$ or T_g. In general we also did not find any significant correlation between any XY pair of parameters. Furthermore we can notice that specimens 029 and 029b, which were obtained as two halves of the same UV-cured film, are characterised by very different values of T_g, $E'_{rubbery}$ and E'_{glassy}.

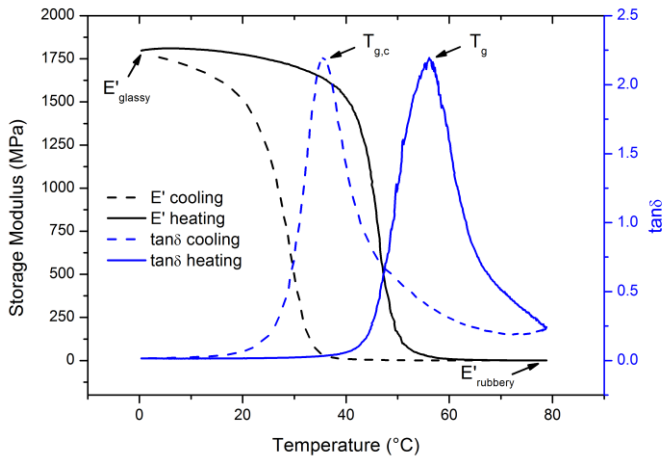

Figure 6-3 Heating and cooling trace of storage modulus and tanδ against temperature as obtained from DMA experiments. The temperature was ramped between 80 and 0 °C at 2 °C/min. Labelled in the plot are: E'_{glassy}, the value of storage modulus plateau at low temperature; $E'_{rubbery}$, the value of the plateau at high temperature; T_g the glass transition temperature taken as the temperature at the tanδ peak during heating; $T_{g,c}$, the temperature at the tanδ peak during cooling.

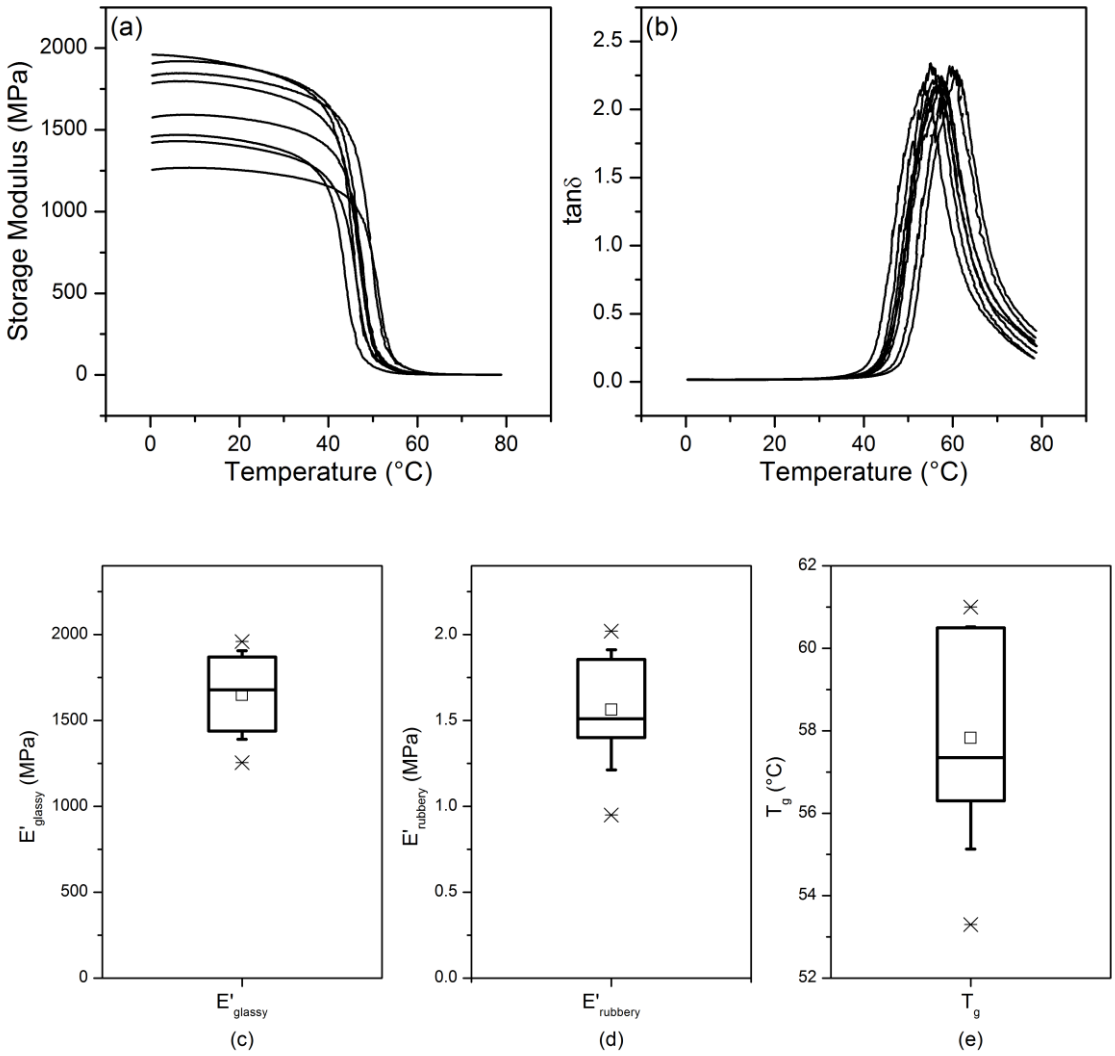

Figure 6-4 (a) The storage modulus curves and (b) the tanδ curves for the eight specimens under analysis; (c), (d) and (e) distribution of, respectively, E'_{glassy}, $E'_{rubbery}$ and T_g values for the same specimens.

Specimen	E'_{glassy} (MPa)	$E'_{rubbery}$ (MPa)	T_g (°C)	w_{gel}
BnOH035 004	1575	1.56	57.8	94.97%
BnOH035 006b	1255	1.46	61	95.84%
BnOH035 007	1833	2.02	61	95.48%
BnOH035 008b	1420	1.39	56.9	94.85%
BnOH035 010b	1960	1.72	60	93.44%
BnOH035 028	1906	1.99	56.4	92.93%
*BnOH035 029**	1458	1.41	53.3	91.96%
*BnOH035 029b**	1782	0.95	56.2	91.96%

*Table 6-1 Values of storage modulus at the glassy and rubbery plateau and values of glass transition temperature (temperature corresponding to tanδ peak) as obtained from DMA measurements for eigth BnOH035 specimens. Values of E'_{glassy} are taken at 0 °C while values of $E'_{rubbery}$ are taken at 80 °C. * BnOH035 029 and 029b are two halves cut from the same specimen.*

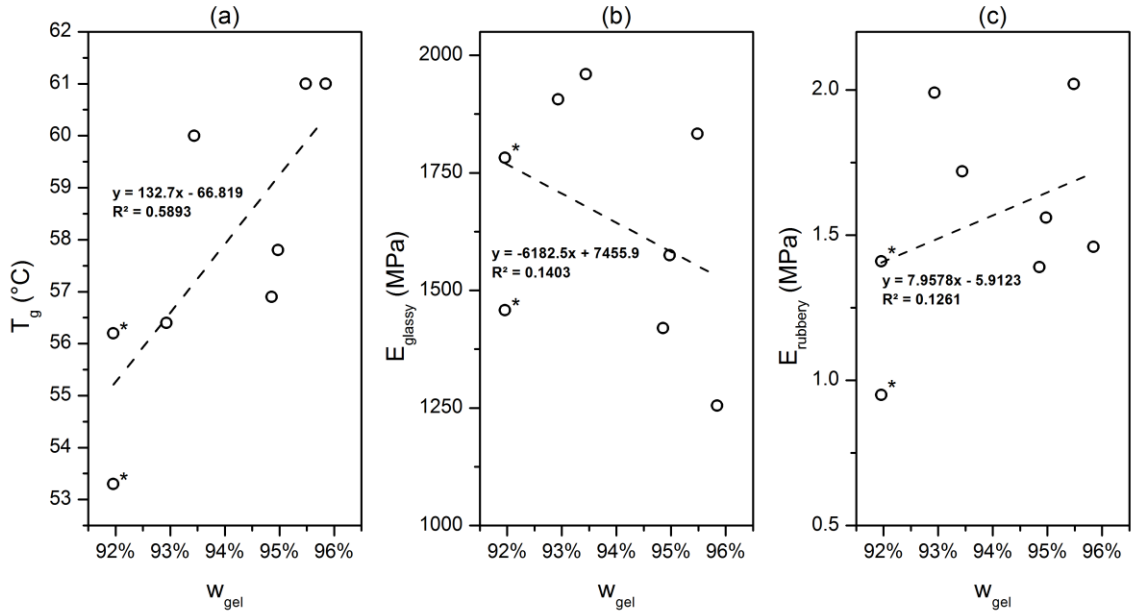

Figure 6-5 The values of (a) T_g, (b) E'_{glassy}, (c) $E'_{rubbery}$ are plotted against the values of w_{gel} for all specimens. The dashed lines represent the linear fit with equation and R^2 value as reported. The asterisk (*) near the data points indicate the specimens BnOH035 029 and 029b.

6.4 Results from differential scanning calorimetry for specimens from resin BnOH035

Here we report the results from the calorimetry analysis for specimens obtained from resin BnOH035 and belonging to the same population discussed in the first paragraph. For all specimens we performed a first heating ramp at 5 °C/min to 80 °C, followed by a cooling ramp and a second heating ramp. The cooling rate could not be accurately controlled by the machine but we can still estimate 5-7 °C/min. For all specimens, we obtained the reported results from the second heating ramp which was performed at 5 °C/min. In Figure 6-6 (a) we report the typical trace of heat flow against temperature obtained for the specimens. All specimens showed a second order transition in the range between 40 and 55 °C. The values of glass transition temperature were calculated at the inflection point of the heat flow curve by plotting the second derivative of the heat flow against the temperature and are reported in Table 6-2. We can see from Figure 6-6 (b) that the values of T_g are distributed on approximately a 3 °C range between 47 and 50 °C. We can also notice that the values are generally lower than the ones obtained from the DMA analysis, with an average T_g of 48.7 °C whereas the average for dynamic analysis is almost 10 °C higher. This kind of result can be expected when comparing T_g calculated from the two different methodologies [194][199].

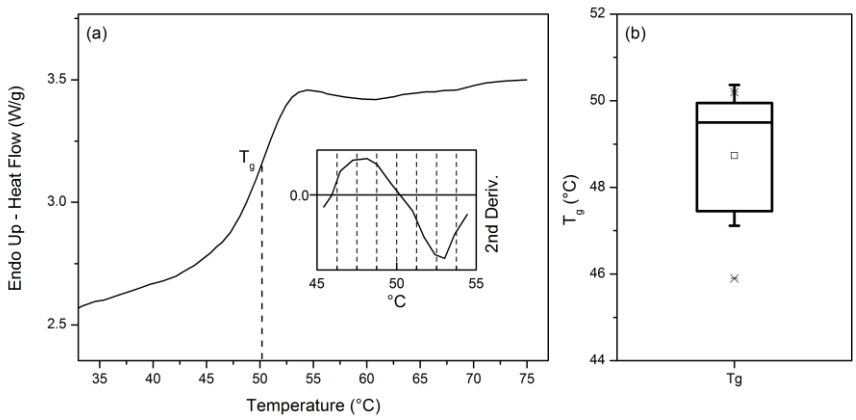

Figure 6-6 (a) Typical trace of heat flow against temperature obtained from DSC second heating ramp at 5 °C/min, only the part of the data is here reported. The inset graph represents the heat flow second derivative. The value of glass transition temperature, T_g, is here defined as the temperature at which the second derivative is zero (the heat flow curve inflection point). In (b) the distribution of the values of T_g is reported as a box chart.

Specimen	**T_g (°C)**
PLA100 BnOH035 DSC001	45.9
PLA100 BnOH035 DSC002	50.2
PLA100 BnOH035 DSC003	49.5
PLA100 BnOH035 DSC004	50.1
PLA100 BnOH035 DSC005	49.5
PLA100 BnOH035 DSC006	48.1
PLA100 BnOH035 DSC007	46.8
PLA100 BnOH035 DSC008	49.8

Table 6-2 Values of glass transition temperature calculated from DSC analysis for eight specimens obtained from resin BnOH035.

6.5 Results from stress relaxation experiments performed on the DMA Q800 in single cantilever mode for specimens with slab geometry, construction of stress relaxation modulus master curve and observations over reproducibility

The stress relaxation experiments were carried out in the initial phase of this research with samples obtained from resins that are different from the ones used to date, in that they were formulated with a different diluent and did not contain UV-absorber. The testing was carried out in single cantilever mode, using specimens with slab-like geometry produced by UV-curing in PTFE moulds of dimensions 40x13x3.0 mm^3. The fabrication methodology and the relatively large thickness are the reason why the resin used was UV-absorber-free, as the light needs to be able to penetrate the whole thickness. The slab specimens went through extraction and drying for longer times than the film specimens, given their larger volume. After drying the final dimensions for the specimens would be around 20% lower than the dimensions of the mould, as a result of shrinking. We should also remember that the length of the specimen during testing is the clamped length, for the DMA Q800 set of cantilever clamps in use this is equal to approximately

17.5 mm. The stress relaxation isotherms were obtained by running two separate time-temperature superposition tests (the test is built-in for the DMA Q800) for two different slab specimens obtained from the same resin through the same fabrication methodology. The first test repeated the stress relaxation step for temperatures from -20 to 40 °C, the data at -20, 35 and 40 °C was discarded. The second test was run from 35 to 100 °C, with only the data from 35 to 50 °C being used. Each relaxation test lasted for 10 minutes and the temperature increment between each iteration was set to 5 °C. In Figure 6-7 (a) and (b) we report the stress relaxation modulus curves for temperatures going from -15 to 50 °C at intervals of 5 °C. The modulus at low temperatures starts from values of around 3 GPa, it drops under 1 GPa at 30 °C and to the order of 1 MPa at 45 and 50 °C. The qualitative behaviour is comparable to what observed for the dynamic analysis, in that the modulus starts dropping around 30-40 °C and once at 50 °C is already entering the rubbery plateau. The stress relaxation curves were obtained for the main purpose of building the stress relaxation modulus master curve, which is part of one of the possible methodologies to identify the material's parameters that are required for the viscoelasticity modelling. To obtain the master curve the isotherms were manually shifted as this was found to be easier and more efficient than using an algorithm. In Figure 6-8 (a) and (b) we report the master curve when the reference isotherm is chosen to be at 15 °C, one plot being in semi-log scale and the other in log-log scale. The same qualitative curve would be obtained at any other temperature, though the reduced time range would change. We did not obtain a perfect superposition for most of the curves and some parts of the master curve were left unfilled.

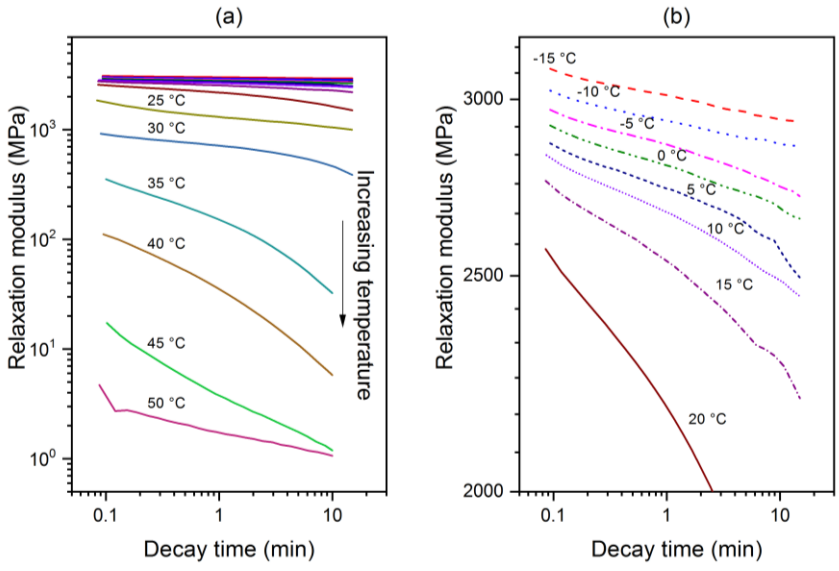

Figure 6-7 Stress relaxation modulus against decay time obtained from DMA analysis. Each curve is the result from one isothermal test, the lowest temperature being -15 °C and the highest 50 °C, the temperature increment is 5 °C. The experiments at temperatures from -15 to 30 °C are carried out with a 0.1% strain, for all other experiments the displacement was increased to 0.5%. In (b) we report the curves for the lowest temperatures.

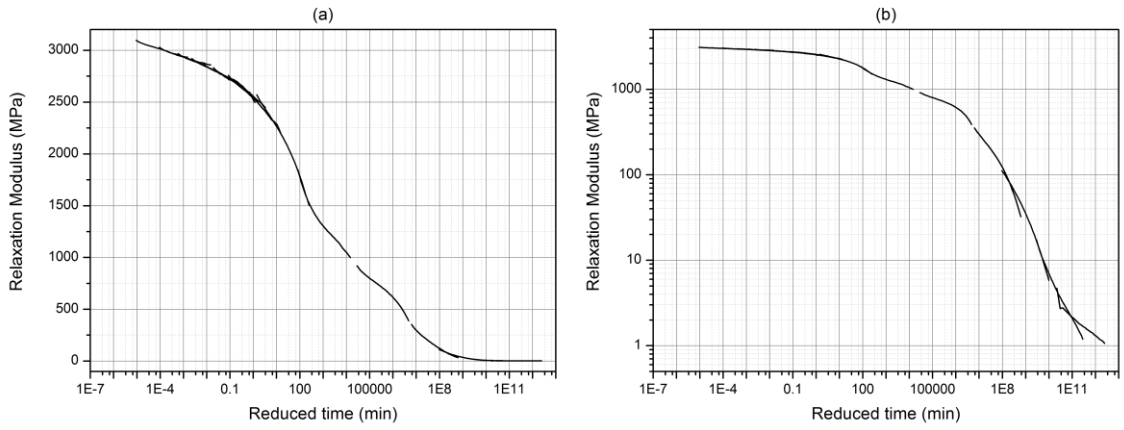

Figure 6-8 Relaxation modulus master curve obtained by horizontal shifting of the isotherms with respect to the one at 15 °C. (a) Relaxation modulus reported in linear scale; (b) Relaxation modulus reported in logarithm scale

6.6 Shape memory programming on the DMA Q800 in strain rate mode

The shape programming was conducted on the DMA by means of a custom made method in strain rate mode, with tension clamps and the same film geometry specimens. In Figure 6-9 we report the stress, strain and temperature curves against time for one shape programming experiment, in this case the film specimen was obtained from resin BnOH035. We also labelled the different steps (A, B, C, D) of the programming and some points of interest ("i", "ii", "iii"), for ease of discussion. To briefly recapitulate the programming: in A and B the temperature is increased to 80 °C at 3 °C/min and kept constant for one hour to achieve equilibrium; in C the specimen is strained instantaneously by 10% and kept in isothermal and isostrain condition for one hour; in D the temperature is quickly (around -30 °C/min) decreased to 0 °C, while still in isostrain condition and then kept constant for one hour. During the initial equilibration step we noticed that the strain increases to values that can be as small as 0.1% and as large as 7% (see "i"). For some experiments we also noticed a sudden strain drop near the end of the heating ramp. This does not correspond to a drop in length or shaft position; we can assume that the Q800 is performing a (non-programmed) measure length segment, which resets the strain to zero. For all experiments, step B was found to be long enough for the length to stabilize. Just before the loading step (at point "ii") we programmed a measure length segment, without this command the DMA would apply a 10% strain with respect to the initial length of the specimen which would not take into account the change in length during equilibration. We can notice that the length after loading is 8.55 mm while the value before loading is 7.77 mm, therefore the correct amount of strain has been applied to the specimen. During step D we noticed a large increase in stress or, in other terms, an increase in the force required to maintain the 10% strain. This increase reaches

maximum values in the range of 1-10 N. In the same step the strain first drops by typically as much as 0.1% and is brought back to 9.99% by the end of the step.

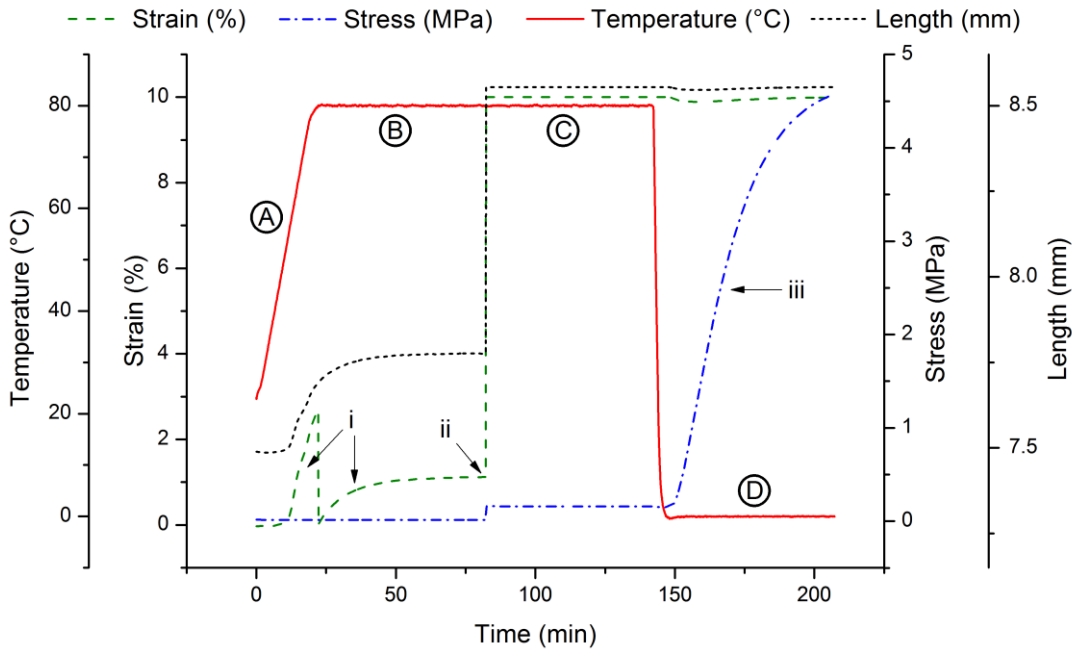

Figure 6-9 Example of shape programming of PDLLA network performed on the DMA Q800 by means of a custom method in strain rate mod and tension clamps. The capitalised letters denote the different steps during programming: A) temperature ramp from room temperature to T_h (80 °C); B) 60 min isothermal step to complete equilibration; C) 60 min isothermal and isostrain step following loading to achieve 10% strain; D) cooling ramp to T_c (0 °C) followed by 60 min isothermal. Roman numerals represent points of interest: i) strain increase during equilibration step; ii) instantaneous loading; iii) stress increase during cold temperature isotherm.

6.7 Results for shape recovery cycles performed on the DMA Q800 at different recovery temperatures

Several film specimens were tested for their shape memory behaviour through shape memory cycles on the DMA Q800 by employing custom methods with strain rate module. The shape programming step was the same as what discussed in the previous paragraph, during the recovery step we then brought the specimens to isothermal conditions and ran the experiments long enough for most of the deformation to be recovered.

In Figure 6-10 we report the DMA traces for shape recovery steps for recovery temperature of 45 °C, as a reference example. In general we noticed that the instantaneous unloading after the cold step resulted in loss of strain. This is usually referred to as a spring-back of the shape memory material and relates to the shape fixity ratio through the equation:

$$R_f = \frac{\varepsilon_{max} - \Delta\varepsilon}{\varepsilon_{max}}$$

Where $\Delta\varepsilon$ is the drop in strain and ε_{max} is the programmed strain. For our experiments, given the strain decrease during the programming step, we calculated the shape fixity as:

$$R_f = \frac{\varepsilon_0}{\varepsilon_{max}}$$

Where ε_0 is the strain right after unloading which will be the same as $\varepsilon_{max} - \Delta\varepsilon$ as long as the strain before unloading is still equal to ε_{max}. For all shape memory cycles carried out on the DMA we noticed high R_f values of usually 97%. For all tests, after the unloading the temperature was increased at a constant rate of 5 °C/min until the recovery temperature was reached. At the beginning of the heating we noticed that the strain increased, sometimes to higher values than 10%, it then started decreasing as the recovery temperature is reached. The recovery process is quantified and studied through the use of the recovery ratio function R_r, as previously introduced this is calculated as:

$$R_r(t) = 1 - \frac{\varepsilon(t)}{\varepsilon_0}$$

Where $\varepsilon(t)$ is the strain at a certain time. In Figure 6-11 the recovery steps for three experiments are reported in terms of the recovery ratio. The experiments were carried out at three different recovery temperature of 37, 40 and 45 °C. Higher recovery temperatures corresponded to faster recovery of the deformation. For the recovery carried out at 40 and 45 °C, $R_r(t)$ reached a plateau by the end of the experiment with values of 92% and 99% respectively. For both cases we can notice that most of the deformation was recovered in a ten to twenty minutes interval. The recovery experiment at 37 °C reached a value of R_r equal to 80% after 35 hours. We notice for this experiment the logarithmic growth of R_r is much slower than what observed at the higher temperatures and that the plateau value seems to be around 80%, which leaves a residual deformation of 20%.

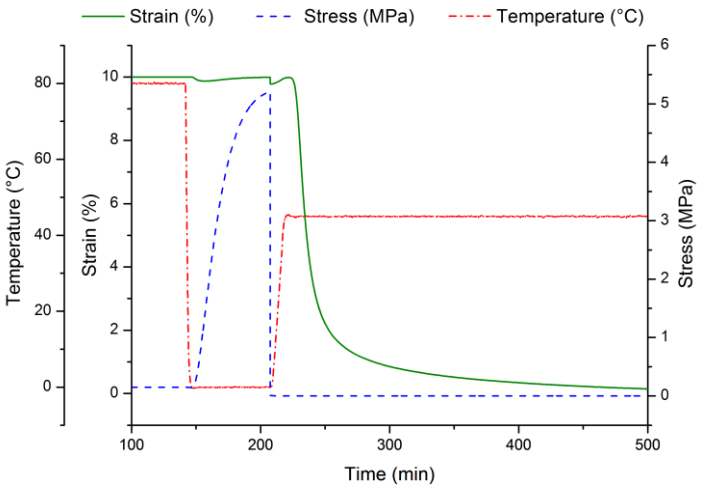

Figure 6-10 Unconstrained recovery step for a film specimen characterised on the DMA Q800 by shape memory cycle with same programming as per Figure 6-9 and recovery temperature of 45 °C. The temperature during recovery step is increased at a rate of 5 °C/min.

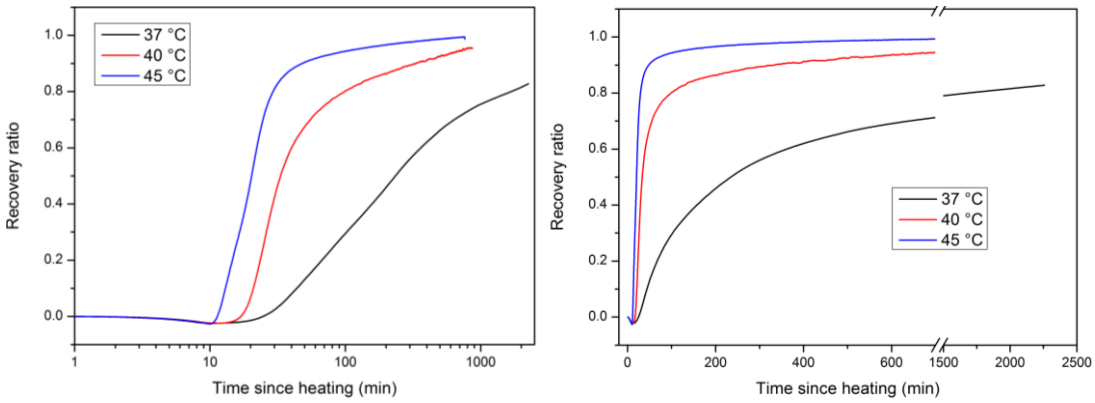

Figure 6-11 Recovery ratio curves for three experiments at different recovery temperatures, against log and linear scale.

6.8 Investigation over the influence of clamped length over material properties obtained from dynamic analysis for film shaped polycarbonate specimens

We noticed that the length of film that is clamped during experiments in tension mode on the DMA has a strong influence on the results obtained. Because of this observation we ran all experiments with the same clamped length and we also decided to test a factory-produced polycarbonate (PC) material. The available sheet of PC had a thickness of 1 mm and we cut out specimens of roughly 3.5 mm width. We first studied the spread in results (focusing on T_g obtained from the peak in the tanδ curve) for cuts in the two perpendicular directions by running temperature sweep dynamic tests with constant clamped length around 8 mm. The cut direction that showed the lowest spread in values of T_g was chosen as the one to continue the experiments. We ran temperature sweeps from 100 °C to 180 °C by ramping at 3 °C/min with an oscillation of 15 μm and an initial preload of 0.01 N. We varied the clamped length between 8, 10 and 12 mm. In Figure 6-12 (a) we report the values of T_g against the clamped length obtained from the temperature corresponding to the peak in tanδ. We notice that the spread in values is very large particularly for the shorter lengths. The range is still quite large for a length of 12 mm and in general the values of T_g are lower than what one could expect for polycarbonate. In figure (b) we report the values of storage modulus in the rubbery region taken at 175 °C; in this case we notice that increasing the length by 2 mm has a drastic effect on reducing the spread in the values. In figure (b) we report the values of storage modulus in the glassy region which we decided to take as the ones at 100 °C since we equilibrated the specimens at this temperature (two points in the 12 mm length area are superimposing). Similarly for what already reported, the data spread much less as the length is increased. The DMA Q800 tension mode clamp is best used in its operating window, this is an area on a plot of modulus vs geometry factor of the film specimen. The dimensions of the tested film specimen give the geometry factor as $GF =$

$clamped\_length/cross\_section$ which determines the horizontal position on the operating window. In Figure 6-13 we report the operating window and the range in which the tested specimens' geometry factor values fall. For simplicity we cut stripes of PC sheet with the same width, since the thickness is also constant the GF was lager for longer clamped length. During the temperature sweep the modulus varied from 10^3 MPa (10^9 Pa) to 0.1-1 MPa (10^5-10^6 Pa) which was covered by the operating window given the range of GF, in particular the glass transition region falls into the window.

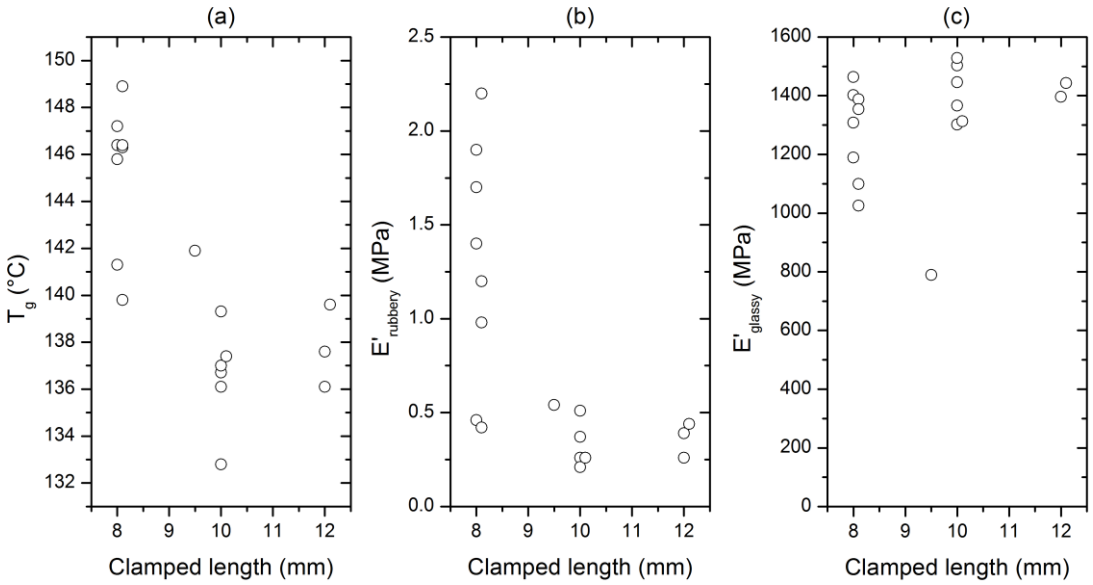

Figure 6-12 Values of (a) glass transition temperature, (b) storage modulus in the rubbery area at 160 °C and (c) storage modulus in the glassy plateau, against the value of clamped length for film specimens of polycarbonate.

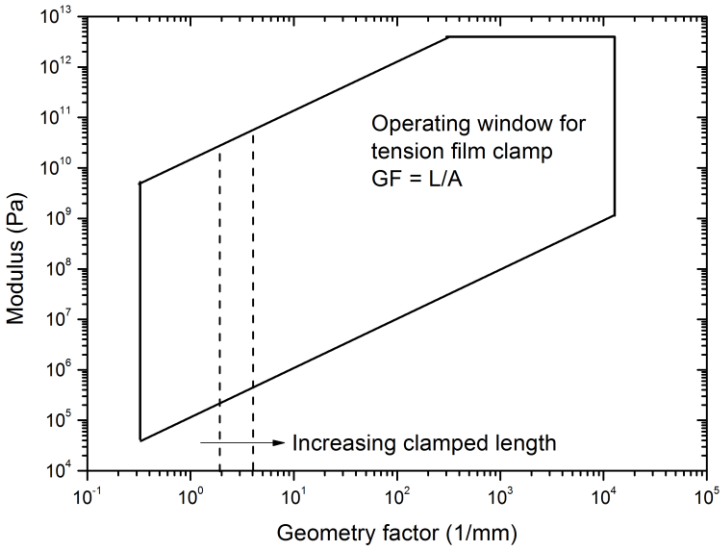

Figure 6-13 Operating window for tension film clamp mode on the DMA Q800. The dashed lines represent the range in which the geometry factors of the tested PC specimens fall into. Since thickness and width of the specimens were mostly constant – given to the fabrication procedure – the higher GF corresponds to longer clamped length. The operating window was reproduced from the Thermal Analysis Q800 manual.

6.9 Discussion and conclusions

6.9.1 Analysis of gel fraction and correlation to material properties

The film specimens are all obtained by the same methodology and with the same designed geometry. For all specimens we calculated the values of gel part from the values of initial mass (after curing) and final mass (after extraction and drying). The values do not significantly spread, each specimen formed a network were 94% ±0.8% of the initial mass of prepolymer reacted during photopolymerisation. From this result alone we would expect good reproducibility for the material properties, though we would be assuming that the formed networks are qualitatively similar. Still as we reported the three properties T_g, $E'_{rubbery}$ and E'_{glassy} are not well reproduced. We considered if there is a correlation between the values of w_{gel} (representing the gel part) and the values for the mechanical properties but did not find any significant one. Furthermore two specimens, 029 and 029b, were obtained as two halves of the same film but lead to very different results. We can assume that even though the relative mass of prepolymer polymerised is basically the same for all specimens, the characteristics of the networks are dissimilar. For example difference in the number of dangling chains (prepolymers that did not form a crosslink), different kinetic chain lengths and number of kinetic chains formed, different number of crosslink per network. All these can affect the mechanical and viscoelastic behaviour of the material leading to the low reproducibility. The cause for such differences could be identified in the printer itself as the measured level of light intensity is not perfectly homogenous with respect to the spatial coordinates on the window and therefore the way the prepolymer is converted during this first curing step and also the amount converted to network might change depending on the position of the specimen. The specimens are then post-cured in a UV-box to complete conversion of prepolymer, which would likely result in the gel part values being very reproducible but the final result would still be largely affected by the first curing step. This is one possible assumption which would require further testing, e.g. characterising the specimens for their gel part without being post-cured as well as characterising the specimens with respect to the position they were printed onto the window.

6.9.2 Dynamic analysis temperature sweep film tension mode: influence of specimen clamped length

The DMA Q800 manual recommends a series of operation windows that are defined by the clamps in use and the expected material properties (the modulus). On the basis of this information the optimal geometry factor of the specimen can be decided, or, if the

geometry factor is given, then it can be checked if the experiment will fall inside the operating window. For all tests we made sure the geometrical factor would be such that we would be in the operating window, though what we noticed is that small changes in specimen length (the length between the clamped sides) gave rise to large changes in properties. In particular we noticed that the glass transition temperature (defined through any of the standard ways) would change by a considerable amount. Because of this observation we ran all temperature sweep tests at the same length of 7.5 mm which, given the average cross-section of the film specimens, results in a geometry factor around 8.5. In turn this puts us in the operating window with values of storage modulus from 1 MPa to tens of GPa, suitable for the material, in particular for the investigation in the glass transition region. As reported, we later decided to run tests on a polycarbonate sheet to determine to what extent the clamped length affects the dynamic analysis results and in general what kind of spread in properties could be expected. To avoid any uncertainty in the applied methodology we ran the standard temperature ramp test without editing any segment other than the starting and final temperature and the heating rate. From the results it seems clear that at clamped length lower than 12 mm, or GF lower than 0.3 mm^{-1}, the experimental data – T_g, $E'_{rubbery}$ and E'_{glassy} – is not accurate. At 12 mm the spread in data is relatively low for the values of the moduli. The values of T_g for 12 mm clamped length are obviously spread on a lower range than what observed for shorter clamped length, though from the point of view of modelling the material the range (4 °) would still produce considerable uncertainty. We can conclude that the clamped length has a very strong impact on the measured properties during the temperature ramp experiment and we can suspect that the results for the PDLLA specimens would be more reproducible if a longer clamped length had been used. As for the reason behind the observed behaviour we could consider: a higher sensitivity of the equipment than what reported on the manual, malfunctioning or poor testing procedure. More testing on different machines might clarify the first possibility. The second possibility is not too unlikely as the machine received damage in the past, which caused the shaft to bend. The shaft was replaced though we do not have data from before the damage that can be compared to what observed for the polycarbonate or the PDLLA. The third possibility cannot be excluded, though the user (the author of this thesis) was trained at TA Instruments and has successfully and extensively used the same machine before the start of this research.

6.9.3 Dynamic analysis: glass transition temperature during cooling ramps

As we noticed, the storage modulus and tanδ curves shift to lower values of temperature during the cooling ramps as opposed to the heating ramps. This is due to the viscoelastic nature of polymers and examples of the same behaviour can be found in literature [104], [194], [196], [200]. Briefly, the shifting is due to the fact that, for most of the experiment, the polymer is out of equilibrium because its response is not only temperature dependent but also time dependent. In the plateau regions we can assume that the polymer is spending enough time at high enough or cold enough temperature to reach an equilibrium or pseudo-equilibrium state. When this state is perturbed by either heating or cooling the material will take a certain time, on top of a certain change in temperature, to produce the same viscoelastic response. It seems logical to at least consider the use of the glass transition temperature values obtained during cooling ramps. First we should notice that these values are distributed on a wide range like the ones observed during heating ramps, therefore nothing would be gained from this point of view. Typically, the tanδ curve during heating stabilises to a certain trace right after the first cycle while the cooling ramp can show a more sporadic behaviour which results in more than one peak to be considered. Maybe more importantly, the tanδ peak during cooling is just too low to be taken as the glass transition temperature. The values fall between 30 and 40 °C. During our experimenting work several specimens were handled in this range of temperature. Their behaviour was that of a glassy, brittle material. Furthermore the specimens left to recover their deformation in an incubator should spring back in a matter of minutes to hours if their glass transition was in fact between 30 and 40 °C. Finally, during application the material would increase in temperature, for all these reasons it seems best to consider the results from the heating ramps.

6.9.4 Expected consequence of data spread over the predictive modelling

We can anticipate the effect of the three parameters lack of reproducibility, on the modelling. The $E'_{rubbery}$ and the E'_{glassy} values are taken as the values of, respectively, the equilibrium modulus and the summation of all moduli in the multi-branch model (generalised Maxwell model). They are therefore connected to most calculations. The $E'_{rubbery}$ will relate particularly to the calculations at long time or high temperature as the model reduces to purely elastic. The E'_{glassy} value has, in particular, one very important clear influence which is the determination of shape fixity, in other terms, it is inversely proportional to the instantaneous strain loss upon unloading. The two values of storage modulus will also have a non-analytically evident effect on the model parameters. For

example the E'_{glassy} will clearly affect the values of elastic moduli in the model. The third parameter is the glass transition temperature values T_g. This could analytically come into place in the Arrhenius-type or WLF equations, though we do not employ any of these equations in a form that includes T_g. We can expect a large effect on the model parameter identification through the temperature sweep fitting. During this fitting we need to determine a certain reference temperature, T_{ref}, from each set of experimental data.

6.9.5 Stress relaxation tests and master curve construction

During stress relaxation testing the traces obtained from different specimens could not be accurately superimposed, for one when trying to build the master curve but also when repeating the experiments at the same temperature. As reported we could eventually obtain a stress relaxation master curve from the tests run for two different specimens (from the same resin), though most of the curves do not superimpose very well. Several experiments could not be used and therefore the procedure was deemed too wasteful both for the amount of resin used and the amount of time required. In this case the problems we encountered might be related to the thermal history removal step. As we noticed during the shape programming and other experiments, the film specimens required very long equilibration times at high temperature to achieve constant length. We can expect this to be true not only for the film geometry but also for the slab-like geometry. Though in the case of the film specimens, given the smaller thickness, we can expect that the internal stresses caused by the thermal history are relieved faster than what could happen for the thicker, slab geometry. In this first part of the research we performed standard tests with 10-15 minutes of thermal equilibration. This is probably not enough to completely erase the thermal history and might affect the trend in stress relaxation curves, as the internal stresses would still get relieved during the tests. With respect to the master curve construction we assumed that manually shifting the curves (on Excel) would be much easier than using a time-temperature superposition software. Since most curves are not superimposing very well and overshoot one each other, the shifting procedure did not seem very suitable to be performed by a software. When shifting the curves we tried to visually minimise the error between each curve. This could be achieved in more than one way and therefore we iterated the process until we obtained an optimal shifting that would produce a plot of shifting factor values against temperature, well-described by Arrhenius-like and Williams-Landel-Ferry equations. As for the choice of the reference temperature, this does not affect the optimal shifting and the master curve can simply be

moved to a different reference temperature by adding or subtracting a constant value from each shifting factor.

6.9.6 Shape memory programming: drop in designed strain and stress increase during cold programming step

As we noticed the initial equilibration step during the shape programming is characterised by an increase in strain. This is due to both thermal expansion and thermal history, the latter basically results in a shape programming. The one hour equilibration step is long enough for the specimen to reach a steady length, we can assume that thermal history is removed and should not create any miscalculation during the rest of the programming. As we already explained, we occasionally noticed an instantaneous drop in strain. As this drop does not correspond to a drop in specimen length or position (the position parameter is directly calculated by the Q800 optical encoder) we can assume that the drop in strain is due to a non-user-programmed measure length segment. We also already specified that just before the loading step we implemented a measure length segment. This is because otherwise the Q800 would apply the designed strain with respect to the specimen length at time equal zero, which would result in every experiment being different. We can also look at the stress required by the machine to provide the strain. At the beginning of the experiment we typically have a small force applied to keep the specimen straight (1 mN). Once the 10% strain is applied the force will grow in a range between 0.08 and 0.25 N, or in terms of stress 0.1-0.29 MPa. This range is comparable to the range of $E'_{rubbery}$ we observed, as (0.1-0.29)/10% = 1-2.9 MPa. The stress is then basically constant for the following hour as one would expect given the high temperature (the viscous components are already completely relaxed, the material response is elastic). During the cooling step the stress and strain behaviours are dictated by the thermal contraction. What we noticed is that the strain drops by a small amount, e.g. 0.1%, which is then recovered in the following hour. At the same time the stress grows by ten-fold with a logarithmic trend. This can be observed in literature and as already stated is due to thermal contraction[138][15][201][202]. The isostrain segment is still valid, therefore the decrease could be justified if the force required was larger than the maximum operational one (18 N). This is theoretically possible as a large stress could be required to accommodate for the strain change due to thermal contraction but, on the other hand, the results clearly showed that the force is well below 18 N. After the drop the strain gradually increases back to 10% with the stress increasing to the 1-10 MPa range. This possibly means that the Q800 is trying to keep the isostrain conditions but finding

resistance so that it is required to increase the force applied. Still, it is not clear why the force would increase on such a long period of time. The specimen is already strained and therefore the machine should just need to compensate for any thermal contraction. From thermal expansion experiments (not reported) we noticed that the decrease of strain for the film specimens is around 1% when going from 80 °C to room temperature, with an average rate of 0.024 %/°C. We could then overestimate a change of -2.0% strain at 0 °C due to thermal contraction, which assuming a modulus of 1000 MPa and a typical cross-section of 0.85 mm^2 would require a force of about 18 N. This is the limit of the Q800 and therefore we could justify why the strain drops by a small amount after the temperature has stabilised at 0 °C. At the same time the machine does not report applying that much force.

6.9.7 Shape memory cycles: shape recovery for film specimens at 37, 40 and 45 °C

The shape fixity was calculated from the ratio of the strain right after unloading and the maximum applied strain. This can be different from calculating the fixity from the drop in strain that follows the unloading because, as we reported, the specimen strain experiences a first drop during the cold phase of the shape programming step. Therefore the calculation might be underestimating the values of shape fixity, though not by much. During the shape recovery step we noticed that the strain increases with the temperature and then starts decreasing once the recovery temperature is reached. This initial increase in strain is most likely due to thermal expansion as also observed in literature [15], [138], [196]. The recovery step proceeded relatively fast for the recovery temperatures of 40 and 45 °C and at much slower pace for the recovery temperature of 37 °C. This is to be expected as the higher the temperature the higher the chain mobility. The results are surely sound when compared one to the other, both from a qualitative and quantitative point of view. At the same time there are a few observations to be made that reveal how the shown recovery behaviour is quite unlikely to be accurate. We should start from a purely empirical observation; as far as we noticed, specimens programmed either by DMA or manually will not show recovery at 37 °C when stored for as long as months, hanging in vertical position with no physical constraints for their shape to be recovered. In other words, the PDLLA SMP is in its fixed state at 37 °C for any experiment that is not carried out inside the DMA. The recovery experiments inside a temperature-controlled oven are reported in the next Chapter and they show that also the behaviour at 45 °C is very different, with the recovery process taking much longer than what observed inside the DMA. From the theoretical point of view we can also notice that any relatively

fast shape recovery should not be observed when the recovery temperature is lower than the glass transition region. In general the shape memory activation is considered to happen at temperature near or above the glass transition temperature, though this is a quite relative concept, as the very definition of T_g depends on the identification methodology and standards in use. From the accumulated literature it seems acceptable to consider, as already stated, that the recovery process will not be displayed for temperatures that are far from the glass transition region observed during temperature sweep analysis. In particular the temperature corresponding to the onset in tanδ might be considered the threshold between fixity and recovery. From this point of view it seems unlikely that the same material exhibiting a glass transition region starting around 40 °C (at the very minimum) would be able to recover at 37 °C. We therefore regarded the DMA results as quantitatively wrong and focused on tests run inside temperature controlled oven.

6.10 Conclusions

The characterisations performed show that the materials properties are not accurately reproducible which therefore will introduce a large error in the viscoelastic modelling. In particular the glass transition temperature values are spread on a large interval of 8 °C when obtained from DMA and 3 °C when obtained from DSC. In trying to understand the cause of such results we first considered if the specimens fabrication would result in low reproducibility of gel part, as this would definitely influence the mechanical properties of the specimens. Still, the methodology we followed results in good reproducibility for the specimens gel part. Even so we looked for a correlation between the gel part values and the material properties and also between each property (T_g, $E'_{rubbery}$, E'_{glassy}). Under the assumption that a larger gel part would result in more crosslinks and less free volume, we would expect a positive correlation with T_g and $E'_{rubbery}$. Still, we did not find any significant correlation. What we can assume is that the networks are qualitatively different so that their viscoelastic response is also different. Starting from this point of view we can assume that even though the fabrication methodology is the same for all specimens the final networks are different one from the other. The step that seems likely to cause this difference is the first curing process which is performed on the Ember 3D printer. The light intensity on the printer window is not perfectly homogenous which can cause differences in the conversion of prepolymer to network in this step. The following step of post-curing inside the UV-box would complete the prepolymer conversion so that the values of gel part for the different specimens are very close one to the other.

To test this hypothesis one should fabricate specimens without post-curing and calculate their gel part values. Also the effect of printing on different positions on the window should be studied. The solution for such a problem would be to reduce the number of specimens printed at the same time to guarantee that all are exposed to the same light intensity.

Furthermore the experiments for polycarbonate sheets show that the clamped length during the temperature sweep can introduce a large error in results and suggest that the reproducibility problems are related to the specimens' length being too short.The analysis of shape memory behaviour was conducted through a custom methodology on the DMA. We could conclude that the programming step is working as planned and that the specimens show high shape fixity. The recovery behaviour was also studied by DMA for three specimens at temperatures of 37, 40 and 45 °C. The results are qualitatively and also quantitatively sound when compared on to the other, with the recovery process taking longer time at lower recovery temperatures. At the same time, these results are not consistent with what we noticed when simply storing strained specimens at the same temperatures. In particular, we empirically observed that the fixed shape can be retained by storing at 37 °C. Because of these observations we focused on running recovery experiments in a temperature-controlled oven, which is the focus of the next chapter.

Chapter 7– Empirical analysis of the shape recovery behaviour in isothermal conditions

7.1 Introduction

This Chapter presents the empirical observations over the shape recovery of UV-cured PDLLA networks programmed through the same shape programming cycle and let to recover under different isothermal conditions for up to two weeks.

The main motivation behind this experimental analysis was to prove that a shape recovery lasting few weeks could be obtained, independently from the recovery temperature being equal to physiological temperature or any specific temperature. Consequentially, we would also investigate several research questions that are here summarised:

1. Obtain empirical proof of weeks' long shape recovery
2. Identify the temperature at which the temporary shape is fixed
3. Evaluate shape memory behaviour at 37 °C and 20 °C over long periods of time

The methodology we followed is a typical shape memory cycle consisting of a programming step and a free recovery step. When designing the experiments we worked while considering the following main assumptions as true:

1. The shape recovery can be activated in a range of temperature that is bounded from below by a certain temperature that fixes indefinitely the programmed deformation
2. Choosing recovery temperature closer and closer to this lower bound will enable to obtain extremely slow recovery kinetics
3. The influence of programming step above the shape recovery is limited; the chosen programming step is one that results in the same qualitative effect of maximising the recovery time for any recovery temperature

The first assumption is intrinsic to the very nature of a shape memory polymer. Here we decide to explicitly report it since one of our objectives was to identify the lower boundary temperature. In our research we consider the change in shape recovery with temperature as a continuous process, this translates into our second assumption. The third assumption comes from both what we observe in literature and our own theoretical modelling. During shape programming the polymeric networks receive a certain fixed strain, resulting in a stress relaxation process that will go on at the programming temperature for the entirety of the programming time. This process will result in a certain configuration of internal stress which will determine the shape recovery. At the same time stress relaxation processes move towards a plateau condition, which means that the effect of programming

over shape recovery is limited. Our understanding is that allowing for the stress relaxation processes to complete will provide the condition for the slowest possible recovery. In order to achieve this, the programming step consists of 60 minutes heating at 80 °C. The specimens' free recovery was then followed at temperatures of 45, 48, 50 and 53 °C, typically as long as it would take for a plateau to be reached. We also performed a six months investigation of the recovery at physiological temperature (37 °C) and at 20 °C. Finally, we should add that all specimens employed were prepared following the same methodology.

7.2 Empirical observation of shape recovery at 45, 48, 50 and 53 °C

We start by reporting the results in terms of average values of recovery ratio (R_r) against recovery time. The data points are plotted in Figure 7-1 for the recovery temperatures of 45, 48, 50 and 53 °C. The tests were named OFO as in oven, freezer, oven, and followed by the value of recovery temperature. We can generally notice that the lower the recovery temperature, the slower the observed recovery behaviour. We define the values of recovery time required to achieve 70% recovery ratio as $t_{0.7}$ and report them in Table 7-1. We can notice that the values of $t_{0.7}$ increase by around tenfold for each descending value of recovery temperature. At the highest recovery temperature of 53 °C, the value of $t_{0.7}$ is lower than 15 minutes and a crossing point could not be experimentally observed, at 50 °C the value increases to around 60 minutes. At 48°C, $t_{0.7}$ is approximately 900 minutes (i.e. 15 hours), while at 45 °C it increases to 10000 minutes (one week). This last result is encouraging for slow recovery applications, as it gives empirical proof of one week long shape recovery. At the same time it should be noticed that the specimens stored at 45 °C recovered in hours to values of R_r higher than 10% and reached 30% recovery in around one day. Additionally, the specimens recovering at 45 °C showed two main different kinetics. In Figure 7-2 we report the data points for the three experiments at 45 °C. We can notice that one specimen (s3) achieves 95% recovery during the observation time of 15 days, while the remaining two (s1, s2) reach around 60% and 70% recovery. The recovery is also slower for these specimens, they share almost the same behaviour with the exception of the initial recovery points. Additionally, for all three specimens, we can notice that the recovery behaviour came to a halt at least twice during our observation. In the plot these plateau points are denoted by the dashed lines; in Table 7-2 we report the values of R_r at which the recovery momentarily stops and the interval of time during which we could observe no significant change in the value. We notice that the values of R_r at these plateaus are quite close for all three specimens, though specimen

3 incurs in the plateaus at lower recovery times. The observed durations for the plateaus of different specimens are also comparable. Specimen 3 reached (almost) full recovery and therefore we also report a 96% plateau. At the end of the experiments we heated up all specimens to 80 °C, this resulted in the residual deformation being recovered. Additionally, we noticed that some specimens would recover through a bent shape. This would happen mostly during slow recovery at 45 °C, Figure 7-3 shows one such specimen. From our observations the 45 °C recovery temperature defines a drastic change in recovery behaviour. Around this temperature different specimens can show quite different behaviour when recovering at the same time (same experiment), as we reported. Few degrees below this temperature the behaviour for different specimens is also more sporadic and some specimens do not show recovery.

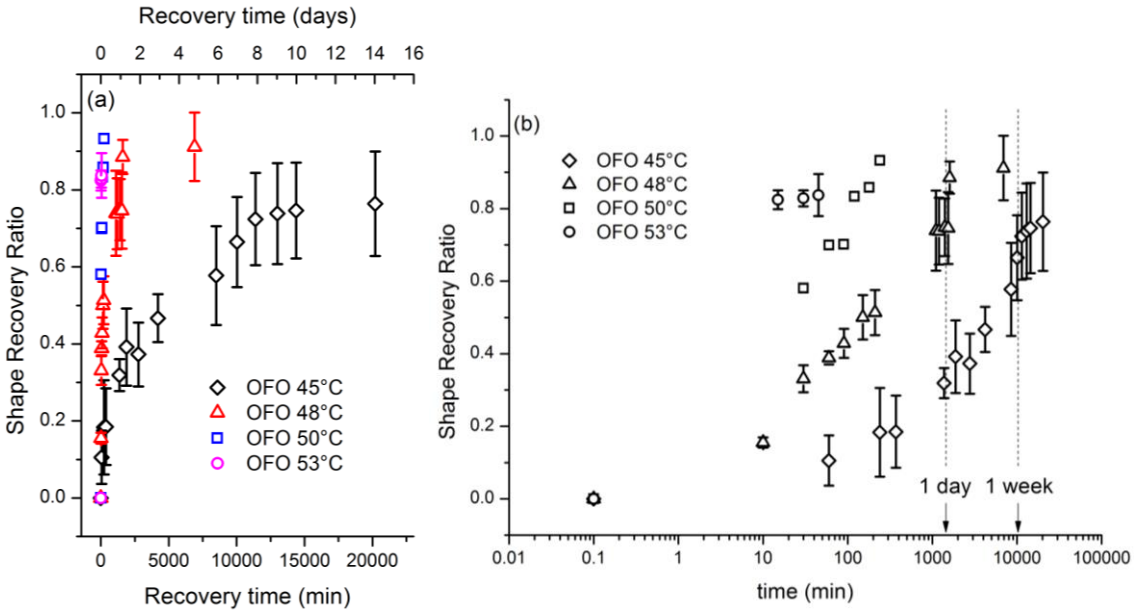

Figure 7-1 (a) Experimental values of shape recovery ratio against time at isothermal temperatures of 45, 48, 50 and 53 °C. Symbols represent the average for measurements obtained from three specimens, bars represent one standard deviation. The data for recovery at 50 °C was obtained from one specimen. (b) Semi-log plot of the same data points

	Recovery time required to reach 70% recovery at T_r			
T_r (°C)	45	48	50	53
$t_{0.7}$ (min)	10832	945	60	< 15

Table 7-1 Values of recovery time to reach 70% recovery ratio at different recovery temperature. Values are calculated through two points interpolation.

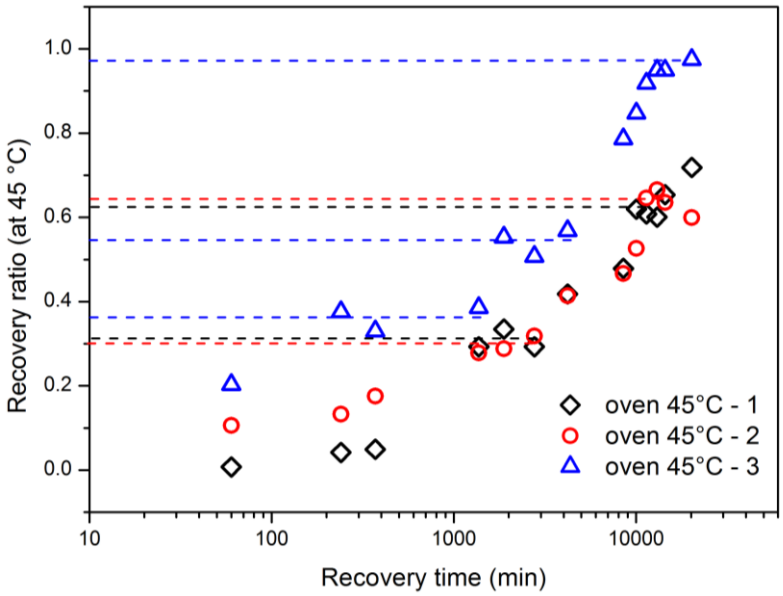

Figure 7-2 The data points of recovery ratio against recovery time for three experiments at 45 °C. The dashed lines indicate the observed plateaus in recovery ratio.

Experiment	**R_r plateau values**	**Duration (h)**
OFO 45°C – 1	0.30; 0.61	23; 49
OFO 45°C – 2	0.30; 0.64	23; 50
OFO 45°C – 3	0.36; 0.54; 0.96	19; 39; n.a.

Table 7-2 Specimens recovering at 45 °C showed two plateaus points at which R_r value is constant. The table reports the values of R_r and the observed duration of the plateaus.

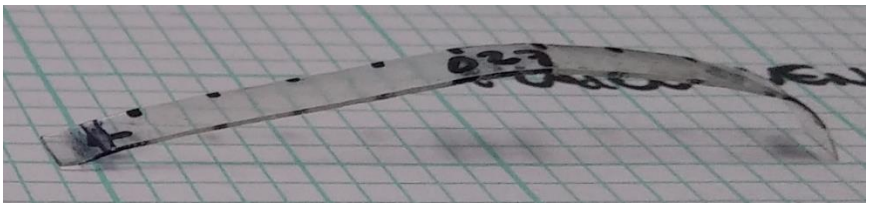

Figure 7-3 PDLLA UV crosslinked network specimen. While recovering at 45 °C the specimen bends and goes back to a straight shape if heated up to 80 °C.

7.3 Absence of shape recovery at 37 and 20 °C

Specimens programmed through the same programming step were stored at 37 and 20 °C for several months. In Table 7-3 we report the strain values at the beginning (May 2018) and at the end of the test (October 2018). Heating the specimens to 80-100 °C resulted in a strain change comparable to the imparted value.

Temperature	**Initial strain**	**Final strain**	**Experiment time**
20 °C	12.1%	13.0%	~6 months
20 °C	12.0%	12.0%	~6 months
20 °C	11.5%	12.3%	~6 months
37 °C	11.8%	12.9%	~7 months
37 °C	11.9%	11.5%	~7 months
37 °C	10.0%	9.40%	~7 months

Table 7-3 Values of strain at the beginning and end of tests for specimens recovering at 20 and 37 °C

7.4 Discussion

7.4.1 Potential for slow rate, long recovery

The two weeks recovery observed at 45 °C is encouraging in view of applications requiring long recovery time. At the same time, we report that the specimens can recover up to 20% in less than two hours. This is already a significant change in strain over a relatively short time that could exclude the use of the material in certain applications. To work around this problem, one could exploit the slower recovery behaviour observed at higher values of R_r. For example, the average recovery at 45 °C will go from R_r = 57% to R_r = 72% in 48 hours following a quite linear progression. If one was interested in a, slow rate, 20% change in shape, then the application might be conducted in this time interval. There are other time points we could take into consideration, with even longer duration, but the general idea is that bypassing the initial "fast" recovery might be a solution to enable applications requiring very slow recovery rate. For the PDLLA networks, these applications cannot be carried out at physiological temperature. As observed the strain is retained when the specimen is stored at 37 °C and the recovery can only be activated by heating. The glass transition temperature would need to be reduced so that the recovery could be activated at this temperature, or possibly the polymer chemistry could be changed in order to obtain a larger glass transition region that incorporates relaxation kinetics activated at 37 °C.

7.4.2 Plateaus during recovery at 45 °C and network heterogeneity

As we observed, the 45 °C recovery experiments proceed through two plateaus of recovery ratio. We can liken this behaviour to a series of distinguishable recoveries adding up to the overall one, with every next recovery starting from the plateau value of the previous one in a step-like way. Any shape recovery processes in T_g activated SMPs is a combination of several recoveries, resulting from a distribution of chain relaxation kinetics, each with different characteristic relaxation times. Here we can simplify and imagine our network as made of three coexisting regions: each region can relax at the recovery temperature but their structures (e.g. number of crosslinks) are different to the point that their associated relaxation times are magnitudes apart. This way while the first relaxation process is completed, the second does not start, leading to a dead time in recovery. This behaviour is similar to a multi-shape memory effect, though instead of a change in temperature, the different recoveries are activated by a change in time. Also the behaviour can be noticed only at low recovery temperature as at higher temperatures the gaps in relaxation times become too small to result in an experimentally noticeable

dead time. The assumption of network heterogeneity is probably accurate and should be ascribed to the fabrication technique. In particular, the UV-curing carried out on the Ember is quite likely to introduce a gradient in macromer conversion. This is because, as the projected light travels through the resin, it will drop exponentially in intensity with a Beer-Lambert equation form:

$$I(z) = I_0 \exp(-z/D_p)$$

Where I_0 is the maximum intensity as the light enters the resin, z is the depth travelled by the light in the resin and D_p is the penetration depth (100 μm ca.). Therefore, the energy dose received at a certain depth will increase linearly with exposure time but decrease exponentially with z. This means that the level of overexposure time required to guarantee the same conversion at each z of a specimen is not practical and would generate excessive lateral overcuring. We assumed that the post-curing would uniform the network structure but this might not be the case. The gradient in conversion along the specimen depth would also explain why some specimens recover with a bent shape, as there would be a difference of recovery speed at the two faces of the specimen because of different crosslinking degree. Additionally to the gradient along the specimen depth, the light intensity across the printer window is not perfectly uniform, which would also result in conversion gradients.

7.5 Conclusion

We studied the shape recovery behaviour of film-like specimens of PDLLA at the temperatures of 45, 48, 50 and 53 °C. We found that the shape recovery is possible for all temperatures. At the lowest temperature of 45 °C, we observed considerable differences in recovery speed for different specimens with the slowest kinetic achieving 70% recovery ratio in two weeks. At temperatures few degrees lower than 45 °C most specimens are not showing any recovery while others can still recover part of the deformation, at 37 °C and 20 °C there is no recovery after 6 months. At the temperature of 45 °C the recovery behaviour develops through a series of distinguishable recovery steps similar to what would be obtained by programming of multiple temporary shapes.

Chapter 8 – Linear viscoelasticity modelling, shape recovery simulation and comparison to experimental data

8.1 Introduction

In this Chapter we present the mathematical framework developed to model the material and predict its shape recovery behaviour. We then compare the modelling results with the experimental results from shape recovery tests at 45, 48, 50 and 53 °C.

The material modelling was the main objective in this part of the research and clearly one of the most important objectives in the overall research. In addition, we moved through the modelling with the following objectives in mind:

1. Compare different methodologies to identify the parameters required for the modelling and choose the most efficient one;
2. Study the influence of experimental data variance on the prediction results and how to account for it;
3. Apply the prediction model to some realistic scenarios of temperature fluctuation during application;
4. Apply the model to theoretically show that the programming conditions have limited effect over the shape recovery behaviour;

The motivation behind pursuing most of these objectives is related to the application over long time period where, for example, temperature fluctuations can be expected. We also had to take into account the experimental thermo-mechanical results for our material showing a low reproducibility and hence aim at somehow compensating for this. We also decided to use the model to show that the programming conditions do not have unlimited influence on the shape recovery, since this is one of the assumptions we keep through the research.

We modelled the material by the generalised Maxwell model (GMM), with the dependency of the material response upon temperature being introduced through the time-temperature superposition principle (TTSP) for which we use the Arrhenius-type and the Williams-Landel-Ferry (WLF) equations [11], [144]–[147]. This kind of phenomenological modelling is well explored in literature, with the main differences between works being in the number of material phases considered, in the modelling of thermal expansion, in the use of partial derivatives[8], [12], [133], [136]–[139], [196], [203]–[206]. In general the validity of this theoretical framework rests on the assumption of linear viscoelasticity and thermorheological simplicity of the material being modelled:

the first comes into place in the material constitutive models, such as the Maxwell spring-dashpots elements and the second is required for the TTSP to be valid.

The parameters required for the modelling were obtained from fitting of experimental data by following two methodologies that differ in the way the experimental data is collected. The master curve method (MC) requires to run a time-temperature superposition test and build the stress relaxation master curve for the material. The methodology we followed is described in the Supplementary material section of [8] and frequently applied by Yu, Qi et al., similar methodologies can be found in literature such as in [136], [207] The temperature sweep (TS) method requires to run at least one temperature sweep test on the DMA and to simultaneously fit two viscoelastic properties, e.g. storage modulus and tanδ, at the same time, while also applying the time-temperature superposition principle. This methodology can be also found in literature in very similar forms, e.g. in fractional derivatives models[137], [195], [197], or also for integer derivatives in[143], [203]. Both methods will be further discussed in their specific paragraphs. Still, most of the presented work was carried out through the TS method as it was much faster to obtain different sets of model parameters from different specimens' temperature sweep results.

8.1.1 The generalised Maxwell model and the TTSP: forms used for Arrhenius-type equation and Williams-Landel-Ferry equation

As a reminder, we here introduce the nomenclature used for the GMM and for the TTSP. The model is depicted in Figure 8-1. It consists of one equilibrium branch and several non-equilibrium spring-dashpot branches (Maxwell elements) in parallel. The equilibrium branch is purely elastic and represents the material response when rubbery, E_{eq} can be obtained as the value of the rubbery storage modulus plateau from DMA experiments. Each non-equilibrium branch is a Maxwell element with a certain value of elastic modulus E_i and a certain relaxation time τ_i. These elements describe the different relaxation modes for the material. Branches with higher τ_i will better describe the mechanical behaviour at longer experimental time and vice versa. To fully describe the material several branches with increasing relaxation times can be added, a typical approach is to choose the values of relaxation times as log-spaced. We should also specify that the values of relaxation time that are chosen by the user are the reference values, i.e. the values at a certain reference temperature. Relaxation times at other temperatures are obtained through the TTSP as later discussed. For the elastic moduli the only constrain to be introduced is that the summation $E_{eq} + \sum E_i$ should be equal to the

material modulus for an instantaneous response, which can be obtained as the value of the storage modulus in the glassy plateau. As far as we noticed there is no particular trend in how to choose the values of E_i and a minimisation algorithm could even output some zero values if free from non-zero constraints. The TTSP will be implemented by the Arrhenius-type [11], [145]–[147] and WLF [144] equations in the form:

$$\ln(\alpha_T) = -\frac{AF_C}{k_B}\left(\frac{1}{T} - \frac{1}{T_{ref}}\right) \qquad \text{Arrhenius-type} \qquad (8.1)$$

$$\log(\alpha_T) = -\frac{C_1(T - T_{ref})}{C_2 + (T - T_{ref})} \qquad \text{Williams-Landel-Ferry} \qquad (8.2)$$

Where α_T is the shifting factor at a certain temperature T, T_{ref} is the reference temperature and will be discussed in more detail at the end of the paragraph, AF_C/k_B is a constant parameter (the relevant bit being F_c, the configurational free energy), C_1 and C_2 are material constants. In the application of TTS we can think of four relevant temperatures that are going to influence the data fitting: the reference temperature for the shifting during MC construction; the reference temperature in the Arrhenius-type equation, let us say T_{Arr}, which is sometimes taken equal to T_g; the reference temperature in the WLF equation, which is often referred to as T_M; the temperature at which to switch between the use of the two equations, sometimes called switching temperature and termed T_S. In our modelling we just consider one reference temperature (T_{ref}) for the two equations and also consider this as the switching temperature. Similar examples can be found in literature [137], [195], [203], [204], particularly in fractional models but also in Yu et al. [8] (though the paper states differently). The TS methodology does not provide any experimental information of shifting factor values against temperature, as opposed to the MC methodology. Each previously discussed relevant temperature value would therefore be an additional unknown variable to be obtained during fitting. Furthermore, the next paragraph will show that this approach is successfully used when fitting the experimental data from the stress relaxation master curve. As previously discussed the relaxation times at a generic temperature are calculated from the reference values and from the TTSP. This is obtained through the equation:

$$\tau_i(T) = \alpha_T(T)\tau_i^{ref} \qquad (8.3)$$

Where τ_i is the relaxation time in the *i-th* branch at a certain temperature T and τ_i^{ref} is the reference relaxation time in the same branch. The values of the reference relaxation times are valid for $T = T_{ref}$ and are usually assigned arbitrarily in a log-spaced manner, as previously stated.

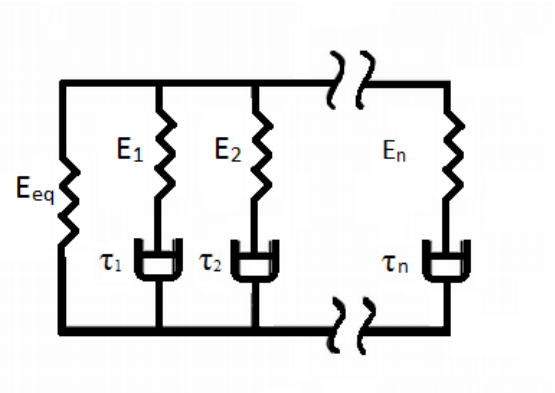

Figure 8-1 Generalised Maxwell model with n parallel Maxwell elements and one equilibrium branch

8.2 MC method: Model parameters determination by master curve construction

In the following paragraphs we report the results from the stress relaxation isotherms shifting, which provides the relaxation modulus master curve and the plot of shifting factors against temperature employed to identify the model parameters when this kind of methodology is used.

8.2.1 Determination of parameters for time-temperature superposition

In the MC method the parameters for the TTSP are determined by building the stress relaxation master curve. For this purpose we did not use any minimisation algorithm as we found more time-efficient to shift the curves manually until an acceptable superposition was obtained. During this process the values of the shifting factors at each temperature with respect to the reference curve are collected and plotted against the temperature. Fitting the data of $\alpha_T(T)$ to the Arrhenius-type and WLF equations allows to determine the parameters AF_C/k_B, C_1 and C_2. In Figure 8-2 we report the master curve built from the stress relaxation tests for the PDLLA networks. Fifteen stress relaxation curves, from -15 to 50 °C at 5 ° intervals, are manually shifted with respect to the one at the chosen reference temperature of 15 °C. The values of shifting factor α_T for each temperature are plotted in Figure 8-3. Below the reference temperature (T_{ref}) the values are fitted through the Arrhenius-type equation. Plotting the values of $ln(\alpha_T)$ against the values of $(1/T - 1/T_{ref})$ in K^{-1} allows to determine the slope $-AF_C/k_B$ which in this case is equal to 21376 K. For temperatures above T_{ref} the WLF equation was used to fit the data. C_1 and C_2 are determined by minimising the error between experimental data and calculated values of α_T, which results in C_1 = 34.1 and C_2 = 68.6 °C.

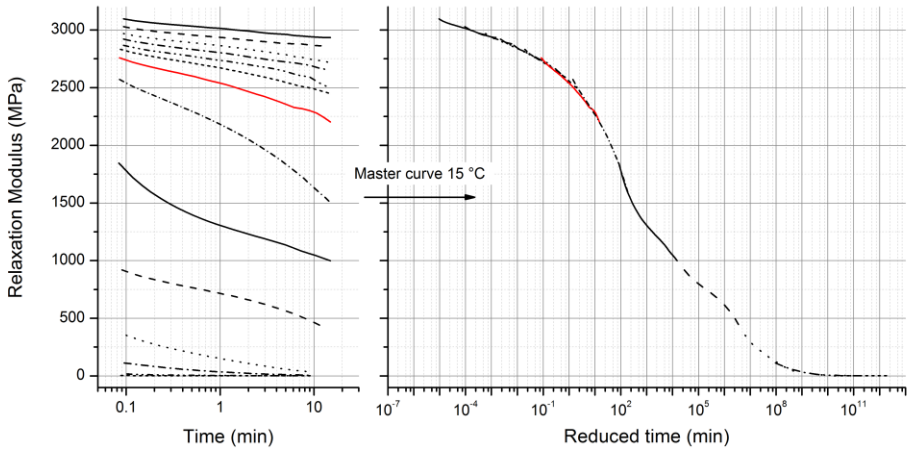

Figure 8-2 Stress relaxation master curve at 15 °C and the stress relaxation tests at temperature from -15 °C to 50 °C increasing at 5 °C intervals.

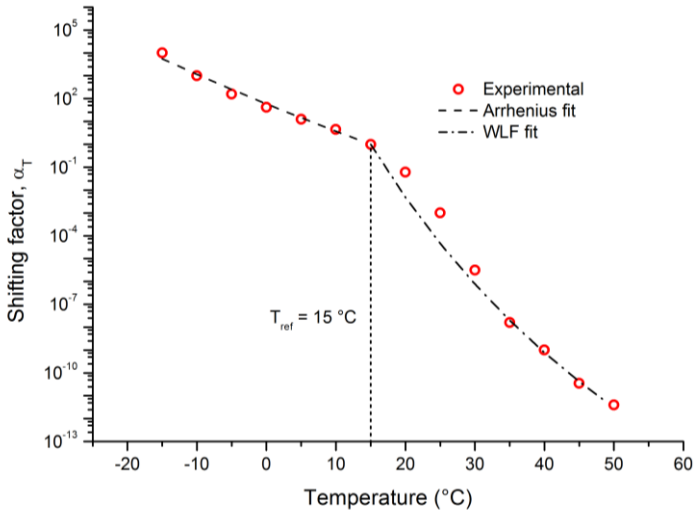

Figure 8-3 Shifting factors experimental values against temperature and WLF and Arrhenius behaviour

8.2.2 Improving the fitting by choosing a more accurate value of shifting temperature

It can be noticed from Figure 8-3 that the fitting can be improved. This can be done by reducing the data points that the WLF equation should fit to the ones from 20 to 50 °C and temporarily lifting the simplification $T_M = T_{ref}$. This allows us to determine a more accurate value of switching temperature, as shown in Figure 8-4, of around 19 °C. Still wanting to apply the simplification of using one T_{ref}, we shifted the master curve from Figure 8-2 so that the new reference temperature would be 19 °C. This is done by calculating the value of α_T at 19 °C, which is 0.362, the logarithm value is then -0.44. Shifting the master curve by this value will result in a new one that is valid for the, non-experimental, reference temperature of 19 °C and that can be fitted to the GMM to obtain the values of elastic moduli and new reference relaxation times.

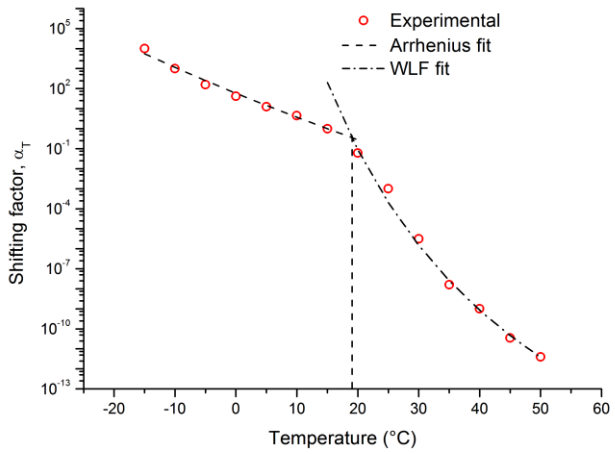

Figure 8-4 The fitting of the shifting factors data is improved by choosing a switching temperature around 19 °C

8.2.3 Determination of parameters for the generalised Maxwell model

To fit the master curve we first define the value of E_{eq}, the elastic modulus for the equilibrium branch, as the smallest experimental value of relaxation modulus. The summation of the elastic moduli can generally be taken as the experimental value of the glassy plateau, though as far as we noticed the same fit is obtained without introducing this equality constraint. The number of branches in the model was changed until obtaining a good fit, starting from a relaxation time of 0.001 minutes for the first branch and increasing ten-fold for each new branch. The master curve is fitted on MATLAB (the script is reported in Appendix A) by minimising:

$$error = \sum_i \left(\frac{E_{relax}^{calc}(i)}{E_{relax}(t(i))} - 1 \right)^2 \tag{8.4}$$

$$E_{relax}^{calc}(i) = E_{eq} + \sum_{j=1}^{N} E_j \cdot \exp\left(-\frac{t(i)}{\tau_j}\right) \tag{8.5}$$

Where $E_{relax}^{calc}(i)$ is the *i-th* value of relaxation modulus calculated by Prony series, while $E_{relax}(t(i))$ is the experimental value of relaxation modulus at the *i-th* time data point; N is the total number of branches. The total error is the output of a function script which takes as input the values of elastic moduli and relaxation times. The function is handled to an fmincon solver with equality conditions such that the summation of all elastic moduli is set to the largest experimental value of E_{relax} and boundaries conditions such that all variables are non-negative. The values of relaxation time are part of the variables but are set to constant values as already explained, therefore the only parameters that are optimised are the elastic moduli. In Figure 8-5 we report the fitting obtained for a total number of non-equilibrium branches equal to 20 and relaxation times log-spaced from

1E-3 to 1E+16 min. The model parameters determined from the fitting are reported in Table 8-1 together with the time-temperature superposition parameters, it should be reminded that all obtained values are valid for a reference temperature of 15 °C, the relaxation times at different temperatures can be obtained through Eq.8.3. The obtained set of parameters was used to simulate a temperature sweep dynamic analysis going from -20 to 80 °C with oscillation of 1 Hz. The results are reported in Figure 8-6, in terms of the storage modulus and tanδ traces. Though the curves are not smooth, particularly the tanδ one, we can observe peak in tanδ at 52 °C with a temperature range from onset to offset of the curve of about 40 °C. The drop in storage modulus is predicted to happen in a 25 ° range, the onset being around 15 °C and the offset around 40 °C.

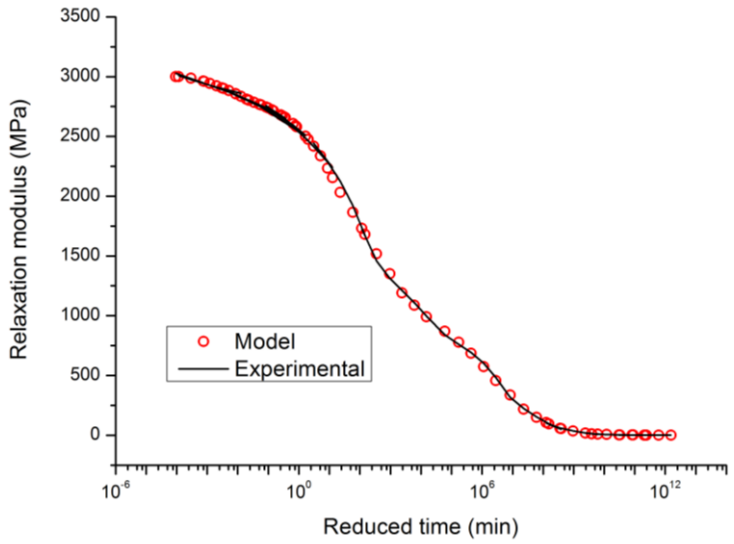

Figure 8-5 The relaxation modulus master curve is fitted by a GMM model with 20 non-equilibrium branches

Parameters	**Values**	**Parameters**	**Values**
C_1	34.1	C_2	68.6 °C
AF_c/k_b	-21376 K	T_{ref}	15 °C
Parameters	**Values**		
E_{eq}	1.18 MPa		
$E_1 - E_{20}$ (MPa)	70.1; 125; 85.2; 184; 456; 448; 433; 244; 167; 280; 293; 151; 55.4; 12.3; 1.43; 0.344; 9.1E-4; 7.3E-4; 7.2E-4; 7.2E-4		
$\tau_1 - \tau_{20}$ (min)	1E-3; 1E-2; 1E-1; 1E+0; 1E+1; 1E+2; 1E+3; 1E+4; 1E+5; 1E+6; 1E+7; 1E+8; 1E+9; 1E+10; 1E+11; 1E+12; 1E+13; 1E+14; 1E+15; 1E+16		

Table 8-1 Parameters for the generalised Maxwell model with 20 non-equilibrium branches

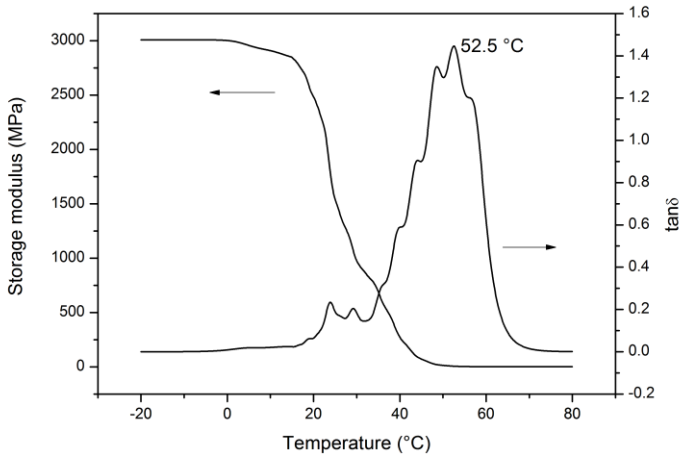

Figure 8-6 The model obtained through the master curve fitting and the application of the TTSP is used to simulate the response of the material to a dynamic analysis temperature sweep test from -20 °C to 80 °C, at 1 Hz.

8.3 TS method: Model parameters determination by temperature sweep fitting

The model parameters can also be determined by fitting the experimental data from a temperature sweep test (TS method). This is the methodology that we adopted throughout the shape recovery modelling. It has the advantage of relying on a quick DMA test so that multiple fittings from multiple specimens can be produced in a short time. In this method two properties are fitted at the same time, namely the storage modulus and the tanδ curves. The model is the same generalised Maxwell model and the time-temperature superposition is implemented by the same two equations. Though, the experimental information on shifting factors for a certain T_{ref} is lost. Therefore the optimisation algorithm needs to simultaneously target the values of T_{ref}, C_1, C_2 and AF_c/k_b other than the values of elastic moduli in the non-equilibrium branches. The full MATLAB code can be found in Appendix A. In this case we used the lsqnonlin solver and the target for the optimisation is the matrix:

$$\boldsymbol{error} = [\boldsymbol{E_{stor}^{error}} \quad \boldsymbol{tan\delta^{error}}] \tag{8.6}$$

Where $\boldsymbol{E_{stor}^{error}}$ is a column vector with element $E_{stor}^{error}(i)$ equal to the difference between calculated and real value of storage modulus at the *i-th* temperature value $T(i)$ and $\boldsymbol{tan\delta^{error}}$ is a column vector with element $tan\delta^{error}(i)$ being the difference between calculated and real value of tanδ at the same temperature value. The calculated values at a certain temperature are obtained from the equations:

$$E_{stor}^{calc}(i) = E_{eq} + \sum_{j=1}^{NT} E_j \cdot \frac{\omega^2 \tau_j^2(i)}{1 + \omega^2 \tau_j^2(i)} \quad (8.7)$$

$$E_{loss}^{calc}(i) = \sum_{j=1}^{NT} E_j \cdot \frac{\omega \tau_j(i)}{1 + \omega^2 \tau_j^2(i)} \quad (8.8)$$

$$tan\delta^{calc}(i) = \frac{E_{loss}^{calc}(i)}{E_{stor}^{calc}(i)} \quad (8.9)$$

$$\tau_j(i) = \alpha_T(i) \cdot \tau_j^{ref} \quad (8.10)$$

Where E_{loss}^{calc} is the calculated value of loss modulus, ω is the experiment frequency (1 Hz), *NT* is the total number of non-equilibrium branches, E_j is the elastic modulus in the *j-th* non-equilibrium branch, τ_j is the relaxation time in the *j-th* non-equilibrium branch at the *i-th* temperature value, $\alpha_T(i)$ is the shifting factor value calculated at the *i-th* temperature value, τ_j^{ref} is the value of relaxation time in the *j-th* non-equilibrium branch at the reference temperature. The values of shifting factors are calculated accordingly to the Arrhenius-type equation when the temperature is lower than T_{ref} and accordingly to the WLF equation when at or above T_{ref}. In Figure 8-7 (i) to (viii) we report the eight fittings obtained when modelling the response through a generalised Maxwell model with 14 non-equilibrium branches. In Figure 8-8 we report the distribution of the model parameters T_{ref}, C_1, C_2 and AF_c/k_b. The values of reference relaxation time are once again set in a log-spaced way, from 1E-4 to 1E+9 seconds. The elastic moduli values can be found in Appendix B. The four parameters responsible for the time-temperature superposition are distributed on large ranges, all of the interquartiles, except for AF_c/k_b, are almost as large as the full range. The average ± standard deviation for all parameters are: T_{ref} = 40.7 ± 1.89 °C; C_1 = 12.3 ± 0.76; C_2 = 11.3 ± 2.88 °C; AF_c/k_b = -34161 ± 3529 K. The values for this last parameters are fall in a small interquartile, though the minimal and maximal values fall far from the median.

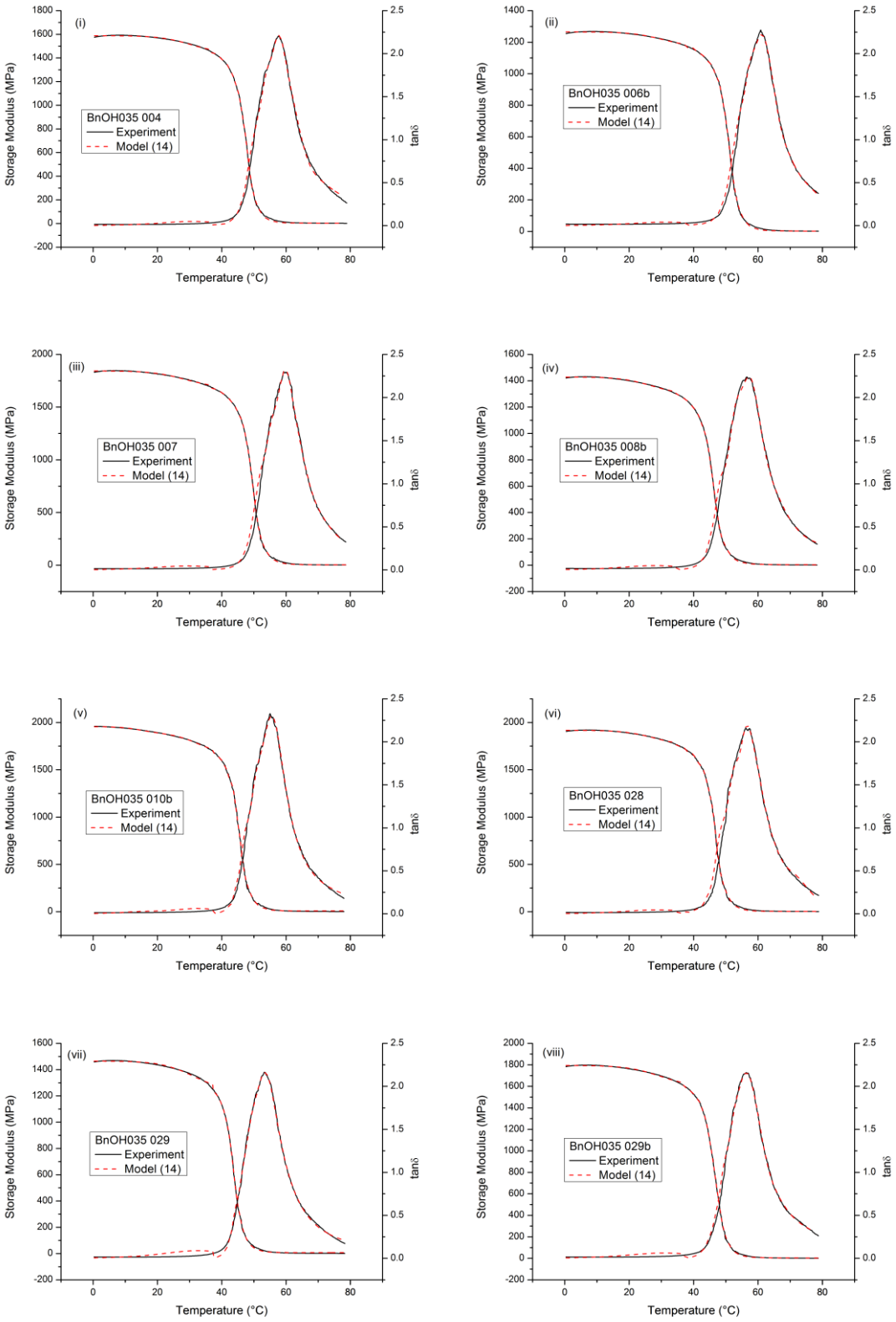

Figure 8-7 (i-viii) Results from fitting eight DMA temperature sweep data to a 14 non-equilibrium branches generalised Maxwell model implemented with TTSP.

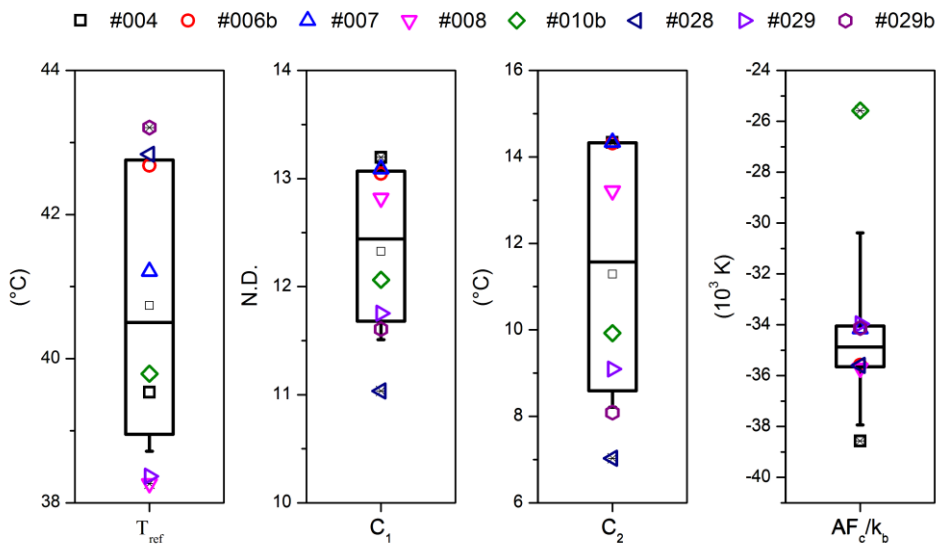

Figure 8-8 Values distribution of parameters for TTS. Each set of four parameters is obtained from fitting the temperature sweep experimental data of one specimen. For each plot the box range is 25th to 75th percentile, horizontal line is the median, thin-lined □ symbol marks the mean, × symbols mark the full range, whiskers mark mean ± standard deviation. The scatter points represent each one specimen, labelling is the same across all four plots.

8.4 1D-Modelling for the shape memory behaviour prediction

To be able to predict the shape recovery behaviour of the specimens we first model the strain and stress evolution for each branch during programming and until the unloading step. This provides us with the starting point to solve the system of differential equations that govern the strain evolution during the unconstrained recovery. Keeping in mind that the programming cycle consists of isostrain processes, either isothermal holds or constant rate temperature sweeps, we can approach the steps in the following manner.

We calculate the elastic strain in each non-equilibrium branch at the end of loading and holding step as:

$$\varepsilon_j^s(t_h) = \varepsilon_{max} \cdot exp(-t_h/\tau_j) \tag{8.11}$$

Where ε_{max} is the total stress applied to the sample, i.e. the stress in the equilibrium branch of the model, t_h is the holding time at the programming temperature T_h and τ_j is the relaxation time in the *j-th* non-equilibrium branch at the temperature T_h which is calculated as per Eq.8.3. With the obtained values of elastic strain we can solve the evolution during the cooling step. This is divided in a first part corresponding to a fast cooling ramp of -20°/min and a second part corresponding to the isothermal at the cold temperature T_c for the time t_c. During the cooling ramp the strain evolution in each non-equilibrium branch is calculated by:

$$\varepsilon_j^s(t) = \varepsilon_j^s(t_h) \cdot exp \int_{t_h}^{t} \frac{-dt}{\tau_j(T(t))} \tag{8.12}$$

The integral will make use of the WLF equation until the reference temperature is reached and of the Arrhenius equation afterwards. The final values of strain can then be used to calculate the strain at the end of the isothermal cold step:

$$\varepsilon_j^s(t_c) = \varepsilon_j^s\left(t_{ramp}\right) \cdot exp(-t_c/\tau_j) \tag{8.13}$$

With the relaxation time being constant as the temperature does not change and $\varepsilon_j^s\left(t_{ramp}\right)$ being the value of strain at the end of the cooling ramp for each non-equilibrium branch. This step concludes the calculations related to the programming cycle. The last contribution to be considered is due to the instantaneous strain recovery when unloading at the cold temperature T_c. Since the stress is zero and since the process is too fast and the temperature is too low for the dashpots elements to respond, we can calculate the strain change $\Delta\varepsilon$ as a purely elastic response:

$$\Delta\varepsilon = \frac{E_{eq}\varepsilon_{max} + \sum_{j=1}^{NT} E_j\varepsilon_j^s}{E_{eq} + \sum_{j=1}^{NT} E_j} \tag{8.14}$$

Where $E_{eq}\varepsilon_{max}$ gives the stress in the equilibrium branch and $E_j\varepsilon_j^s$ the stress in the *j-th* non-equilibrium branch before unloading. With this value we can find the strain condition at the beginning of recovery as:

$$\varepsilon_j^s(t_{0\%}) = \varepsilon_j^s(t_c) - \Delta\varepsilon \tag{8.15}$$

Where $t_{0\%}$ denotes the time at 0% recovery. The *NT* values of strain are then used as starting point to solve the system of homogenous differential equations governing the strain evolution during free recovery. Here, we first report the mathematics behind the equations used for this purpose.

Each *j-th* non-equilibrium branch is a Maxwell element (a spring-dashpot element) and the total strain in each element is the same as the one in the equilibrium branch. For the generic non-equilibrium branch *j*, we can therefore write:

$$\dot{\varepsilon} = \dot{\varepsilon_j^s} + \varepsilon_j^s/\tau_j \tag{8.16}$$

Where $\dot{\varepsilon}$ is the time derivative of the strain in the equilibrium branch, $\dot{\varepsilon_j^s}$ is the time derivative of the elastic strain (the strain of the spring element) in the *j-th* non-equilibrium branch and τ_j is the relaxation time for the *j-th* branch. We should notice that the relaxation time is a function of temperature but also that the recovery process is either isothermal or a constant rate temperature ramp and therefore the relaxation time can be translated to a constant value or a function of time. We can solve for $\dot{\varepsilon_j^s}(t)$ by applying the integral factor rule (all functions are continuous and continuously differentiable) which will give:

$$\varepsilon_j^s(t) \cdot exp \int_0^t \frac{ds}{\tau_j(s)} = \int_0^t \left[\frac{d\varepsilon}{dt}(s) \cdot exp \int_0^s \frac{dz}{\tau_j(z)}\right] ds \tag{8.17}$$

Where we introduced the dead variables *s* and *z*. We can also notice that given a certain time *t* we have:

$$\int_0^t \frac{dz}{\tau_j} = \int_0^s \frac{dz}{\tau_j} + \int_s^t \frac{dz}{\tau_j}$$

And therefore:

$$exp \int_0^t \frac{dz}{\tau_j} = exp \int_0^s \frac{dz}{\tau_j} \cdot exp \int_s^t \frac{dz}{\tau_j}$$

We can then rewrite Eq.8.17 as:

$$\varepsilon_j^s(t) = \int_0^t \left[\frac{d\varepsilon}{dt}(s) \cdot exp \int_s^t -\frac{dz}{\tau_j(z)}\right] ds \tag{8.18}$$

This equation describes the relative change in elastic strain for the *j-th* non-equilibrium branch. The absolute value can be obtained as long as the value at time equal zero is known. The stress in each non-equilibrium branch can be obtained multiplying the relative elastic modulus and elastic strain. Since during free recovery the stress is constant at zero, we have:

$$E_{eq}\dot{\varepsilon}(t) + \sum_{j=1}^{NT} E_j \dot{\varepsilon_j^s}(t) = 0 \tag{8.19}$$

And applying Eq.8.16:

$$\dot{\varepsilon_j^s} + \varepsilon_j^s/\tau_j + \sum_{j=1}^{NT} \frac{E_j}{E_{eq}} \dot{\varepsilon_j^s} = 0 \tag{8.20}$$

Which is the system of differential equations to be solved in order to find the strain evolution in each non-equilibrium branch. We can solve this system by first rewriting it in matrix form as done in Yu et al.[8] and applying eigen-analysis, or also by handling the same system to a MATLAB function like ODE15s. For both cases and for all previous calculations the MATLAB scripts can be found in the Appendix A. The total strain at any point during free recovery can be found from:

$$\varepsilon(t) = -\sum_{j=1}^{NT} \frac{E_j}{E_{eq}} \varepsilon_j^s(t) \tag{8.21}$$

Which finally allows to calculate the recovery ratio $R_r(t) = 1 - \varepsilon(t)/(\varepsilon_{max} - \Delta\varepsilon)$ and complete the shape recovery prediction model.

8.5 Stress and strain distribution in non-equilibrium branches and theoretical limit in the influence of programming conditions over the shape recovery

As shown by Yu et al. the shape recovery behaviour of the SMP modelled by the generalised model will depend upon the stress distribution in the non-equilibrium branches upon unloading. This distribution is directly influenced by the programming conditions and can be looked at as a function of the reduced programming time. This parameter would need to be calculated with respect to the whole programming, through the equation:

$$t_{r,prog} = \int_0^t \frac{dz}{\alpha_T(T)} \tag{8.22}$$

Where, once again, $\alpha_T(T)$ is the shifting factor at a certain temperature *T*. Given the way the shifting changes with temperature and given the difference in temperature between the hot and cold programming steps, the value of reduced time can be often taken as $t_{r,prog} = t_h/\alpha_T(T_h)$. In Figure 8-9 we report four stress distributions in the model branches, immediately after unloading, for different reduced programming time. The fourth distribution is the one generated due to the experimental programming conditions, i.e. T_h = 80 °C and t_h = 3600 s, which result in the reduced programming time of 2.00E+13 seconds. The first to third distributions are theoretical scenarios that can be obtained for T_h = 50 °C and t_h = {6 s; 60 s; 60000 s} and were chosen for demonstration purpose. To obtain the distributions we employed one set of model parameters (#004) and always considered an applied strain of 10%. As we can observe this results in the same stress in the equilibrium branch for all reduced time values, this would be equal to the equilibrium modulus multiplied the applied strain of 10% and therefore is independent from the value of $t_{r,prog}$. Furthermore we can notice that the first reduced time condition results in higher absolute values of stress that surpass the one in the equilibrium branch, as opposed to what we can observe in the other three cases. We can also notice that all conditions are qualitatively similar in terms of stress distribution for the first 10 branches. As the value of reduced programming time increases the stress distribution is less and less changed so that there is no quantitative difference between the last two conditions (2.22E+10 and 2.00E+13 seconds). In other words, any further increase in programming reduced time will not affect the stress distribution. This condition imposes a limit on the kind of shape recovery that can be theoretically programmed, specifically a limit in how slow the recovery can proceed. We can better see this in Figure 8-9 (e): for recovery temperature of 45 °C the four stress distributions, corresponding to four reduced programming times, will give a shape recovery behaviour that, at the slowest, will reach 90% recovery in 8

days. This qualitative behaviour is independent from the recovery temperature as we can notice from Figure 8-9 (f) where the recovery temperature is increased to 50 °C which results in the recovery curves being just shifted to lower values of time.

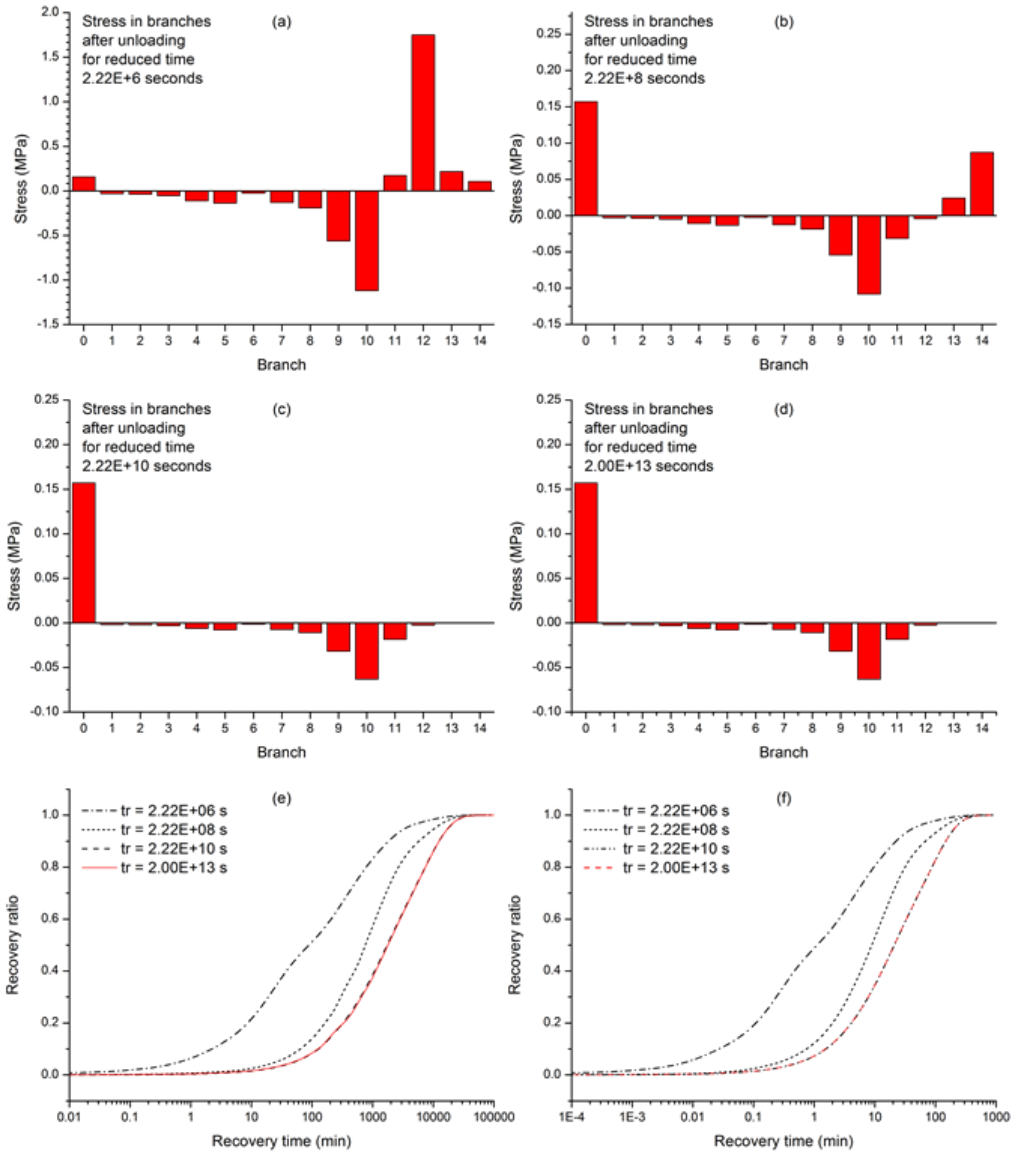

Figure 8-9 Stress distribution in the equilibrium (branch 0) and non-equilibrium (branch 1 to 14, ordered by ascending reference relaxation time) branches immediately after unloading, prediction results for different values of reduced programming time in seconds: (a) 2.22E+6; (b) 2.22E+8; (c) 2.22E+10; (d) 2.00E+13. Image (e) and (f), shape recovery predictions at 45 °C and 50 °C respectively.

8.6 Shape recovery prediction and use of time-temperature superposition

Figure 8-10 (a) reports the simulated shape recovery curves for a recovery temperature of 45 °C, each curve is generated by one set of model parameters. The eight curves cover a wide time interval, showing recovery ($R_r \simeq 95\%$) as fast as half a day and as slow as 2 years. From Figure 8-10 (b) we also observe a correlation between the reference temperature and the speed of the recovery, here represented by the time required to reach 95% shape recovery. Considering one curve produced by one set of model parameters,

we can anticipate that a change in recovery temperature will shift the recovery curve horizontally, without changing the qualitative behaviour. This can be expected given the use of the time-temperature superposition in the model. Furthermore we can calculate the horizontal shift as $|\log(\alpha_{T1}/\alpha_{T2})|$, the logarithm of the ratio of the shifting factors calculated at the two recovery temperatures (T_1 and T_2). Therefore we can conveniently look for a certain recovery condition to be met by employing the time-temperature superposition. Figure 8-11 shows such an example: we shift the 45 °C recovery curve to the right until we hit 20% recovery at one week, from the value of the shift we calculate that the recovery temperature for such behaviour to be theoretically true should be around 42.35 °C. We also observe that the eight curves in Figure 8-10 (a) can be superimposed almost perfectly. In Figure 8-12 (a) the dashed lines are the recovery curves at 45 °C for the model parameters obtained from three different specimens' temperature sweeps (004, 029, 006b). We then choose the middle curve, #004, as the reference curve. We shift the other two curves by dividing their recovery time data points by:

$$\beta = \frac{\alpha_{T_{rec}}}{\alpha_{T_{rec}}^{ref}} \tag{8.23}$$

Where $\alpha_{T_{rec}}$ is the shifting factor at the recovery temperature calculated using the model parameters pertaining to the curve to be shifted, while $\alpha_{T_{rec}}^{ref}$ is the one calculated using the model parameters of the reference. By doing so the curves shift to the solid lines position and are very close to being superimposed. The same is true for all other curves as we report in Figure 8-12 (b), though the superposition is not perfect.

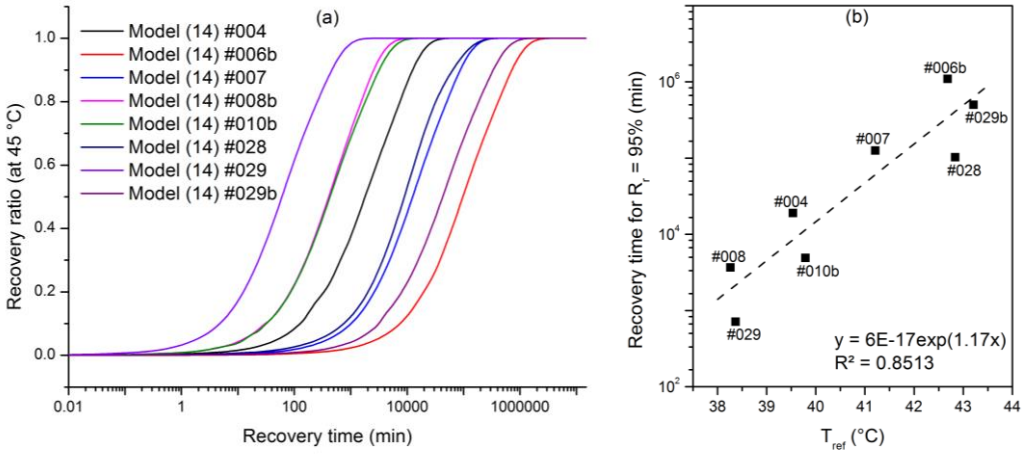

Figure 8-10 (a) Eight simulation recovery curves are obtained for recovery temperature of 45 °C; (b) the time required to reach full recovery shows a correlation to the reference temperature, even though weak.

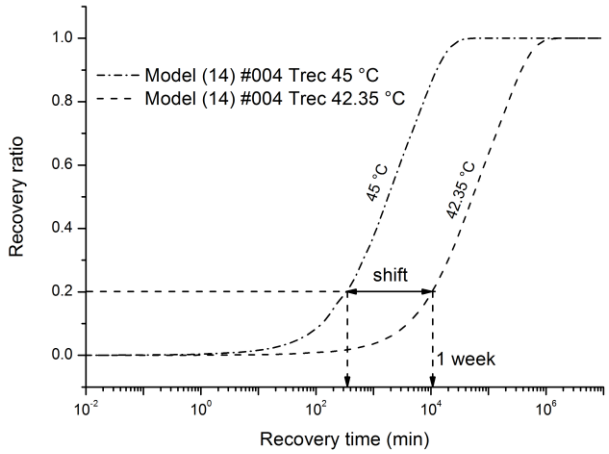

Figure 8-11 The simulated recovery curve at 45 °C is shifted to the right until the 20% recovery mark is hit at 1 week of recovery time. The horizontal shift is used to calculate the new recovery temperature of 42.35 °C.

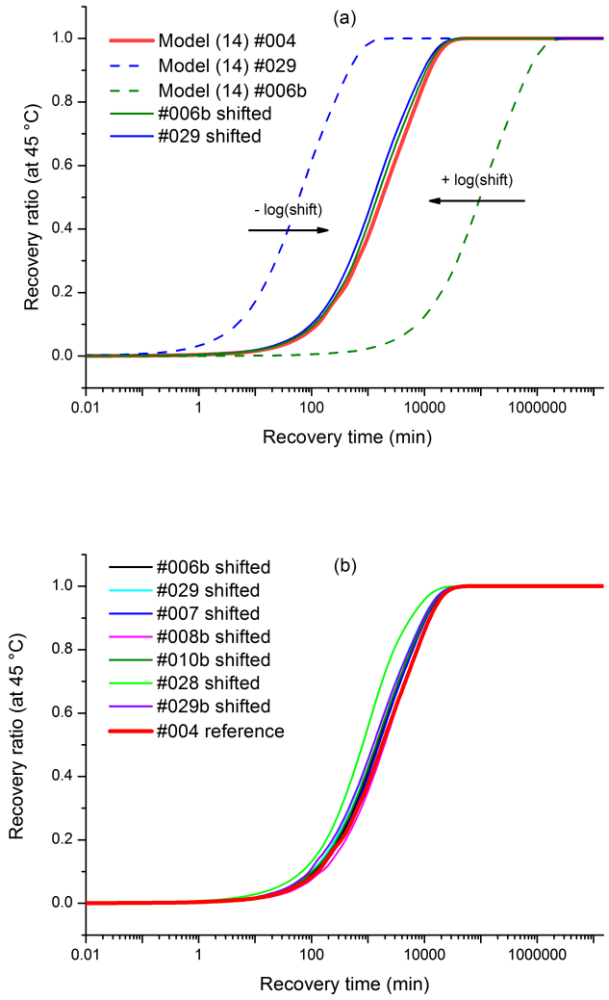

Figure 8-12 (b), (c) The recovery curves at 45 °C superimposing when one is chosen as reference curve and the others are shifted accordingly.

8.7 Prediction and experimental data comparison for shape recovery at 45, 48, 50 and 53 °C

Here we present the comparison between the experimental data for the shape recovery and the shape recovery prediction obtained from the modelling. We report the experimental recovery at 50 and 53 °C in terms of average ± SD, together with the simulated recovery curves, in Figure 8-15. We focus on the recovery at 45 °C and 48 °C, for which we report all data points for the triplicates in Figure 8-13 and Figure 8-14. Each recovery experiment follows more than one simulated curve, depending on the interval of recovery time under consideration. We observe multiple plateaus of recovery ratio, lasting for shorter or longer time, thus resulting in a dead time of the recovery process. For example, specimen 3 of the 45 °C recovery experiments reaches a first plateau around 38% recovery ratio with a dead time of 18 hours. Before this value the experimental behaviour is better represented by faster recovery curves (#008b, #010b), when the recovery resumes it follows a slower curve (#004). A second plateau can be observed around 55% recovery and lasts for 38 hours. The last plateau is reached around 96% recovery, at the end of our experimental observations, which we can assume as the plateau of the full recovery. We observe a similar behaviour for the other specimens recovered at 45 °C and also for the ones at 48 °C. The plateau values of recovery ratio are close to each other, we observe one around 30-40% recovery ratio, around 60% and for the 48 °C recovery also one around 80%. The time points at which the plateaus are observed for the different specimens are also close, though the value of the recovery ratio plateau might be different. For example, in Figure 8-13 (b) we notice that all specimens experience a plateau at around 2000 minutes of recovery time, with specimen 3 being at 55% recovery and specimens 1 and 2 being at 30% recovery. Similarly, in Figure 8-14 (b) we notice a plateau around 1200 minutes, though specimen 3 reaches 60% recovery while specimens 1 and 2 reach 80% recovery.

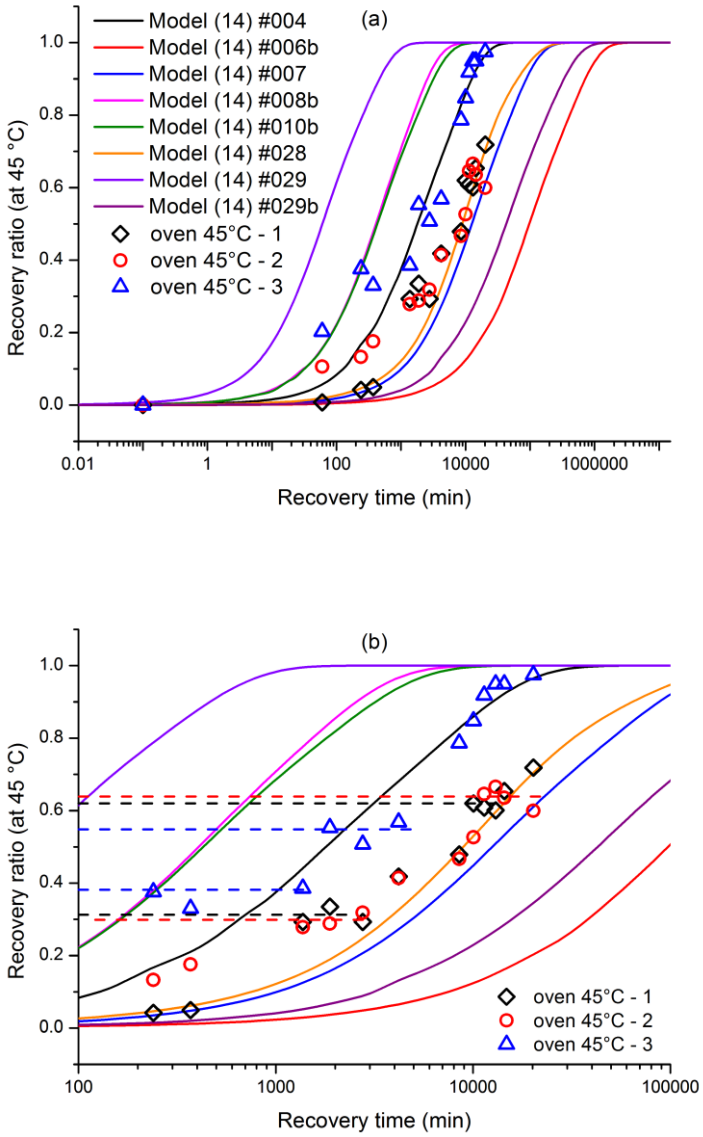

Figure 8-13 Comparison of experimental data and simulation results for shape recovery at 45 °C. The rescaling (b) shows the recovery dead times experienced during the tests, with the dashed lines indicating the relative values of recovery ratio.

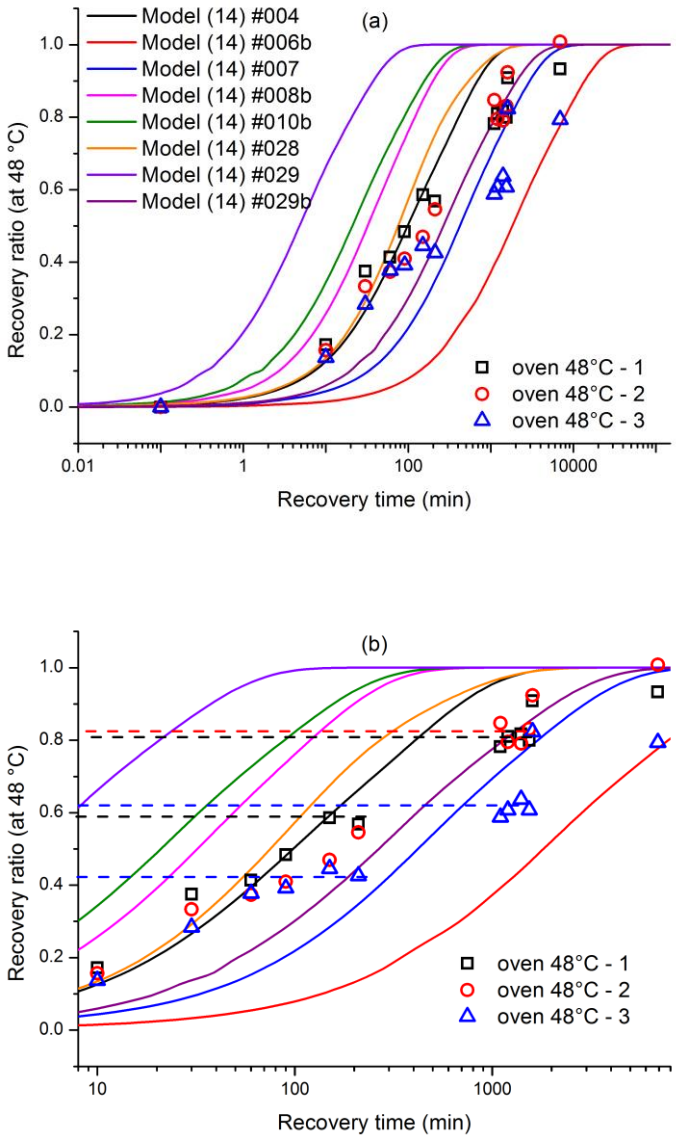

Figure 8-14 Comparison of experimental data and simulation results for shape recovery at 48 °C. The rescaling (b) shows the recovery dead times experienced during the tests, with the dashed lines indicating the relative values of recovery ratio.

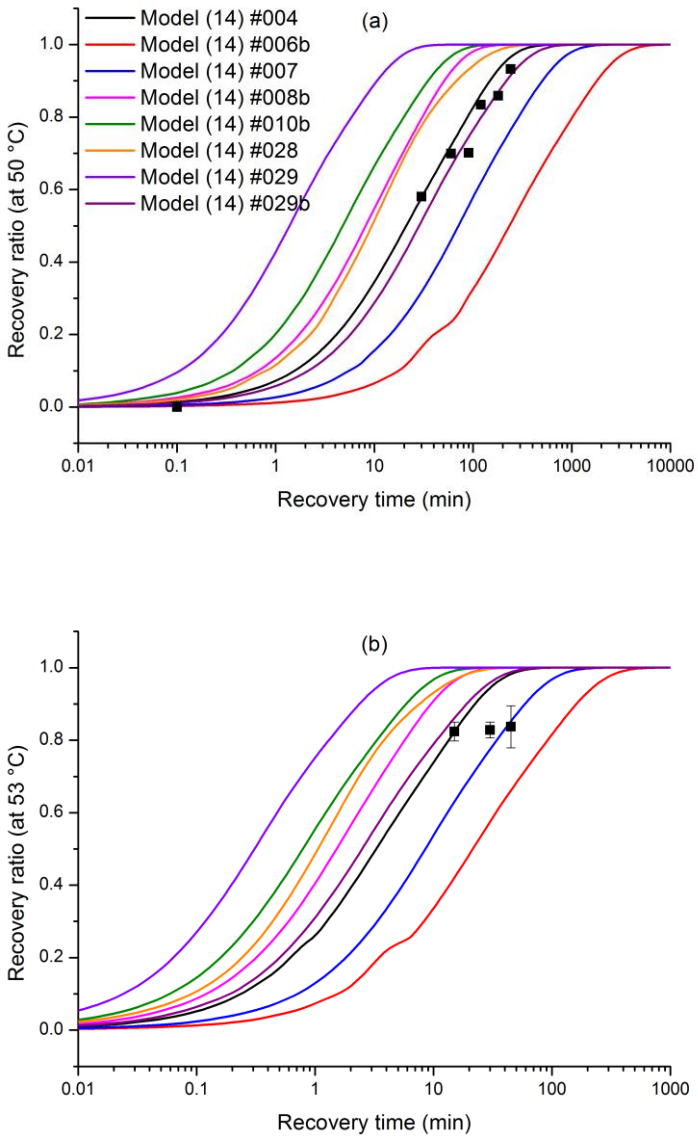

Figure 8-15 Shape recovery prediction and experimental data at recovery temperature of: (a) 50 °C; (b) 53 °C.

8.8 Simulation of temperature departure scenarios during application

We can apply the model to look at some scenarios of temperature swings during application. We will use 45 °C as the standard temperature but we will consider relative changes in temperature that could be typically encountered in a physiological application. The first scenario we can think of is a daily ± 0.5 °C temperature variation, which can be expected for body temperature and might as well be the case for the recovery tests carried out inside the oven. In this case the recovery response does not move to far from the one at constant temperature, as shown by Figure 8-16 (a). Here we are simplifying the scenario by applying a sinusoidal recovery temperature functions, written as $T_{rec} = 45 \pm 0.5\sin(\omega t)$ with ω such that the period is 24 hours. We chose ω such that the period is 16 hours and we model the response separately for each form of the temperature

equations. The recovery response differs the most where the frequency of oscillation is comparable to the recovery time scale, with an error in recovery ratio around +/- 5%. We also notice that the slower the recovery at the constant temperature, the less the influence of daily swings. For a different scenario we could think of an increase in temperature for a certain period of days, for example due to fever incurred after 3 days from the application and receding in two days. This would change the recovery profile and speed up the recovery from 9 days to 4 days (to achieve 90% recovery ratio) as shown in Figure 8-16 (b).

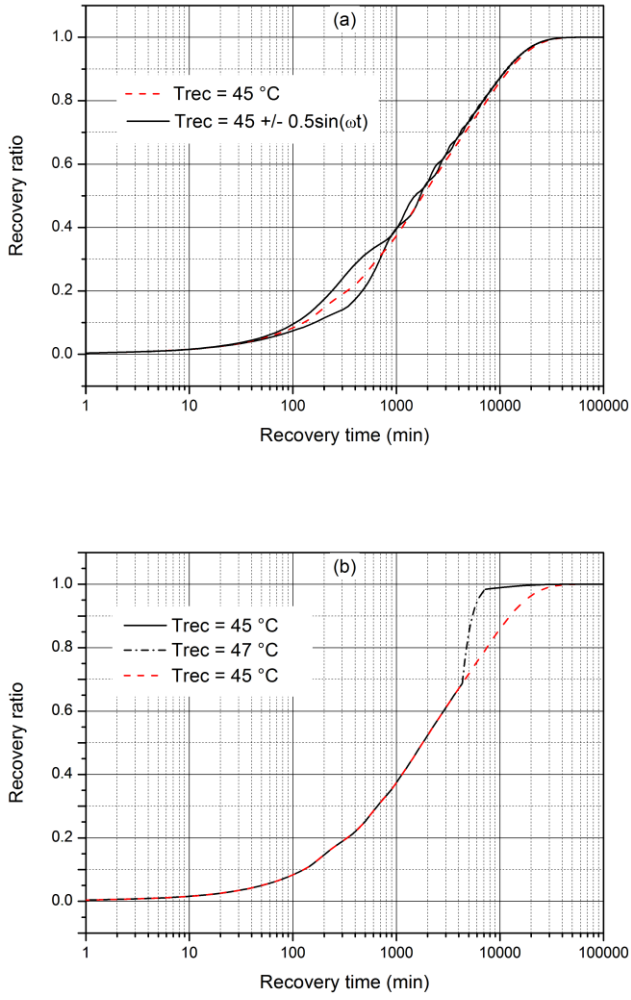

Figure 8-16 Simulations of shape recovery response. (a) Comparison of constant recovery temperature (dashed red line) and sinusoidal change in recovery temperature (solid lines). (b) The recovery temperature is increased by 2 °C for two days, resulting in an accelerated recovery profile.

8.9 Discussion

8.9.1 MC method and temperature sweep simulation

The MC method is here of relative importance as the main methodology employed to obtain the model parameters was the TS method. As we discussed in Chapter 6, we

encountered several problems in performing the stress relaxation tests required for the master curve to be built. Here we presented the fitting for the one relaxation modulus master curve we were able to produce, though we cannot trust the quantitative data and we only wish to point out some qualitative observations. From the master curve construction procedure it should be clear that the shape of the curve does not depend on the chosen reference curve. And similarly, the shifting temperature T_S does not change with different T_{ref}. Both these observations are intrinsic to the TTSP and are useful for our discussion as they show that the Arrhenius-type and WLF equations can be applied in the form of Eq.8.1 and 8.2. This is the case when $T_{ref} = T_S$ and clearly when this is true we should also have $T_{ref} = T_M = T_S$ otherwise the shifting factor calculated at T_{ref} would be different than 1. It is also useful to point out that T_S is more or less the temperature at which the isotherms start to drop in magnitude (this seems. As a result the simulated temperature sweep shows the onset in the drop in storage modulus at around the same temperature. This gives us a rule of thumb for choosing the first guess values of T_{ref} when fitting the experimental temperature sweep tests. We should notice that the temperature sweep prediction does not take into account the temperature ramp rate nor the test being conducted in cooling from the rubbery state or in heating from glassy state. As showed, this shifts the traces by a significant amount. A more complex model, able to predict this behaviour, is presented by Lei et al.[196].

8.9.2 TS method and parameters physical meaning

The temperature sweep tests were fitted to a 14 non-equilibrium branches GMM, with the TTSP being applied through Eq.8.1, 8.2 and 8.3. Each of the eight fittings closely reproduces the experimental results and results in eight different sets of parameters. We can notice how the values of T_{ref} obtained by the fitting are close to the temperature that corresponds to the onset of the storage modulus drop, this is the same qualitative observation we made for the T_S in the MC method and the same can be observed in literature[137], [138], [200], [208]. At least in part, this confirms that fitting the temperature sweep data produces a similar prediction for $\alpha_T(T)$ than what could be obtained experimentally. As it can be expected, given the experimental data, the eight sets of parameters obtained from the fitting are different from each other. At the same time, the values of AF_c/k_b are quite narrowly distributed with the exception of two values that fall far from the average. As far as we noticed, the fitting is not particularly sensitive to this parameter so that even if the value was to change by a relatively large amount, a small change in the other parameters would be enough to compensate. From the physical

point of view the parameter AF_c/k_b correlates to an apparent activation energy for the relaxation processes[144], it is therefore reasonable to find quite similar values since the eight crosslinked networks should be similar one to each other. The values of C_2 also show a large distribution but at the same time made of two groups of four data points, each group showing a narrow range. We also find no direct correlation between this parameter and T_{ref} which in this case shows a lack of physical correspondence of the model with the theory. This is because C_2 represents the drop in temperature below T_{ref} for the configurational entropy to be zero[145] and therefore for similar networks one would expect larger C_2 with larger T_{ref}. Then again the modelling reaches a solution point in a purely mathematical way, the starting point and the boundary conditions could be changed accordingly to obtain more physically coherent results, at the expense of time efficiency.

8.9.3 Stress distribution predictions and influence of the programming conditions on the shape recovery behaviour

As showed, different programming conditions will result in different reduced programming time and different stress distributions after unloading. At the same time this is only relatively true and after a large enough reduced programming time is reached the stress distribution will always be the same. This is because there is a threshold for the Maxwell elements condition during programming, namely the case in which every dashpot is completely free to move and therefore the springs do not store any of the applied deformation. Both intuitively and mathematically this clearly happens when the reduced programming time is larger than the larger reference relaxation time, so that even the "slowest" viscous component is able to fully relax. The stress distributions at the beginning of the recovery are then non-zero because of the little percentage of strain being instantaneously recovered during unloading. Since this process is fast and at very low temperature, the only components that can account for the change in strain are the springs. Therefore, those springs that had strain close to zero will go into compression as a result of the overall strain decrease and of the dashpots being frozen at the maximum deformation. Our programming conditions for experimental SMCs result in the threshold situation, so that all springs except the equilibrium one will go into compression after unloading. The elastic stresses are then different one from the other because the elastic moduli are different. These observations offer the justification to the applied programming cycle and the reason why it results in the slowest possible recovery. Any stretched elastic component would in fact cooperate with the equilibrium string to the

recovery, accelerating the process. Conversely, any spring in a compressed state will resist to the recovery, slowing down the process until its viscous counterpart gains enough mobility to be active. When all non-equilibrium elastic components are compressed, with the compression equal to the instantaneous drop in strain during unloading, the recovery proceeds at the slowest speed. This limit in how slow the recovery can be made to proceed by tailoring the programming conditions, results in the need for additional variables to be changed in order to achieve slower kinetics at a given temperature.

8.9.4 Comparison of shape recovery experimental and modelled behaviour

By looking at the free recovery experiments against the eight simulations we can notice that the experimental data is not predicted by one particular model curve. Rather, different intervals of the recovery proceed accordingly to different simulated curves. This is only possible because the experimental recovery shows one or more points at which the recovery rate will slow down for a certain dead time, before accelerating once more. This is a behaviour similar to what could be observed for multi-shape memory effect [12], though it is here not intentionally programmed and gets activated not by a temperature change but by a long enough time being elapsed. We can interpret the behaviour as the result of different regions of the network being fixed or not, after a certain time. The parts with lower relaxation time account for the initial recovery, this naturally proceeds towards a plateau value of R_r which is maintained until the parts with higher relaxation time are activated. We also notice that the recovery behaviour before and after the plateau is similar. From the Maxwell branches point of view, a large time spent with R_r at a plateau, might suggests a big gap in relaxation times. We also noticed that the values of recovery at which the plateaus are experienced are close for all specimens. Furthermore the recovery times around which the plateaus are observed are also very similar. Still, even though two specimens reach a plateau around the same time they do not necessarily share the same value of R_r. We already discussed that each recovery behaviour and therefore each plateau reached, can be addressed to different regions of the network being able to recover or not; furthermore the previous observations might relate to how these regions make for different volume fractions in different specimens. We could assume that the time points at which we observe the plateaus would be similar because the rate of recovery of a certain region is independent from its volume fraction in the network, while the recovery ratio reached at the plateau would be, e.g., larger because a larger volume stores a larger part of the deformation.

8.10 Conclusions

We modelled the material by a 1D linear viscoelasticity model, including the temperature effect by the use of the time-temperature superposition principle. The model parameters were obtained by fitting of temperature sweep dynamic analysis test results, which was found to be the most efficient way to proceed. We obtained eight sets of parameters from eight different temperature sweep tests and developed the model for each set. The high inconsistency of the experimental data showed a strong impact on the recovery simulations. The eight recovery curves that can be predicted at a certain recovery temperature, cover an exceedingly large time interval, with the experimental recovery data falling close to the centremost prediction curve. Furthermore the model is not able to predict the exact qualitative behaviour during recovery at lower temperatures, as this is characterised by one or more time points at which the recovery temporarily comes to a halt. In this particular case the complications lie in the studied polymeric networks, which show too much of an unpredictable behaviour to be modelled. The model could still be used as a theoretical means to show that the programming conditions have limited effect over the shape recovery. This limit is reached when the springs in the Maxwell elements of the model do not store any deformation by the end of the programming cycle. This observation implies that the programming alone is not enough to tailor a very diverse range of recovery.

Chapter 9 – Conclusions and future work

Here, I present an overview of the main conclusions, tying them together with the main application in mind and suggest what the results could mean in view of future work.

9.1 Conclusions in relation to the objectives of the research

All main conclusions can be reviewed in reference to the objectives summarised in Chapter 1.2.

9.1.1 Formulation of a stereolithography resin and printing of porous scaffolds

A stereolithography resin based on poly(D,L-lactide) was successfully formulated. The printing can be achieved on the desktop 3D printer we tested (Ember), though it is extremely arduous. Furthermore, the concentration of UV-absorber and the macromer need to be decreased in order to obtain this less-than-acceptable level of printing. This is a considerable compromise, as the lower amount of macromer makes the green parts weak and prone to breaking and the lower amount of absorber will result in lower resolution. On the other hand, the printing was successful on the professional printer PerFactory, where the desired amount of macromer and absorber could be used. This seems to confirm that the problem can be purely ascribed to differences in the technology in use, in particular the components involved in and the type of, peeling mechanism. The resin is based on a non-reactive diluent to minimise the amount of non-hydrolisable mass in the network. After extraction of diluent and unreacted species, the parts can be expected to be suitable for cell culture.

It was possible to print porous structures with gyroid architecture on both the desktop and the professional printer. On the Ember,only a half-cell high scaffold could be obtained, while on the PerFactory a 6 cells high scaffold was successfully printed. More testing (not allowed by the short time available) would be required, though it can be concluded conclude that printing scaffolds with pores of approximately 250 μm diameter should be possible on the PerFactory. Given the low volatility of the diluent in use, an additional approach would be to heat the printing vat in order to lower viscosity. In the case of the Ember, this might solve the problems related to jamming during peeling; in the case of the PerFactory it might allow for more macromer to be used, which has the benefit to produce stronger green parts and reduce shrinking after post-processing.

9.1.2 Experimental observation of prolonged recovery

It was possible to demonstrate a prolonged shape recovery of around 7-10 days. This was obtained by programming the networks at high programming temperature and long

programming time (80 °C and 60 minutes). This kind of programming was chosen to ensure the longest possible recovery, this choice relates to one of themain hypotheses (#4). This type of prolonged recovery is, to this day, the only example in SMPs research. It forms a good precedent and evidence for future research where the shape memory application should have a delayed aspect to it, rather than having fast actuation. Together with the week-long recovery, evidence of faster recoveries that are also outside the time length of what usually reported, was provided by this research. Furthermore, a six months long investigation of the shape memory behaviour of networks stored at 37 and 20 °C, showed that the deformation is retained for this length of time and then recovered by heating. Possibly, similar experiments must have been carried out by other research groups, but they are typically not reported. It was found that the observed recovery behaviours were not all the same. This relates to the non-reproducibility of the polymer viscoelastic behaviour, as seen in Chapter 6, which can be addressed to the photo-crosslinking process resulting in dissimilar networks. Additionally, the slow recovery at 45 °C proceeds through one or two plateaus during which the recovery stops. This behaviour can be liken to a multiple shape memory effect activated by the passing of time. It can be related to network heterogeneity causing some recovery kinetics to be apart in terms of relaxation time, so that some activate and come to end before the next can also activate, which results in dead times of recovery.

9.1.3 Modelling the shape recovery

I made use of a combination of 1D linear viscoelasticity modelling approaches found in literature to predict the shape recovery of the networks. To identify the model parameters, a simultaneous fit of the tanδ and storage modulus curves obtained from DMA analysis in temperature sweep (TS method) was performed. This kind of test is very practical and standardised, which are its main advantages. Considering the time required to run one temperature sweep and the time required to obtain a good fitting on the MATLAB script, the model parameters could be obtained in around 2 hours. The other tested approach, is based on the construction and fitting of a master curve. This has the advantage of giving direct information on the shifting factors but, in our experience, it is several times slower than the TS method. Each application of the TS method resulted in extremely good fitting of the experimental curves. The model to predict the shape recovery was then developed on the basis of the parameters obtained through this fitting method. This allowed to show that that the programming conditions have limited effect on the recovery, which was one of the hypotheses and a very important consideration when designing this kind of

prolonged recoveries. The model was employed to predict the shape recovery of the specimens under their programming conditions. Due to the already discussed spread in the experimental parameters, it was only possible to predict that the recovery ratio curve would fall in a certain, very large, area. This is the main drawback of our research and can only be addressed by improving the material fabrication to obtain more homogeneous networks.

9.2 Results in view of the proposed application

The main application in mind during this study is based on exploiting the shape memory biopolymers to deliver a new standard in tissue engineering scaffolds, where the seeded 3D construct can recover from a compressed state to allow progressively increasing volume to be available for tissue formation. Unfortunately, there are no studies that demonstrate the ability of shape memory polymers to recover the imparted deformation over the kind of time length required for this application (we can imagine that recovery over few weeks would be the minimal requirement). Typically, the focus is on fast actuation of the memory effect; slow recovery kinetic is often intended as tens of minutes and it is not desirable for many applications. Our results showed that recovery over 7-10 days is possible, which is a basic requirement to consider continuation of the research towards the intended purpose. Still, more considerations need to be discussed to contextualise the present work with the application in mind and to try and direct future research.

45 °C was the lowest temperature at which the recovery could be observed, conversely, the deformation was retained when at 37 °C. For biomedical application the recovery should activate at 37 °C. It seems reasonable to assume that the determining factor for the actuation of the recovery is how far the recovery temperature is from the onset of the glass transition, which can be considered the temperature at which the faster relaxation kinetics activate. Therefore, the polymer would need to be modified in a way to lower the onset point to around 36.5 °C. Lowering the glass transition temperature could be one way to do this. Another way would be by broadening the glass transition range. Taking a step back, it cannot be excluded that the recovery of the porous scaffold would be actuated even when using the same PDLLA as bulk material. For example, water uptake after few days might have enough of a plasticizing effect to initiate the shape recovery. Repeating the 37 °C recovery tests in wet condition should elucidate if the water uptake has any significant effect on the shape memory behaviour and, therefore, give an indication of the extent to which the onset temperature should be lowered.

Even though a slow recovery was observed, the time length suitable for tissue formation might require several more weeks. This is probably the most complicated aspect to work on. One can speculate that there is a limit to the kind of recovery kinetic that can be obtained for a certain material. We would require to modify the polymer to unlock longer recoveries. This would probably mean increasing the molecular weight, which is problematic as it results in greater resin viscosity and might decrease the solubility of the macromer in the diluent. One more related observation is that the initial recovery proceeds at a fast pace. This would not fit the application; therefore, I suggest that the initial recovery could be "discarded". This means that the construct would first be strained and fixed; then, prior application, it would be left to undergo the fast recovery and fixed again by quenching. Under the assumption that the following recovery would proceed through the same path independently from this additional step, the required slow recovery kinetics would then be provided. In this sense, the observed dead times in recovery can be exploited as they create a recognisable steady state condition. There are probably many complications related to this approach. For one, the construct would have to be compressed more than what theoretically required. Also, the overall strategy becomes more time consuming and susceptible to errors. At the same time, it seems the most straightforward approach.

The imparted strain and the 2D geometry of the specimens are far from the actual application and one should wonder what could be expected for a 3D porous scaffold compressed to, say, 50% of its volume. As for the geometry, we can at least take this research as indication that the struts forming the 3D construct could display a similar shape memory behaviour. As for the strain, we observed some preliminary results (here not reported) where the same networks can recover from large deformations (around 100%), displaying what could be described as reversible plasticity. This is also a good indication that the bulk material could be compressed significantly and still be able to recover.

One aspect of prolonged recovery that was not fully investigated during this research is the extent of recovery stress under constrained conditions. From preliminary results (here not reported) the force generated by the SMPs during constrained recovery at body temperature is 0.06 N at most. In general we can expect that to obtain slow recovery the force generated by the SMP against constrains would be small, this is because few recovery kinetics would be in play at the same time. Furthermore, the viscoelastic modelling of an SMP programmed for slow recovery shows that the elastic components in the non-equilibrium branches before recovery are characterised by strain opposite in

sign to the overall strain of the system (the strain of the equilibrium branch). This means that the stresses stored by the elastic components are also opposite to the overall stress generated during constrained recovery. Overall, it can be suspected that small forces (few grams force) would be able to constrain the recovery, which could exclude the *in vivo* application of such SMPs.

One pressing point for future research would be to verify to what extent stereolithography printing of our resin results in heterogeneous parts and to compare our results against thermally crosslinked networks. The reversible plasticity behaviour should also be investigated, as it could be interesting for minimally invasive surgery applications other than the present one. The model should also be tested against commercial SMPs and eventually modified to be able to work for large deformations (examples of this can be found in literature, e.g. Diani et al. [136]). The printing tests should also be continued on a professional printer and the printed scaffolds should be tested for their shape recovery behaviour. As already stated, the recovery under wet conditions should also be investigated.

To summarise, the present work can only provide an evidence that slow recoveries can be obtained. In turn, this gives justification to follow up with future research moving towards the envisioned scaffold application.

Appendix A: MATLAB scripts

We report the scripts in use to obtain the parameters for the generalised Maxwell model through the two methodologies and to solve the shape memory cycle. The scripts are partially edited to save space, in that we removed some comments. The text is changed to black and white to keep the use of colour on this document to a minimum, the font is kept as per MATLAB.

Scripts to fit the master curve

PronyErrorNT

This is the function for the error between experimental data and calculated data when the calculation is done by the GMM framework with some variables values. This function gets handled to the next script (MinimisePronyErrorNT).

```
PronyErrorNT v1.1 by Alberto Di Bartolo
function error_tot = PronyErrorNT(var)
NT = 14; % n.e. branches (user input) (should be the same as in
minimisePronyErrorNT)
load Your_MC_data.mat % load experimental data to fit. time var
% should be named "redtime" and modulus should be named "relmod"
E0 = relmod(end); % value of rubbery plateau
Evec = var(1:NT); % elastic moduli in branches
tauvec = var(NT+1:NT+NT); % relax times vector
Eloop=zeros(1,NT); % preallocates a vector used in the loop
Erel_calc = zeros(size(redtime)); % preallocates calculated values
errors = zeros(size(redtime)); % preallocates errors
% Now we calculate the modulus at time(i)
for i=1:numel(redtime)
    for j=1:NT
        Eloop(j) =  Evec(j).*exp(-redtime(i)./tauvec(j)); % for time(i),
        % calculate each Evec*exp(-t/tau) and store the value in the
vector
        % Eloop
    end
Erel_calc(i) = E0 + sum(Eloop); % summ all the values in Eloop and add
E0
errors(i) = (Erel_calc(i)./relmod(i)-1).^2; % calculate the error at
time(i)
end
error_tot = sum(errors);
% make sure the values are in the base workspace by assigning them
assignin('base','redtime',redtime);
assignin('base','relmod',relmod);
assignin('base','Erel_calc',Erel_calc);
end
% end of PronyErrorNT
```

MinimisePronyErrorNT

This is the script that gets handled the previous error function to be minimised and to find the best values. It also contains some lines to output a report on the result and generate a figure to compare model and experiment.

```
minimisePronyErrorNT v1.0 by Alberto Di Bartolo
        NT = 14; % number of non-eq branches (should be the same as in
PronyErrorNT)
        tausmallest = -11; % the smallest value of tau is
10^(tausmallest)
        divdec = 1; % tau values are logspaced but like 10^(1/divdec)
10^(1/divdec + 1/divdec), eg 10^0.5 10^1 10^1.5
        load Your_MC_data.mat % load your experimental MC data
        Etot = relmod(1); % the sum of E0 and all other moduli
        E0 = relmod(end); % the equilibrium modulus, modulus at rubbery
plateau
        % Build Vector zero (the first try)
        zero(1:NT) = rand(1,NT).*Etot; % moduli zero
        zero(NT+1:NT+NT) = logspace(0,NT-1,NT); % relax times zero
        % equality constr Aeq*x=beq, the sum of all moduli is Etot
        Aeq = zeros(NT+NT);
        Aeq(1,:) = [ones(1,NT) zeros(1,NT)];
        beq = zeros(NT+NT,1); beq(1) = Etot-E0;
        % inequality constr A*x<=b, if desired the moduli values are
forced to be in descending order i.e. E(NT)<E(NT-1)<...<E1
        A = zeros(NT+NT); A1=A; A2=A;
        A1(2:NT,1:NT-1)=-eye(NT-1);
        A2(2:NT,2:NT)=eye(NT-1);
        A=A1+A2;
        b = zeros(2*NT,1);
        % boundaries cond
        Elb = zeros(1,NT);
        Eub = ones(1,NT).*(Etot-E0);
        taulb = logspace(tausmallest,NT/divdec+tausmallest1/divdec,NT);
        tauub = taulb; % set tau values a priori
        % tauub = ones(1,NT).*Inf; % tau values are not set a priori
        lb = [Elb taulb];
        ub = [Eub tauub];
    else
    end
%%%% FMINCON
options=optimset('MaxFunEvals',5000,'MaxIter',1000,'TolFun',0,'TolX',0
);
    minimum=fmincon(@PronyErrorNT,zero,A,b,Aeq,beq,lb,ub,[],options);
%%%% Results
    minvalues.E0 = E0;
    minvalues.Ei = minimum(1:NT);
    minvalues.taui = minimum(NT+1:NT+NT);
    PronyErrorNT(minimum);
    figure()
    semilogx(redtime,Erel_calc)
    hold on
    semilogx(redtime,relmod)
    xlabel('Reduced time (min)')
    ylabel('Relaxation modulus (MPa)')
    legend('model','experiment')
    hold off
    error = PronyErrorNT(minimum)
    para = minimum(:); % for later use
    % (all results should always be saved with the same kind of name)
end
%end of minimisePronyErrorNT
```

Scripts to fit the temperature sweep

LSQFitNT

This is the function for the error between experimental values of storage modulus and tanδ and the values calculated using the GMM with the time temperature superposition equations to include the temperature dependency. This function gets handled to the next script.

```
%{
LSQFitNT v1.2 by Alberto Di Bartolo
Correct order for the data in var is:
Tref,WLF1,WLF2,ARR,E0,Evec,tauvec
with:
Tref reference temperature
WLF1 WLF equation C1
WLF2 WLF equation C2
ARR AFc/kb the Arrhenius equation slope
E0 rubbery plateau (script will get it from the data)
Evec vector with NT elements for the NT moduli
tauvec vector with NT elements for the NT relaxation times
The data should be named: temperature, storage, tandelta. And be in
column vector form
%}
function total_error = LSQFitNT(var)
NT = 14; % # of non-equi branches (should be the same as in
minimise_LSQFitNT)
% temperature intervals for weighting the errors if desired
tempLeft = 37; % left of tan delta peak
tempRight = 52; % right of tan delta peak
tempOnset = 27; % onset of tan delta
A = 100; % tand weight
B = 1; % mod weight
C = 1000; % tand weight
D = 1; % mod weight
E = 1000; % tand weight
F = 1; % mod weight
load data.mat % load data
temp_data = temperature; Estor_data = storage; tand_data = tandelta;
Tref = var(1); % the reference temperature
WLF1 = var(2); % WLF equation paramter
WLF2 = var(3); % WLF equation paramter
ARR = var(4); % Arrhenius equation parameter
E0 = var(5); % value of rubbery plateau
Evec = var(6:(5+NT)); % vector of NT elastic moduli
tauvec = var((5+NT+1):(5+NT+NT)); % vector of NT relaxation times at
Tref
w = 1; % frequency [Hz]
% Preallocate
at=zeros(size(temperature));
Estor_calc=zeros(size(temperature));
Estor_loop=zeros(1,NT);
Eloss_loop=zeros(1,NT);
Eloss_calc=zeros(size(temperature));
tand_calc=zeros(size(temperature));
errors_tand=zeros(size(temperature));
errors_storage=zeros(size(temperature));
%{
for each value of temperature temp_data(i):
calcualte the shifting factor (at) from WLF or ARR
calculate the storage modulus as:
```

```
calculate the loss modulus as:
calculate the tan delta from the ratio
%}
for i = 1:numel(temp_data)
    %calc shift factor at T(i)
    if temp_data(i) >= Tref
        at(i)   =   10.^((-WLF1).*(temp_data(i)   -   Tref)./(WLF2   +
temp_data(i) - Tref)); % WLF
    else
        at(i)  =  exp((-ARR).*(1./(273.15  +  temp_data(i))-1./(Tref  +
273.15))); % Arrhenius
    end
    %calculate E' and E'' and tandelta at T(i)
    for j=1:NT

Estor_loop(j)=Evec(j).*((w.*tauvec(j).*at(i)).^2)./(1+(w.*tauvec(j).*a
t(i)).^2);

Eloss_loop(j)=Evec(j).*((w.*tauvec(j).*at(i)))./(1+(w.*tauvec(j).*at(i
)).^2);
    end
    Estor_calc(i)=sum(Estor_loop)+E0;
    Eloss_calc(i)=sum(Eloss_loop);
    tand_calc(i)=Eloss_calc(i)./Estor_calc(i);
    %calculate error at T(i)
    if 0 < temp_data(i) < tempOnset
%        errors_tand(i)  =  A.*(tand_calc(i)./tand_data(i)  -  1);  %  in
percentage
%     errors_storage(i) = B.*(Estore_calc(i)./Estore_data(i) - 1); % in
percentage
    errors_tand(i) = A.*(tand_calc(i) - tand_data(i));
    errors_storage(i) = B.*(Estor_calc(i) - Estor_data(i));
    elseif tempLeft < temp_data(i) < tempRight
%        errors_tand(i)  =  C.*(tand_calc(i)./tand_data(i)  -  1);  %  in
percentage
%     errors_storage(i) = D.*(Estore_calc(i)./Estore_data(i) - 1); % in
percentage
    errors_tand(i) = C.*(tand_calc(i) - tand_data(i));
    errors_storage(i) = D.*(Estor_calc(i) - Estor_data(i));
    else
%        errors_tand(i)  =  E.*(tand_calc(i)./tand_data(i)  -  1);  %  in
percentage
%     errors_storage(i) = F.*(Estore_calc(i)./Estore_data(i) - 1); % in
percentage
    errors_tand(i) = E.*(tand_calc(i) - tand_data(i));
    errors_storage(i) = F.*(Estor_calc(i) - Estor_data(i));
    end
end
total_error = [errors_tand errors_storage];
assignin('base','temperature',temp_data);
assignin('base','modulusCalculatedValues',Estor_calc);
assignin('base','tandeltaCalculatedValues',tand_calc);
assignin('base','modulusExperimentalValues',Estor_data);
assignin('base','tandeltaExperimentalValues',tand_data);
assignin('base','shift',at);
end
% end of LSQFitNT.m
```

minimise_LSQFitNT

Script that gets handled the previous function and outputs variables values that minimise the error. For this script we found convenient to introduce some basic user input messages.

```
%{
minimise_LSQFitNT v1.2 by Alberto Di Bartolo
%}
close all
tic
NT = 14; % number of ne branches
first_tau = -4; % the smallest value of tau is equal to 10^(first_tau)
divdec = 1; % the decades will be spaced 10^1/divdec, e.g. divdec=2
gives 10^-1 10^-0.5 etc
dataname = 'YuetAl_tempRamp_DATA'; % name of file.mat containing data
load(dataname)
% User is asked some questions
% prevent pop-up figures if requested
answer = questdlg('Disable figures pop-up?');
switch answer
    case 'Yes'
        popup = 'off';
    case 'No'
        popup = 'on';
    case 'Cancel'
        popup = 'on';
end
repeat = inputdlg('How many repetition would you like to
perform?','Repetition number',[1 50],{'10'}); % ask how many rep to do
repeat = str2double(repeat);
for q=1:(repeat) % repeat with different starting point
%% BUILD STARTING POINT (vector called zero)
Trefzero = 27;
WLF1zero = 17;
WLF2zero = 51;
ARRzero = -40000;
% some extra options
% ARRvec = [1000 2500 5000 8000 10000 15000 20000 30000 50000 100000];
% ARRzero = -ARRvec(q);
% Randomise the first 4 zero variables in a certain range
% Trefzero = randi([0 80]);
% WLF1zero = randi([0 200]);
% WLF2zero = randi([0 200]);
% ARRzero = -randi([0 100000]);
E0 = storage(end); % experimental value
Etot = max(storage); % experimental value
zero(1) = Trefzero;
zero(2) = WLF1zero;
zero(3) = WLF2zero;
zero(4) = ARRzero;
zero(5) = E0;
% Preparations to make moduli starting vector
% Comment one out
% #1 log spaced moduli values
% utility=logspace(NT-1,0,NT); utility=utility/sum(utility);
% #2 rand descending moduli values
utility=rand(1,NT);                         utility=utility/sum(utility);
utility=sort(utility,'descend');
zero(6:(5+NT))=utility.*(Etot-E0); % moduli starting vector that adds
up to Etot-E0
```

```
zero((5+NT+1):(5+NT+NT))= logspace(0,NT-1,NT); % logspaced relax times
starting vector
startpoint(q,:) = zero; % save all the different starting points
w = 1; % the experiment frequency is 1 for most cases
%% LOWER AND UPPER BOUNDARIES (vectors lb and ub)
% set VARlb = VARub to lock VAR to a certain value
% Use the following lines when locking some or all of the first 4
variables
% (just to be faster when trying different solutions)
% Treflb = 41.79;
% Trefub = Treflb;
% WLF1lb = 8.93;
% WLF1ub = WLF1lb;
% WLF2lb = 12.14;
% WLF2ub = WLF2lb;
% ARRlb = -21376;
% ARRub = ARRlb;
Treflb = 0;
Trefub = 60;
WLF1lb = 0;
WLF1ub = 200;
WLF2lb = 0;
WLF2ub = 200;
ARRlb = -inf;
ARRub = -0;
E0lb = E0; % always locked
E0ub = E0; % always locked
% lb and ub vectors for moduli
Elb = zeros(1,NT);
Eub = ones(1,NT).*(Etot-E0);
% lb and ub vectors for relax times
taulb = logspace(first_tau,NT/divdec-1/divdec+first_tau,NT);
% taulb = zeros(1,NT); % opt
% taulb = ones(1,NT).*0.001; % opt
tauub = taulb;
% tauub = ones(1,NT).*1e14; %opt
% compose lower and upper boundaries vectors
lb = [Treflb,WLF1lb,WLF2lb,ARRlb,E0lb,Elb,taulb];
ub = [Trefub,WLF1ub,WLF2ub,ARRub,E0ub,Eub,tauub];
% lb = minimum; ub=minimum;
% lb(4)=-inf; ub(4)=0;
%% Functions: comment out to choose function/options
% options = optimset('MaxFunEvals',3000,'MaxIter',1000); % standard
Tolerance
%                                options                                =
optimset('MaxFunEvals',100000,'MaxIter',5000,'TolFun',0,'TolX',0);    %
zero tolerance
% minimum = lsqnonlin(@LSQFitNT,zero,lb,ub,options);
[minimum,resnorm] = lsqnonlin(@LSQFitNT,zero,lb,ub);
%% OUTPUT
% this creates a strut called minvalues
optimal(:,q) = minimum;
minvalues.Tref = minimum(1);
minvalues.WLF1 = minimum(2);
minvalues.WLF2 = minimum(3);
minvalues.ARR = minimum(4);
minvalues.E0 = minimum(5);
minvalues.Evec = minimum(6:(5+NT));
minvalues.tauvec = minimum((5+NT+1):(5+NT+NT));
% error = LSQFitStorage(minimum);
disp(minvalues)
disp(q)
disp(resnorm)
% disp(error)
```

```
%% PLOTS - the model curves are plotted against the experimental curves
figurename = [dataname,'_OPTIMISED_',num2str(q),'.png'];
f = figure('visible',popup);
% f = figure('visible','off');
plot(temperature,modulusCalculatedValues,'r--');
% semilogy(temperature,modulusCalculatedValues,'k--');
xlabel('Temperature (°C)'); ylabel('Storage Modulus (MPa)'); ylim([1
storage(1).*1.15]); xlim([0 temperature(end)+10]);
hold on;
plot(temperature,modulusExperimentalValues,'k-');
% semilogy(temperature,modulusExperimentalValues,'k-');
legend('model','experiment');
yyaxis right
plot(temperature,tandeltaCalculatedValues,'r--'); ylabel('tan\delta');
plot(temperature,tandeltaExperimentalValues,'k-');
legend('model','experiment');
%% SAVE FIGURE in .png - DISABLE TO IMPROVE PERFORMANCE
% saveas(f,figurename);
% print('Plot','-dpng');
% % % end
%% RESULTS - disable to save time
% error = ; % funtion(minimum)
% mincol = transpose(minimum);
% start = transpose(zero);
% lower = transpose(lb);
% upper = transpose(ub);
%                                 TgData                                  =
temperature(find(tandeltaExperimentalValues==max(tandeltaExperimentalV
alues)));
%                                 TgCalc                                  =
temperature(find(tandeltaCalculatedValues==max(tandeltaCalculatedValue
s)));
% result(1:5+NT+NT,1) = start; result(1:(5+NT+NT),2) = mincol;
% result(1:(5+NT+NT),3) = lower; result(1:(5+NT+NT),4) = upper;
% result((5+NT+NT+1),2) = NaN; result((5+NT+NT+1),1) = NaN;
% result((5+NT+NT+2),2) = TgCalc;
% result((5+NT+NT+3),2) = TgData;
% result((5+NT+NT+4),2) = TgData-TgCalc;
%           result((5+NT+NT+1):(5+NT+NT+4),1)           =           NaN;
result((5+NT+NT+1):(5+NT+NT+4),3:4) = NaN;
%% EXPORT RESULTS TO EXCEL - DISABLE TO IMPROVE PERFORMANCE
%% export results to excel sheet (NT = 7)
%                                 rows                                    =
{'Tref';'WLF1';'WLF2';'ARR';'E0';'E1';'E2';'E3';'E4';'E5';'E6';'E7';'t
auref1';'tauref2';'tauref3';'tauref4';'tauref5';'tauref6';'tauref7';'e
rror';'TgCalc';'TgData';'Tgerr'};
%                                  LOG                                    =
table(rows,result(:,1),result(:,2),result(:,3),result(:,4),'VariableNa
mes',{'name' 'zero' 'min' 'LB' 'UB'});
% filename = [dataname,'_OPTIMISED_',num2str(q),'.xlsx'];
% writetable(LOG,filename);
%% export results to excel sheet (NT = 14)
%                                 rows                                    =
{'Tref';'WLF1';'WLF2';'ARR';'E0';'E1';'E2';'E3';'E4';'E5';'E6';'E7';'E
8';'E9';'E10';'E11';'E12';'E13';'E14';'tauref1';'tauref2';'tauref3';'t
auref4';'tauref5';'tauref6';'tauref7';'tauref8';'tauref9';'tauref10';'
tauref11';'tauref12';'tauref13';'tauref14';'error';'TgCalc';'TgData';'
Tgerr'};
%                                  LOG                                    =
table(rows,result(:,1),result(:,2),result(:,3),result(:,4),'VariableNa
mes',{'name' 'zero' 'min' 'LB' 'UB'});
% filename = [dataname,'_OPTIMISED_',num2str(q),'.xlsx'];
% writetable(LOG,filename);
%
```

```
end % of repeat
%
% elapsed time
toc
elapsedTime = toc;
% choose best min
prompt = 'Which solution would you like to use as optimal parameters
set? (scroll up to see all possible solutions)';
solnumb = input(prompt);
disp(['You picked solution ',num2str(solnumb)])
para = optimal(:,solnumb);
% would you like to clear all vars except for para ans save as?
if repeat>1
answer = questdlg('Would you like to clear all variables except for
para? (dataname and NT cannot be cleared)');
    switch answer
        case 'Yes'
        clearvars -except para dataname NT optimal
        case 'No'
        case 'Cancel'
    end
else
end
answer    =    questdlg(['Would    you    like    to    save    as    '
dataname,'_OPTIMISED_',num2str(NT),'.mat (if file already exists I will
ask you before overwriting)']);
if exist([dataname,'_OPTIMISED_',num2str(NT),'.mat'], 'file') == 0
    switch answer
        case 'Yes'
            save ([dataname,'_OPTIMISED_',num2str(NT)])
        case 'No'
        case 'Cancel'
    end
else
answer = questdlg('File already exists, would you like to overwrite
it?');
    switch answer
        case 'Yes'
            save ([dataname,'_OPTIMISED_',num2str(NT)])
        case 'No'
            for ii=2:10
                if
exist([dataname,'_OPTIMISED_',num2str(NT),'_0',num2str(ii),'.mat'],'fi
le')==2

                else

save([dataname,'_OPTIMISED_',num2str(NT),'_0',num2str(ii)]);
                    msgbox(['File                saved                as
',dataname,'_OPTIMISED_',num2str(NT),'_0',num2str(ii),'.mat'])
                    ['File                    saved                    as
',dataname,'_OPTIMISED_',num2str(NT),'_0',num2str(ii),'.mat']
                    break
                end
            end
        case 'Cancel'
    end
end
%% END
```

Scripts to solve the shape memory cycle

StressStrainCalcNT

This script calculates stress/strain condition at the different steps during programming. The final condition is required to solve the system of differential equations during shape recovery. The data required is obtained from the previous scripts.

```
%% StressStrainCalcNT v2.1 by Alberto Di Bartolo
% CALCULATES STRESS AND STRAIN AT END OF DIFFERENT STEPS AND PROVIDES
THE INITIAL VALUE TO SOLVE THE STRAIN EVOLUTION DURING RECOVERY STEP
clear all
close all;
% Needs a file.mat called para in the workspace, para contains the
% parameters obtained from the fitting
load Your_data.mat
NT = 14;
para=para(:);
Tref = para(1);
WLF1 = para(2);
WLF2 = para(3);
ARR = para(4);
E0 = para(5);
Evec = para(6:5+NT);
Evec = transpose(Evec);
tauvec = para(6+NT:end);
tauvec = transpose(tauvec); % s
% SMC parameters
emax = 0.2;
% erate = inf;
Th = 30;
th = 600; % s
Tc = 20;
tc = 3600; % s
qc = -2.5/60; % hypothetical fast cooling °C/s
%% relaxation times at T calculation
if Th > Tref
        ath = 10.^((-WLF1).*(Th - Tref)./(WLF2 + Th - Tref)); % WLF
        disp('ath is WLF')
    else
        ath  =  exp((-ARR).*(1./(273.15  +  Th)-1./(Tref  +  273.15)));  %
Arrhenius
        disp('ath is ARR')
end
%% ==HOLDING AT Th==
% at the programming temperature Th, if the loading is istantaneous then
% the stress in each branch at the end of holding is:
% stress_i = E_i*emax*exp(-th/tau_i)
% with emax*exp(-th/tau_i) beinf the strain at the end of the holding
tauexp_holding = -ones(1,NT).*th./tauvec./ath; % th/(at*tauref) vector
tauexp_holding = exp(tauexp_holding); % take exp vector
ee_holding = ones(1,NT).*emax.*tauexp_holding; % ee = 0 + exp(-th/tau)
vector
% the stress differs by only Ei
stress_holding = Evec.*ee_holding;
tr_h = th/ath; % reduced programming time
disp('reduced programming time is')
disp(tr_h)
%% ==COOLING==
% the first part of cooling step is a temperature ramp
% it's still a stress relaxation process with changing temperature
```

```
% solve it by approximation of the integration
% deei/dt = -dt/taui >> ln(eei/eei(stab) = -int dt/taui ~= - sum
deltat/taui
% where the time is divided in small intervals deltat and at each point
we
% calculate deltat/taui and finally sum them all together
% if Th>Tref from Th to Tref use WLF
if Th>Tref
    ramptime_WLF_cooling = (Tref-Th)/qc;
    deltat_WLF_cooling = 0.1;
    time_WLF_cooling                                                    =
deltat_WLF_cooling:deltat_WLF_cooling:ramptime_WLF_cooling;
    for i=1:numel(time_WLF_cooling)
        T_WLF_cooling(i) = Th+qc*time_WLF_cooling(i);
        at_WLF_cooling(i)    =    10.^((-WLF1).*(T_WLF_cooling(i)    -
Tref)./(WLF2 + T_WLF_cooling(i) - Tref));
        for j=1:NT
        dttau_WLF_cooling_matrix(i,j)                                   =
deltat_WLF_cooling./at_WLF_cooling(i)./tauvec(j);
        end
    end
    for j=1:NT
        int_tau_WLF_cooling(j) = sum(dttau_WLF_cooling_matrix(:,j));
        ee_WLF_cooling(j)            =            ee_holding(j).*exp(-
int_tau_WLF_cooling(j));
        stress_WLF_cooling(j) = Evec(j).*ee_WLF_cooling(j);
    end
    % from Tref to Tc use Arrhenius
    ramptime_ARR_cooling = (Tc-Tref)/qc;
    deltat_ARR_cooling = 0.1;
    time_ARR_cooling                                                    =
deltat_ARR_cooling:deltat_ARR_cooling:ramptime_ARR_cooling;
    for i=1:numel(time_ARR_cooling)
        T_ARR_cooling(i) = Tref+qc*time_ARR_cooling(i);
        at_ARR_cooling(i)       =       exp((-ARR).*(1./(273.15       +
T_ARR_cooling(i))-1./(Tref + 273.15)));
        for j=1:NT
            dttau_ARR_cooling_matrix(i,j)                               =
deltat_ARR_cooling./at_ARR_cooling(i)./tauvec(j);
        end
    end
    for j=1:NT
        int_tau_ARR_cooling(j) = sum(dttau_ARR_cooling_matrix(:,j));
        ee_ARR_cooling(j)          =          ee_WLF_cooling(j).*exp(-
int_tau_ARR_cooling(j));
        stress_ARR_cooling(j) = Evec(j).*ee_ARR_cooling(j);
    end
else % Tref<=Th and we use Arrhenius from the very start
    ramptime_ARR_cooling = (Tc-Th)/qc;
    deltat_ARR_cooling = 0.1;
    time_ARR_cooling                                                    =
deltat_ARR_cooling:deltat_ARR_cooling:ramptime_ARR_cooling;
    for i=1:numel(time_ARR_cooling)
        T_ARR_cooling(i) = Th+qc*time_ARR_cooling(i);
        at_ARR_cooling(i)       =       exp((-ARR).*(1./(273.15       +
T_ARR_cooling(i))-1./(Tref + 273.15)));
        for j=1:NT
            dttau_ARR_cooling_matrix(i,j)                               =
deltat_ARR_cooling./at_ARR_cooling(i)./tauvec(j);
        end
    end
    for j=1:NT
        int_tau_ARR_cooling(j) = sum(dttau_ARR_cooling_matrix(:,j));
```

```
        ee_ARR_cooling(j)            =            ee_holding(j).*exp(-
int_tau_ARR_cooling(j));
        stress_ARR_cooling(j) = Evec(j).*ee_ARR_cooling(j);
    end
end
% once the temperature is reached it is kept isothermal for 60 min
for j=1:NT
ee_isothermal_cooling(j)           =           ee_ARR_cooling(j).*exp(-
tc./tauvec(j)./at_ARR_cooling(end));
stress_isothermal_cooling(j) = Evec(j).*ee_isothermal_cooling(j);
end
stress_EndOfCooling = E0.*emax + sum(stress_isothermal_cooling);
%% ==UNLOADING==
% the unloading is istantaneous therefore right after unloading only the
% elastic contrinbutions are to be considered
% each elastic strain decreases by a small quantity de
% the total stress is zero so E0*(emax-de) + sum Ei*(eei_cool-de) = 0
% so de is the total stress before unloading divided by E0+sumEi which
is the glassy plateau
de = stress_EndOfCooling/(E0+sum(Evec));
for j=1:NT
    ee_recovery_zero(j) = ee_isothermal_cooling(j) - de;
    stress_recovery_zero(j) = Evec(j).*ee_recovery_zero(j);
end
%% write vector for initial value ODE system solution
ee0 = ee_recovery_zero;
stress_distribution = ee0.*Evec;
Rf = (emax-de)/emax;
%% histograms
%% end ~continue by script Eigenalgebra or ODE45~
```

ODEFunNT

This is the function for the system of differential equations.

```
function deedt = ODE_funNT(t,ee)
% main reference for model https://doi.org/10.1038/ncomms4066
%            reference            for            ODE            Matlab
https://uk.mathworks.com/help/matlab/ref/ode45.html
%% ODE system
%
% for the homogeneous system
%           d/dt[ee] = -1/alphaT [A] [ee]
% the general ith equation for this system looks like
%                                    T_N
%           dee(ith)/dt = -1/alphaT * SUM A(i,j)ee(jth)
%                                    j=1
% T_N = total number of non-equilibrium branches
% the function should be handled to a ODE solver like ode15s
% n.e. branches
NT = 14;
%% Choose recovery temperature
Trec = 40;
assignin('base','Trec',Trec);
%% load parameters-file.mat
load YuetAl_tempRamp_DATA_OPTIMISED_14.mat
para=para(:);
ARR = para(4);
WLF1 = para(2);
WLF2 = para(3);
Tref = para(1);
Eeq = para(5);
Evec = para(6:5+NT);
tauvec = para(6+NT:end);
```

```
Etot = Eeq + sum(Evec);
%% BUILD MATRIX E
Evector = Evec;
Ematrix = zeros(NT); % preassign dimension
for j=1:NT
    Ematrix(1:NT,j) = Evector(j)./Eeq;
end
Ematrix = Ematrix + eye(NT);
%% BUILD MATRIX T
tauREFvector = tauvec;
Tmatrix = zeros(NT);
for j=1:NT
    Tmatrix(j,j) = 1./tauREFvector(j);
end
%% BUILD MATRIX A
Amatrix = inv(Ematrix)*Tmatrix;
%% COMPUTE alphaT
if Trec >= Tref
        alphaT = 10.^((-WLF1).*(Trec-Tref)./(WLF2+Trec-Tref)); % WLF
    else
        alphaT  =  exp((-ARR).*(1./(273.15+Trec)-1./(Tref+273.15)));  %
Arrhenius
end
deedt = (-1/alphaT)*Amatrix*ee;
% assignin('base','deedt',deedt)
end
```

SolveStrainNT_ODE

This script solves the strain evolution during recovery by use of the ODE function, which gets handled the previous function. It also outputs some figures and documents on the results.

```
% solve the free recovery evolution by using ODE15s
% close all
clearvars -except para ee0 stress_distribution Rf emax de
NT = 14;
TotTime = 8e9; % seconds
[t,ee] = ode15s(@ODE_funNT,[0 TotTime],ee0);
%                                          T_N
%           total_strain = - SUM(E(i)*ee(i)/Eeq)
%                                          i=1
para=para(:);
E0 = para(5);
E_vec = para(6:5+NT);
strain = zeros(size(t));
for q=1:numel(t)
   strain(q) = -(ee(q,:)*E_vec/E0);
end
time_min = t./60;
tdays = time_min./60./24;
Rr = 1 - strain/(emax-de);
non_equi_stresses = ee.*transpose(E_vec);
equi_stress = E0.*strain;
total_stress  =  equi_stress  +  non_equi_stresses*ones(NT,1);  %  should
obscillate around 0
eev = -ee + strain; % viscous strains evolution
% close all;
%% Plot
% Figtitle = ['(a) Trec = ',num2str(Trec),' °C'];
Figtitle = '';
figure1 = figure('Position', get(0, 'Screensize'));
```

```
axes1 = axes('Parent',figure1);
hold(axes1,'on');
yyaxis(axes1,'left');
semilogx(time_min,Rr,'DisplayName','Recovery ratio','LineWidth',1.5,...
    'Color',[0 0 0]);
ylabel('Recovery ratio','FontSize',22);
ylim([-0.1 1.1])
set(axes1,'YColor',[0 0 0]);
yyaxis(axes1,'right');
semilogx(time_min,equi_stress,'DisplayName','Stress                branch
0','LineWidth',1.5,...
    'Color',[1 0 0]);
% FigRR = figure('Position', get(0, 'Screensize'));
% set(FigRR,'defaultAxesColorOrder',[[0 0 0]; [0 0 0]]);
% semilogx(time_min,Rr,'k-','linewidth',1.5) % RECOVERY
% xlim([time_min(1) time_min(end)]);
% xlabel('Recovery time (min)','FontSize',16)
% ylabel('Recovery ratio','FontSize',16)
% title(['Recovery Prediction at ',num2str(Trec),' °C'],'FontSize',16)
% hold on
% yyaxis right
% semilogx(time_min,equi_stress,'b-','linewidth',1.5) % EQUI B STRESS
markers = {'p','o','*','.','h','v','>','^','s','d','<','+','x','o'};
for i=1:NT
    semilogx(time_min(1:5:end),non_equi_stresses(1:5:end,i),['r--
',markers{i}],'Markersize',10,'linewidth',1.5) % N EQUI B STRESS
end
ylabel('Stress (MPa)','FontSize',16)
ylim([min(min(non_equi_stresses)).*1.25, max(equi_stress).*1.25])
for ii=1:NT+2
    legends(ii) = {['Stress branch ',num2str(ii-2)]};
end
legends(1) = {'Recovery ratio'};
legends(2) = {'Stress branch 0'};
% legend(legends,'location','bestoutside','FontSize',16);
% saveas(FigRR, 'RR_STRESS_vsTIME.png','png');
% Create ylabel
ylabel('Stress (MPa)','FontSize',22);
% Set the remaining axes properties
set(axes1,'YColor',[1 0 0]);
% Create xlabel
xlabel('Recovery time (min)','FontSize',22);
% Create title
title(Figtitle,'FontSize',18);
% Uncomment the following line to preserve the X-limits of the axes
xlim(axes1,[0 133333333.333333]);
box(axes1,'on');
% Set the remaining axes properties
set(axes1,'FontSize',18,'LineWidth',1.5,'XMinorTick','on','XScale','lo
g');
% Create legend
% legend1 = legend(axes1,'show');
% set(legend1,'Location','bestoutside','FontSize',18);
legend(legends,'location','bestoutside','FontSize',18);
% text(0.01,0.9,'(a)','FontSize',16,'Units','normalized')
saveas(figure1,'RR_STRESS_vsTIME.png','png');
%% Some noticable recovery %
idx20=find(Rr>0.19,1,'first');
rec20_minutes=t(idx20)/60 %#ok<NOPTS>
rec20_hours=t(idx20)/60/60 %#ok<NOPTS>
rec20_days=t(idx20)/60/60/24 %#ok<NOPTS>
idx90=find(Rr>0.89,1,'first');
rec90_minutes=t(idx90)/60 %#ok<NOPTS>
rec90_hours=t(idx90)/60/60 %#ok<NOPTS>
```

```
rec90_days=t(idx90)/60/60/24 %#ok<NOPTS>
%% Others
% Min stresses time
% for iii=1:NT
%                 [stresses_min_values(iii)   stresses_min_idx(iii)]   =
min(non_equi_stresses(:,iii));
%     stresses_min_time_min(iii) = time_min(stresses_min_idx(iii));
% end
% Normalised stresses
% for i=1:NT
%                                                 norm_stress(:,i)        =
non_equi_stresses(:,i)./min(non_equi_stresses(:,i));
% end
% print('Rr vs time','-dpng');
```

EigenAnalysisNT

This script uses eigen analysis to solve the system of differential equations.

```
%% Use eigen analysis to solve system of ODE
%% Needs paramaters, file.mat named para required to be in the workspace
% close all
clearvars -except ee0 para de
NT = 14;
para=para(:);
ee0=ee0(:);
emax = 0.1;
Trec = 40;
%% data
Tref = para(1);
WLF1 = para(2);
WLF2 = para(3);
ARR = para(4);
E0 = para(5);
Evec = para(6:5+NT);
tauvec = para(6+NT:end);
Etot = E0 + sum(Evec);
%% Shifting factor at Trec
if Trec >= Tref
        at = 10.^((-WLF1).*(Trec-Tref)./(WLF2+Trec-Tref)); % WLF
    else
        at   =   exp((-ARR).*(1./(273.15+Trec)-1./(Tref+273.15)));   %
Arrhenius
end
% BUILD MATRIX E
Evector = transpose(Evec);
Ematrix = zeros(NT);
for j=1:NT
    Ematrix(1:NT,j) = Evector(j)./E0;
end
Ematrix = Ematrix + eye(NT);
% BUILD MATRIX T
tauREFvector = transpose(tauvec);
Tmatrix = zeros(NT);
for j=1:NT
    Tmatrix(j,j) = 1./tauREFvector(j);
end
% BUILD MATRIX A
Amatrix = (inv(Ematrix))*Tmatrix;
Amatrix = -Amatrix./at;
[Qmatrix,Dmatrix] = eig(Amatrix);
eigenvalues = eig(Amatrix);
%% IMPORTANT load ee0 or have it in the workspace already
% load intitialcondition.mat
```

```
%% Find constants
const = (inv(Qmatrix))*(ee0);
%% Find solution points
time=0:1:3600; % consider logspacing the values for large time scale
(allocated memory is not much)
for i=1:numel(time)
    expvec = exp(eigenvalues.*time(i));
    Cexpvec = const.*expvec;
    ee_matrix(:,i) = Qmatrix*Cexpvec;
end
for i=1:numel(time)
    strain(i)= -(Evector*ee_matrix(:,i))/E0;
end
% recovery ratio
Rr = 1-strain./(emax-de);
% plot
time_min = time./60;
time_hours = time./60./60;
time_days = time./60./60./24;
% reduce number of data point to plot to avoid memory usage
take_every = 60; % elements
time_min_less = time_min(1:take_every:end);
Rr_less = Rr(1:take_every:end);
figure(10)
semilogx(time_min_less,Rr_less)
xlabel('time (min)')
ylabel('Rr, recovery ratio')
% end
```

Appendix B: Supplementary data

Table S.1 Elastic moduli obtained for the fittings reported in paragraph 8.3

Specimen	Elastic modulus in non-equilibrium branches 1-7 [MPa]						
#004	18.447	21.748	30.558	63.418	78.723	14.979	74.221
#006b	14.328	17.663	24.185	48.187	66.024	5.252	56.135
#007	24.134	28.029	39.719	77.894	100.582	7.760	83.332
#008	18.619	23.154	30.257	61.635	78.808	12.801	66.040
#010b	30.362	32.235	45.541	105.158	187.906	12.305	139.771
#028	36.424	34.224	48.049	131.452	240.497	2.337	164.163
#029	22.771	24.176	34.155	78.867	140.926	9.228	104.826
#029b	35.923	33.896	49.781	128.236	304.257	14.199	200.480

Specimen	Elastic modulus in non-equilibrium branches 8-14 [MPa]						
#004	109.574	320.902	638.657	185.760	25.765	2.285	1.092
#006b	75.889	249.367	522.160	161.995	19.328	1.780	0.848
#007	102.919	351.339	743.824	244.346	32.051	2.681	1.141
#008	82.466	276.397	545.177	200.291	27.264	2.439	0.869
#010b	185.069	430.325	575.548	187.275	23.297	2.207	0.946
#028	182.272	531.205	349.949	172.687	19.461	1.647	0.537
#029	138.799	322.737	431.652	140.453	17.473	1.655	0.709
#029b	245.297	354.177	315.493	96.783	10.546	1.236	0.495

References

[1] P. T. Mather, X. Luo, and I. A. Rousseau, "Shape Memory Polymer Research" *Annu. Rev. Mater. Res.*, vol. 39, no. 1, pp. 445–471, 2009.

[2] C. Liu, H. Qin, and P. T. Mather, "Review of progress in shape-memory polymers" *J. Mater. Chem.*, vol. 17, no. 16, pp. 1543–1558, 2007.

[3] A. Lendlein and S. Kelch, "Shape-Memory Polymers" *Angew. Chemie Int. Ed.*, vol. 41, no. 12, p. 2034, Jun. 2002.

[4] C. W. Hull, "Apparatus for production of three-dimensional objects by stereolithography" *US Pat. 4575330*, pp. 1–12, 1986.

[5] Y. Y. C. Choong, S. Maleksaeedi, H. Eng, J. Wei, and P. C. Su, "4D printing of high performance shape memory polymer using stereolithography" *Mater. Des.*, vol. 126, no. April, pp. 219–225, 2017.

[6] Q. Ge, A. H. Sakhaei, H. Lee, C. K. Dunn, N. X. Fang, and M. L. Dunn, "Multimaterial 4D Printing with Tailorable Shape Memory Polymers" *Sci. Rep.*, vol. 6, no. 1, p. 31110, Nov. 2016.

[7] S. Miao, W. Zhu, N. J. Castro, M. Nowicki, X. Zhou, H. Cui, J. P. Fisher, and L. G. Zhang, "4D printing smart biomedical scaffolds with novel soybean oil epoxidized acrylate" *Sci. Rep.*, vol. 6, no. 1, p. 27226, Jul. 2016.

[8] K. Yu, Q. Ge, and H. J. Qi, "Reduced time as a unified parameter determining fixity and free recovery of shape memory polymers" *Nat. Commun.*, vol. 5, p. 3066, 2014.

[9] J. D. Ferry, *Viscoelastic Properties of Polymers*, vol. 81, no. 12. 1980.

[10] H. F. Brinson and L. C. Brinson, *Polymer Engineering Science and Viscoelasticity*. Boston, MA: Springer US, 2015.

[11] M. Rubinstein and R. Colby, *Polymer Physics*. Oxford: Oxford Univerity Press, 2003.

[12] K. Yu, T. Xie, J. Leng, Y. Ding, and H. J. Qi, "Mechanisms of multi-shape memory effects and associated energy release in shape memory polymers" *Soft Matter*, vol. 8, no. 20, pp. 5687–5695, 2012.

[13] K. Yu and H. J. Qi, "Temperature memory effect in amorphous shape memory polymers" *Soft Matter*, vol. 10, no. 47, pp. 9423–32, 2014.

[14] D. Roylance, "Engineering viscoelasticity" 2001.

[15] Y. Liu, K. Gall, M. L. Dunn, A. R. Greenberg, and J. Diani, "Thermomechanics of shape memory polymers: Uniaxial experiments and constitutive modeling" *Int. J.*

Plast., vol. 22, no. 2, pp. 279–313, 2006.

[16] C. M. Yakacki, K. Gall, R. Shandas, A. M. Ortega, N. Willett, and A. R. Greenberg, "Optimizing the Thermomechanics of Shape-Memory Polymers for Biomedical Applications" *MRS Proc.*, vol. 855, p. W3.27, Feb. 2004.

[17] K. K. Westbrook, P. H. Kao, F. Castro, Y. Ding, and H. Jerry Qi, "A 3D finite deformation constitutive model for amorphous shape memory polymers: A multi-branch modeling approach for nonequilibrium relaxation processes" *Mech. Mater.*, vol. 43, no. 12, pp. 853–869, 2011.

[18] K. Otsuka and C. M. Wayman, Eds., *Shape memory materials*. Cambridge: CUP, 1998.

[19] L. Petrini and F. Migliavacca, "Biomedical Applications of Shape Memory Alloys" *J. Metall.*, vol. 2011, pp. 1–15, 2011.

[20] A. Lendlein, "Biodegradable, Elastic Shape-Memory Polymers for Potential Biomedical Applications" *Science (80-.).*, vol. 296, no. 5573, pp. 1673–1676, May 2002.

[21] C. M. Yakacki, R. Shandas, D. Safranski, A. M. Ortega, K. Sassaman, and K. Gall, "Strong, tailored, biocompatible shape-memory polymer networks" *Adv. Funct. Mater.*, vol. 18, no. 16, pp. 2428–2435, 2008.

[22] G. I. Peterson, A. V. Dobrynin, and M. L. Becker, "Biodegradable Shape Memory Polymers in Medicine" *Adv. Healthc. Mater.*, vol. 6, no. 21, pp. 1–16, 2017.

[23] J. Karger-Kocsis and S. Kéki, "Biodegradable polyester-based shape memory polymers: Concepts of (supra)molecular architecturing" *Express Polym. Lett.*, vol. 8, no. 6, pp. 397–412, 2014.

[24] W. Sokolowski, A. Metcalfe, S. Hayashi, L. Yahia, and J. Raymond, "Medical applications of shape memory polymers" *Biomed. Mater.*, vol. 2, no. 1, pp. S23–7, 2007.

[25] T. Matsuda, M. Mizutani, and S. C. Arnold, "Molecular design of photocurable liquid biodegradable copolymers. 1. Synthesis and photocuring characteristics" *Macromolecules*, vol. 33, no. 3, pp. 795–800, 2000.

[26] W. Voit, T. Ware, R. R. Dasari, P. Smith, L. Danz, D. Simon, S. Barlow, S. R. Marder, and K. Gall, "High-strain shape-memory polymers" *Adv. Funct. Mater.*, vol. 20, no. 1, pp. 162–171, 2010.

[27] L. Xue, S. Dai, and Z. Li, "Synthesis and characterization of elastic star shape-memory polymers as self-expandable drug-eluting stents" *J. Mater. Chem.*, vol. 22, no. 15, pp. 7403–7411, 2012.

[28] P. Miaudet, A. Derre, M. Maugey, C. Zakri, P. M. Piccione, R. Inoubli, and P. Poulin, “Shape and Temperature Memory of Nanocomposites with Broadened Glass Transition” *Science (80-.).*, vol. 318, no. 5854, pp. 1294–1296, Nov. 2007.

[29] A. Li, J. Fan, and G. Li, “Recyclable thermoset shape memory polymers with high stress and energy output: Via facile UV-curing” *J. Mater. Chem. A*, vol. 6, no. 24, pp. 11479–11487, 2018.

[30] K. Gall, M. Mikulas, N. A. Munshi, F. Beavers, and M. Tupper, “Carbon fiber reinforced shape memory polymer composites” *J. Intell. Mater. Syst. Struct.*, vol. 11, no. 11, pp. 877–886, 2000.

[31] M. Montgomery, S. Ahadian, L. Davenport Huyer, M. Lo Rito, R. A. Civitarese, R. D. Vanderlaan, J. Wu, L. A. Reis, A. Momen, S. Akbari, A. Pahnke, R. K. Li, C. A. Caldarone, and M. Radisic, “Flexible shape-memory scaffold for minimally invasive delivery of functional tissues” *Nat. Mater.*, vol. 16, no. 10, pp. 1038–1046, 2017.

[32] K. Kratz, U. Voigt, and A. Lendlein, “Temperature-memory effect of copolyesterurethanes and their application potential in minimally invasive medical technologies” *Adv. Funct. Mater.*, vol. 22, no. 14, pp. 3057–3065, 2012.

[33] S. A. Bencherif, R. W. Sands, D. Bhatta, P. Arany, C. S. Verbeke, D. A. Edwards, and D. J. Mooney, “Injectable preformed scaffolds with shape-memory properties” *Proc. Natl. Acad. Sci.*, vol. 109, no. 48, pp. 19590–19595, 2012.

[34] H. M. Wache, D. J. Tartakowska, A. Hentrich, and M. H. Wagner, “Development of a polymer stent with shape memory effect as a drug delivery system” *J. Mater. Sci. Mater. Med.*, vol. 14, no. 2, pp. 109–112, 2003.

[35] W. Small IV, T. S. Wilson, W. J. Benett, J. M. Loge, and D. J. Maitland, “Laser-activated shape memory polymer intravascular thrombectomy device” *Opt. Express*, vol. 13, no. 20, p. 8204, 2005.

[36] T. S. Wilson, W. Small IV, W. J. Benett, J. P. Bearinger, and D. J. Maitland, “Shape memory polymer therapeutic devices for stroke” in *Smart Medical and Biomedical Sensor Technology III*, 2005, vol. 6007.

[37] V. C. Sonawane, M. P. More, A. P. Pandey, P. O. Patil, and P. K. Deshmukh, “Fabrication and characterization of shape memory polymers based bioabsorbable biomedical drug eluting stent” *Artif. Cells, Nanomedicine Biotechnol.*, vol. 45, no. 8, pp. 1740–1750, 2017.

[38] G. Li, G. Fei, H. Xia, J. Han, and Y. Zhao, “Spatial and temporal control of shape memory polymers and simultaneous drug release using high intensity focused

ultrasound” *J. Mater. Chem.*, vol. 22, no. 16, pp. 7692–7696, 2012.

[39] C. Wischke, M. Behl, and A. Lendlein, “Drug-releasing shape-memory polymers – the role of morphology, processing effects, and matrix degradation” *Expert Opin. Drug Deliv.*, vol. 10, no. 9, pp. 1193–1205, Sep. 2013.

[40] M. Behl and A. Lendlein, “Shape-memory polymers” *Mater. Today*, vol. 10, no. 4, pp. 20–28, 2007.

[41] A. Lendlein and T. Sauter, “Shape-Memory Effect in Polymers” *Macromol. Chem. Phys.*, vol. 214, no. 11, pp. 1175–1177, 2013.

[42] J. Hu, Y. Zhu, H. Huang, and J. Lu, “Recent advances in shape-memory polymers: Structure, mechanism, functionality, modeling and applications” *Prog. Polym. Sci.*, vol. 37, no. 12, pp. 1720–1763, 2012.

[43] T. Xie, “Recent advances in polymer shape memory” *Polymer* ., vol. 52, no. 22, pp. 4985–5000, Oct. 2011.

[44] J. Leng, X. Lan, Y. Liu, and S. Du, “Shape-memory polymers and their composites: Stimulus methods and applications” *Prog. Mater. Sci.*, vol. 56, no. 7, pp. 1077–1135, 2011.

[45] H. Meng and G. Li, “A review of stimuli-responsive shape memory polymer composites” *Polymer* ., vol. 54, no. 9, pp. 2199–2221, 2013.

[46] Y. Liu, J. K. Boyles, J. Genzer, and M. D. Dickey, “Self-folding of polymer sheets using local light absorption” *Soft Matter*, vol. 8, no. 6, pp. 1764–1769, 2012.

[47] D. J. Maitland, M. F. Metzger, D. Schumann, A. Lee, and T. S. Wilson, “Photothermal properties of shape memory polymer micro-actuators for treating stroke” *Lasers Surg. Med.*, vol. 30, no. 1, pp. 1–11, 2002.

[48] J. Leng, X. Wu, and Y. Liu, “Infrared light-active shape memory polymer filled with nanocarbon particles” *J. Appl. Polym. Sci.*, vol. 114, no. 4, pp. 2455–2460, Nov. 2009.

[49] Y. Liu, H. Lv, X. Lan, J. Leng, and S. Du, “Review of electro-active shape-memory polymer composite” *Compos. Sci. Technol.*, vol. 69, no. 13, pp. 2064–2068, 2009.

[50] M. Sabzi, M. Babaahmadi, N. Samadi, G. R. Mahdavinia, M. Keramati, and N. Nikfarjam, “Graphene network enabled high speed electrical actuation of shape memory nanocomposite based on poly(vinyl acetate)” *Polym. Int.*, vol. 66, no. 5, pp. 665–671, 2017.

[51] X. Luo and P. T. Mather, “Conductive shape memory nanocomposites for high speed electrical actuation” *Soft Matter*, vol. 6, no. 10, pp. 2146–2149, 2010.

[52] R. Mohr, K. Kratz, T. Weigel, M. Lucka-Gabor, M. Moneke, and A. Lendlein,

"Initiation of shape-memory effect by inductive heating of magnetic nanoparticles in thermoplastic polymers" *Proc. Natl. Acad. Sci.*, vol. 103, no. 10, pp. 3540–3545, 2006.

[53] X. Zheng, S. Zhou, Y. Xiao, X. Yu, X. Li, and P. Wu, "Shape memory effect of poly(d,l-lactide)/Fe3O4 nanocomposites by inductive heating of magnetite particles" *Colloids Surfaces B Biointerfaces*, vol. 71, no. 1, pp. 67–72, 2009.

[54] W. M. Huang, B. Yang, L. An, C. Li, and Y. S. Chan, "Water-driven programmable polyurethane shape memory polymer: Demonstration and mechanism" *Appl. Phys. Lett.*, vol. 86, no. 11, pp. 1–3, 2005.

[55] B. Yang, W. M. Huang, C. Li, and L. Li, "Effects of moisture on the thermomechanical properties of a polyurethane shape memory polymer" *Polymer* ., vol. 47, no. 4, pp. 1348–1356, 2006.

[56] S. Chen, J. Hu, and H. Zhuo, "Study on the moisture absorption of pyridine containing polyurethane for moisture-responsive shape memory effects" *J. Mater. Sci.*, vol. 46, no. 20, pp. 6581–6588, 2011.

[57] H. Lv, J. Leng, Y. Liu, and S. Du, "Shape-memory polymer in response to solution" *Adv. Eng. Mater.*, vol. 10, no. 6, pp. 592–595, 2008.

[58] H. Du and J. Zhang, "Solvent induced shape recovery of shape memory polymer based on chemically cross-linked poly(vinyl alcohol)" *Soft Matter*, vol. 6, no. 14, pp. 3370–3376, 2010.

[59] Y. Li, H. Chen, D. Liu, W. Wang, Y. Liu, and S. Zhou, "PH-Responsive Shape Memory Poly(ethylene glycol)-Poly(ε-caprolactone)-based Polyurethane/Cellulose Nanocrystals Nanocomposite" *ACS Appl. Mater. Interfaces*, vol. 7, no. 23, pp. 12988–12999, 2015.

[60] X. Han, Z. Dong, M. Fan, Y. Liu, J.-H. Li, Y. Wang, Q. Yuan, B. Li, and S. Zhang, "pH-Induced Shape-Memory Polymers" *Macromol. Rapid Commun.*, vol. 33, no. 12, pp. 1055–1060, Jun. 2012.

[61] Z. Q. Dong, Y. Cao, Q. J. Yuan, Y. F. Wang, J. H. Li, B. J. Li, and S. Zhang, "Redox- and glucose-induced shape-memory polymers" *Macromol. Rapid Commun.*, vol. 34, no. 10, pp. 867–872, 2013.

[62] L. Liu, N. Wang, Y. Han, Y. Li, and W. Liu, "Redox-triggered self-rolling robust hydrogel tubes for cell encapsulation" *Macromol. Rapid Commun.*, vol. 35, no. 3, pp. 344–349, 2014.

[63] J. Leng, H. Lu, Y. Liu, W. M. Huang, and S. Du, "Shape-Memory Polymers—A Class of Novel Smart Materials" *MRS Bull.*, vol. 34, no. 11, pp. 848–855, 2009.

[64] I. A. Rousseau, “Challenges of shape memory polymers: A review of the progress toward overcoming SMP’s limitations” *Polym. Eng. Sci.*, vol. 48, no. 11, pp. 2075–2089, Nov. 2008.

[65] A. A. Sharp, H. V. Panchawagh, A. Ortega, R. Artale, S. Richardson-Burns, D. S. Finch, K. Gall, R. L. Mahajan, and D. Restrepo, “Toward a self-deploying shape memory polymer neuronal electrode” *J. Neural Eng.*, vol. 3, no. 4, 2006.

[66] J. H. Park, H. Kim, J. R. Youn, and Y. S. Song, “Strategic design and fabrication of acrylic shape memory polymers” *Smart Mater. Struct.*, vol. 26, no. 8, p. 085026, Aug. 2017.

[67] C. M. Yakacki, R. Shandas, C. Lanning, B. Rech, A. Eckstein, and K. Gall, “Unconstrained recovery characterization of shape-memory polymer networks for cardiovascular applications” *Biomaterials*, vol. 28, no. 14, pp. 2255–2263, 2007.

[68] A. M. Ortega, S. E. Kasprzak, C. M. Yakacki, J. Diani, A. R. Greenberg, and K. Gall, “Structure-property relationships in photopolymerizable polymer networks: Effect of composition on the crosslinked structure and resulting thermomechanical properties of a (meth)acrylate-based system” *J. Appl. Polym. Sci.*, vol. 110, no. 3, pp. 1559–1572, Nov. 2008.

[69] D. L. Safranski and K. Gall, “Effect of chemical structure and crosslinking density on the thermo-mechanical properties and toughness of (meth)acrylate shape memory polymer networks” *Polymer* ., vol. 49, no. 20, pp. 4446–4455, 2008.

[70] K. Gall, C. M. Yakacki, Y. Liu, R. Shandas, N. Willett, and K. S. Anseth, “Thermomechanics of the shape memory effect in polymers for biomedical applications” *J. Biomed. Mater. Res. - Part A*, vol. 73, no. 3, pp. 339–348, 2005.

[71] X. Li, Y. Pan, J. Lai, R. Wu, Z. Zheng, and X. Ding, “Design of well-defined shape memory networks with high homogeneity: Towards advanced shape memory polymeric materials” *Polym. Chem.*, vol. 8, no. 26, pp. 3867–3873, 2017.

[72] T. Javanbakht and W. Sokolowski, *Thiol-ene/acrylate systems for biomedical shape-memory polymers*, no. 2001. Elsevier Ltd., 2015.

[73] D. P. Nair, N. B. Cramer, T. F. Scott, C. N. Bowman, and R. Shandas, “Photopolymerized thiol-ene systems as shape memory polymers” *Polymer* ., vol. 51, no. 19, pp. 4383–4389, Sep. 2010.

[74] C. E. Hoyle and C. N. Bowman, “Thiol-ene click chemistry” *Angew. Chemie - Int. Ed.*, vol. 49, no. 9, pp. 1540–1573, 2010.

[75] T. Xie and I. A. Rousseau, “Facile tailoring of thermal transition temperatures of epoxy shape memory polymers” *Polymer* ., vol. 50, no. 8, pp. 1852–1856, 2009.

[76] A. Alteheld, Y. Feng, S. Kelch, and A. Lendlein, “Biodegradable, amorphous copolyester-urethane networks having shape-memory properties” *Angew. Chemie - Int. Ed.*, vol. 44, no. 8, pp. 1188–1192, 2005.

[77] C. P. Buckley, C. Prisacariu, and A. Caraculacu, “Novel triol-crosslinked polyurethanes and their thermorheological characterization as shape-memory materials” *Polymer* ., vol. 48, no. 5, pp. 1388–1396, 2007.

[78] P. Singhal, W. Small, E. Cosgriff-Hernandez, D. J. Maitland, and T. S. Wilson, “Low density biodegradable shape memory polyurethane foams for embolic biomedical applications” *Acta Biomater.*, vol. 10, no. 1, pp. 67–76, 2014.

[79] N. Y. Choi and A. Lendlein, “Degradable shape-memory polymer networks from oligo[(l-lactide)-ran- glycolide]dimethacrylates” *Soft Matter*, vol. 3, no. 7, pp. 901–909, 2007.

[80] G. Zhu, G. Liang, Q. Xu, and Q. Yu, “Shape-memory effects of radiation crosslinked Poly(ε-caprolactone)” *J. Appl. Polym. Sci.*, vol. 90, no. 6, pp. 1589–1595, 2003.

[81] A. Lendlein, “AB-polymer networks based on oligo(ε-caprolactone) segments showing shape-memory properties” *Proc. Natl. Acad. Sci.*, vol. 98, no. 3, pp. 842–847, Jan. 2001.

[82] R. M. Baker, J. H. Henderson, and P. T. Mather, “Shape memory poly(ε-caprolactone)-co-poly(ethylene glycol) foams with body temperature triggering and two-way actuation” *J. Mater. Chem. B*, vol. 1, no. 38, pp. 4916–4920, 2013.

[83] J. Hu, Z. Yang, L. Yeung, F. Ji, and Y. Liu, “Crosslinked polyurethanes with shape memory properties” *Polym. Int.*, vol. 54, no. 5, pp. 854–859, 2005.

[84] N. Zheng, Z. Fang, W. Zou, Q. Zhao, and T. Xie, “Thermoset Shape-Memory Polyurethane with Intrinsic Plasticity Enabled by Transcarbamoylation” *Angew. Chemie - Int. Ed.*, vol. 55, no. 38, pp. 11421–11425, 2016.

[85] M. Li, Q. Guan, and T. J. Dingemans, “High-Temperature Shape Memory Behavior of Semicrystalline Polyamide Thermosets” *ACS Appl. Mater. Interfaces*, vol. 10, no. 22, pp. 19106–19115, 2018.

[86] T. Chung, A. Romo-Uribe, and P. T. Mather, “Two-way reversible shape memory in a semicrystalline network” *Macromolecules*, vol. 41, no. 1, pp. 184–192, 2008.

[87] C. Liu, S. B. Chun, P. T. Mather, L. Zheng, E. H. Haley, and E. B. Coughlin, “Chemically cross-linked polycyclooctene: Synthesis, characterization, and shape memory behavior” *Macromolecules*, vol. 35, no. 27, pp. 9868–9874, 2002.

[88] S. Bin Hong, S. J. Hong, T. H. Kang, J. H. Youk, and W. R. Yu, “Optical and shape

memory properties of semicrystalline poly(cyclooctene) upon cold-drawing" *J. Polym. Sci. Part B Polym. Phys.*, vol. 55, no. 21, pp. 1595–1607, 2017.

[89] H. M. Jeong, B. K. Ahn, and B. K. Kim, "Miscibility and shape memory effect of thermoplastic polyurethane blends with phenoxy resin" *Eur. Polym. J.*, vol. 37, no. 11, pp. 2245–2252, 2001.

[90] H. M. Jeong, J. H. Song, S. Y. Lee, and B. K. Kim, "Miscibility and shape memory property of poly(vinyl chloride)/thermoplastic polyurethane blends" *J. Mater. Sci.*, vol. 36, no. 22, pp. 5457–5463, 2001.

[91] J. W. Cho, Y. C. Jung, Y. C. Chung, and B. C. Chun, "Improved mechanical properties of shape-memory polyurethane block copolymers through the control of the soft-segment arrangement" *J. Appl. Polym. Sci.*, vol. 93, no. 5, pp. 2410–2415, 2004.

[92] H. M. Jeong, J. H. Song, K. W. Chi, I. Kim, and K. T. Kim, "Shape memory effect of poly(methylene-1,3-cyclopentane) and its copolymer with polyethylene" *Polym. Int.*, vol. 51, no. 4, pp. 275–280, 2002.

[93] C. Min, W. Cui, J. Bei, and S. Wang, "Biodegradable shape-memory polymer - Polylactide-co-poly(glycolide-co-caprolactone) multiblock copolymer" *Polym. Adv. Technol.*, vol. 16, no. 8, pp. 608–615, 2005.

[94] X. Luo, X. Zhang, M. Wang, D. Ma, M. Xu, and F. Li, "Thermally stimulated shape memory behavior of ethylene oxide ethylene terephthalate segmented copolymer" *J. Appl. Polym. Sci.*, vol. 64, no. 12, pp. 2433–2440, 1997.

[95] M. Wang, X. Luo, and D. Ma, "Dynamic mechanical behavior in the ethylene terephthalate-ethylene oxide copolymer with long soft segment as a shape memory material" *Eur. Polym. J.*, vol. 34, no. 1, pp. 1–5, Jan. 1998.

[96] B. K. Kim, S. Y. Lee, and M. Xu, "Polyurethanes having shape memory effects" *Polymer* ., vol. 37, no. 26, pp. 5781–5793, 1996.

[97] X. Ni and X. Sun, "Block copolymer of trans-polyisoprene and urethane segment: Shape memory effects" *J. Appl. Polym. Sci.*, vol. 100, no. 2, pp. 879–885, 2006.

[98] X. Sun and X. Ni, "Block copolymer of trans-polyisoprene and urethane segment: Crystallization behavior and morphology" *J. Appl. Polym. Sci.*, vol. 94, no. 6, pp. 2286–2294, 2004.

[99] A. Saralegi, E. Johan Foster, C. Weder, A. Eceiza, and M. A. Corcuera, "Thermoplastic shape-memory polyurethanes based on natural oils" *Smart Mater. Struct.*, vol. 23, no. 2, 2014.

[100] Z. S. Petrović, J. Milić, F. Zhang, and J. Ilavsky, "Fast-responding bio-based shape

memory thermoplastic polyurethanes" *Polymer .*, vol. 121, pp. 26–37, 2017.

[101] L. Sun and W. M. Huang, "Mechanisms of the multi-shape memory effect and temperature memory effect in shape memory polymers" *Soft Matter*, vol. 6, no. 18, pp. 4403–4406, 2010.

[102] J. Li, T. Liu, S. Xia, Y. Pan, Z. Zheng, X. Ding, and Y. Peng, "A versatile approach to achieve quintuple-shape memory effect by semi-interpenetrating polymer networks containing broadened glass transition and crystalline segments" *J. Mater. Chem.*, vol. 21, no. 33, pp. 12213–12217, 2011.

[103] S. Zhuo, G. Zhang, X. Feng, H. Jiang, J. Shi, H. Liu, and H. Li, "Multiple shape memory polymers for self-deployable device" *RSC Adv.*, vol. 6, no. 56, pp. 50581–50586, 2016.

[104] Q. Ge, X. Luo, C. B. Iversen, P. T. Mather, M. L. Dunn, and H. J. Qi, "Mechanisms of triple-shape polymeric composites due to dual thermal transitions" *Soft Matter*, vol. 9, no. 7, pp. 2212–2223, 2013.

[105] C. Samuel, S. Barrau, J. M. Lefebvre, J. M. Raquez, and P. Dubois, "Designing multiple-shape memory polymers with miscible polymer blends: Evidence and origins of a triple-shape memory effect for miscible PLLA/PMMA blends" *Macromolecules*, vol. 47, no. 19, pp. 6791–6803, 2014.

[106] J. E. Schroeppel, Edward A.; Spehr, Paul R.; Machek, "Implantable cardiac lead with multiple shape memory polymer structures" *US Pat. 5957966*, pp. 1–36, 1999.

[107] I. Bellin, S. Kelch, R. Langer, and A. Lendlein, "Polymeric triple-shape materials" *Proc. Natl. Acad. Sci.*, vol. 103, no. 48, pp. 18043–18047, 2006.

[108] T. Xie, X. Xiao, and Y. T. Cheng, "Revealing triple-shape memory effect by polymer bilayers" *Macromol. Rapid Commun.*, vol. 30, no. 21, pp. 1823–1827, 2009.

[109] T. Xie, "Tunable polymer multi-shape memory effect" *Nature*, vol. 464, no. 7286, pp. 267–270, 2010.

[110] T. Xie, K. A. Page, and S. A. Eastman, "Strain-based temperature memory effect for Nafion and its molecular origins" *Adv. Funct. Mater.*, vol. 21, no. 11, pp. 2057–2066, 2011.

[111] M. Behl, U. Ridder, Y. Feng, S. Kelch, and A. Lendlein, "Shape-memory capability of binary multiblock copolymer blends with hard and switching domains provided by different components" *Soft Matter*, vol. 5, no. 3, pp. 676–684, 2009.

[112] J. Cui, K. Kratz, and A. Lendlein, "Adjusting shape-memory properties of

amorphous polyether urethanes and radio-opaque composites thereof by variation of physical parameters during programming" *Smart Mater. Struct.*, vol. 19, no. 6, 2010.

[113] Y. Pan, X. Ding, Z. Zheng, Y. Wang, J. Li, Y. Peng, and X. Li, "Relation between temperature memory effect and multiple-shape memory behaviors based on polymer networks" *RSC Adv.*, vol. 4, no. 39, p. 20364, 2014.

[114] A. Biesiekierski, J. Wang, M. Abdel-Hady Gepreel, and C. Wen, "A new look at biomedical Ti-based shape memory alloys" *Acta Biomater.*, vol. 8, no. 5, pp. 1661–1669, 2012.

[115] D. J. Fernandes, R. V. Peres, A. M. Mendes, and C. N. Elias, "Understanding the Shape-Memory Alloys Used in Orthodontics" *ISRN Dent.*, vol. 2011, pp. 1–6, 2011.

[116] S. Ozan, J. Lin, Y. Li, R. Ipek, and C. Wen, "Development of Ti-Nb-Zr alloys with high elastic admissible strain for temporary orthopedic devices" *Acta Biomater.*, vol. 20, pp. 176–187, 2015.

[117] J. Indes and L. Gates, "New treatment of iliac artery disease: focus on the Absolute Pro® Vascular Self-Expanding Stent System" *Med. Devices Evid. Res.*, p. 147, 2013.

[118] D. R. Turner, C. Y. Owada, C. J. Sang, M. Khan, and D. S. Lim, "Closure of Secundum Atrial Septal Defects With the AMPLATZER Septal Occluder: A Prospective, Multicenter, Post-Approval Study" *Circ. Cardiovasc. Interv.*, vol. 10, no. 8, pp. 1–7, 2017.

[119] A. Lendlein and R. S. Langer, "Biodegradable Shape Memory Polymeric Sutures" vol. 2, no. 12, 2012.

[120] D. Zhang, O. J. George, K. M. Petersen, A. C. Jimenez-Vergara, M. S. Hahn, and M. A. Grunlan, "A bioactive 'self-fitting' shape memory polymer scaffold with potential to treat cranio-maxillo facial bone defects" *Acta Biomater.*, vol. 10, no. 11, pp. 4597–4605, 2014.

[121] "Shape memory medical Inc" [Online]. Available: https://www.shapemem.com/.

[122] W. et Al., "Shape memory polymer foams for endovascular therapies" *US Pat. 8133256 B2*, pp. 1–14, 2012.

[123] T. S. Wilson and J. P. Bearinger, "Shape memory polymers" *US Pat. 9051411 B2*, pp. 1–13, 2015.

[124] M. Rue, C. R. Roberts, and S. R. Slawson, "System for closure of a physical anomaly" *US Pat. 8882786 B2*, pp. 1–16, 2014.

[125] “CONMED” [Online]. Available: https://www.conmed.com/en.

[126] “FDA Premarket notification for ExoShape Duo Soft Tissue Fastener - 510 (k) Summary - K132783” *U.S. Food Drug Adm.*, 2013.

[127] “REMEDY^{TM} stent” [Online]. Available: https://www.kyoto-mp.co.jp/en/remedy.html.

[128] H. Tamai, K. Igaki, E. Kyo, and K. Kosuga, “Initial and 6-Month Results of Biodegradable Poly- l -Lactic” *Circulation*, vol. 102, pp. 399–404, 2000.

[129] L. Yahia, *Shape Memory Polymers for Biomedical Applications*. Elsevier, 2015.

[130] S. Nishio, K. Kosuga, K. Igaki, M. Okada, E. Kyo, T. Tsuji, E. Takeuchi, Y. Inuzuka, S. Takeda, T. Hata, Y. Takeuchi, Y. Kawada, T. Harita, J. Seki, S. Akamatsu, S. Hasegawa, N. Bruining, S. Brugaletta, S. De Winter, T. Muramatsu, Y. Onuma, P. W. Serruys, and S. Ikeguchi, “Long-term (>10 Years) clinical outcomes of first-in-human biodegradable poly-l-lactic acid coronary stents: Igaki-Tamai stents” *Circulation*, vol. 125, no. 19, pp. 2343–2352, 2012.

[131] H. J. Qi, T. D. Nguyen, F. Castro, C. M. Yakacki, and R. Shandas, “Finite deformation thermo-mechanical behavior of thermally induced shape memory polymers” *J. Mech. Phys. Solids*, vol. 56, no. 5, pp. 1730–1751, 2008.

[132] P. Gilormini and J. Diani, “On modeling shape memory polymers as thermoelastic two-phase composite materials” *Comptes Rendus - Mec.*, vol. 340, no. 4–5, pp. 338–348, 2012.

[133] Y. Li, J. Hu, and Z. Liu, “A constitutive model of shape memory polymers based on glass transition and the concept of frozen strain release rate” *Int. J. Solids Struct.*, vol. 124, pp. 252–263, 2017.

[134] H. Lu, X. Wang, Y. Yao, and Y. Q. Fu, “A ‘frozen volume’ transition model and working mechanism for the shape memory effect in amorphous polymers” *Smart Mater. Struct.*, vol. 27, no. 6, 2018.

[135] T. D. Nguyen, H. Jerry Qi, F. Castro, and K. N. Long, “A thermoviscoelastic model for amorphous shape memory polymers: Incorporating structural and stress relaxation” *J. Mech. Phys. Solids*, vol. 56, no. 9, pp. 2792–2814, 2008.

[136] J. Diani, P. Gilormini, C. Frédy, and I. Rousseau, “Predicting thermal shape memory of crosslinked polymer networks from linear viscoelasticity” *Int. J. Solids Struct.*, vol. 49, no. 5, pp. 793–799, 2012.

[137] C. Fang, J. Leng, H. Sun, and J. Gu, “A multi-branch thermoviscoelastic model based on fractional derivatives for free recovery behaviors of shape memory polymers” *Mech. Mater.*, vol. 120, no. October 2017, pp. 34–42, 2018.

[138] K. Yu, A. J. W. McClung, G. P. Tandon, J. W. Baur, and H. Jerry Qi, "A thermomechanical constitutive model for an epoxy based shape memory polymer and its parameter identifications" *Mech. Time-Dependent Mater.*, vol. 18, no. 2, pp. 453–474, 2014.

[139] Q. Ge, K. Yu, Y. Ding, and H. Jerry Qi, "Prediction of temperature-dependent free recovery behaviors of amorphous shape memory polymers" *Soft Matter*, vol. 8, no. 43, pp. 11098–11105, 2012.

[140] H. Tobushi, K. Okumura, S. Hayashi, and N. Ito, "Thermomechanical constitutive model of shape memory polymer" *Mech. Mater.*, vol. 33, no. 10, pp. 545–554, 2001.

[141] N. W. Tschoegl, *The Phenomenological Theory of Linear Viscoelastic Behavior: An Introduction*. Springer Science & Business Media, 2012.

[142] H. J. Q. Ming Lei, Kai Yu, Haibao Lu, M. Lei, K. Yu, H. Lu, and H. J. Qi, "Influence of structural relaxation on thermomechanical and shape memory performances of amorphous polymers" *Polymer .*, vol. 109, pp. 216–228, 2017.

[143] H. J. Qi, G. P. Tandon, A. J. W. McClung, H. Li, K. Yu, and J. W. Baur, "Cyclic behaviors of amorphous shape memory polymers" *Soft Matter*, vol. 12, no. 13, pp. 3234–3245, 2016.

[144] M. L. Williams, R. F. Landel, and J. D. Ferry, "The Temperature Dependence of Relaxation Mechanisms in Amorphous Polymers and Other Glass-forming Liquids" *J. Am. Chem. Soc.*, vol. 77, no. 14, pp. 3701–3707, 1955.

[145] G. Adam and J. H. Gibbs, "On the temperature dependence of cooperative relaxation properties in glass-forming liquids" *J. Chem. Phys.*, vol. 43, no. 1, pp. 139–146, 1965.

[146] E. A. Di Marzio and A. J. M. Yang, "Configurational entropy approach to the kinetics of glasses" *J. Res. Natl. Inst. Stand. Technol.*, vol. 102, no. 2, p. 135, 2012.

[147] P. A. O'Connell and G. B. McKenna, "Arrhenius-type temperature dependence of the segmental relaxation below Tg" *J. Chem. Phys.*, vol. 110, no. 22, pp. 11054–11060, 1999.

[148] I. Gibson, D. W. D. W. Rosen, and B. Stucker, *Additive Manufacturing Technologies: Rapid Prototyping to Direct Digital Manufacturing*, vol. 54. 2009.

[149] I. Gibson, P. J. Bartolo, and P. J. Bártolo, *Stereolithography*. Boston, MA: Springer US, 2011.

[150] P. F. Jacobs, "Rapid prototyping & manufacturing— Fundamentals of stereolithography" *J. Manuf. Syst.*, vol. 12, no. 5, pp. 430–433, 1993.

[151] F. P. W. Melchels, J. Feijen, and D. W. Grijpma, "A poly(d,l-lactide) resin for the preparation of tissue engineering scaffolds by stereolithography" *Biomaterials*, vol. 30, no. 23–24, pp. 3801–3809, 2009.

[152] J. Jansen, F. P. W. Melchels, D. W. Grijpma, and J. Feijen, "Fumaric Acid Monoethyl Ester-Functionalized Poly (D,L-lactide)/N-vinyl-2-pyrrolidone Resins for the Preparation of Tissue Engineering Scaffolds by Stereolithography" *Biomacromolecules*, vol. 10, no. 2, pp. 214–220, 2009.

[153] F. P. W. Melchels, K. Bertoldi, R. Gabbrielli, A. H. Velders, J. Feijen, and D. W. Grijpma, "Mathematically defined tissue engineering scaffold architectures prepared by stereolithography" *Biomaterials*, vol. 31, no. 27, pp. 6909–6916, 2010.

[154] L. Elomaa, S. Teixeira, R. Hakala, H. Korhonen, D. W. Grijpma, and J. V. Seppala, "Preparation of poly(e-caprolactone)-based tissue engineering scaffolds by stereolithography" *Acta Biomater.*, vol. 7, no. 11, pp. 3850–3856, 2011.

[155] B. J. Green, K. S. Worthington, J. R. Thompson, S. J. Bunn, M. Rethwisch, E. E. Kaalberg, C. Jiao, L. A. Wiley, R. F. Mullins, E. M. Stone, E. H. Sohn, B. A. Tucker, and C. A. Guymon, "Effect of Molecular Weight and Functionality on Acrylated Poly(caprolactone) for Stereolithography and Biomedical Applications" *Biomacromolecules*, vol. 19, no. 9, pp. 3682–3692, 2018.

[156] G. Mapili, Y. Lu, S. Chen, and K. Roy, "Laser-layered microfabrication of spatially patterned functionalized tissue-engineering scaffolds" *J. Biomed. Mater. Res. - Part B Appl. Biomater.*, vol. 75, no. 2, pp. 414–424, 2005.

[157] X. Mu, T. Bertron, C. Dunn, H. Qiao, J. Wu, Z. Zhao, C. Saldana, and H. J. Qi, "Porous polymeric materials by 3D printing of photocurable resin" *Mater. Horiz.*, vol. 4, no. 3, pp. 442–449, 2017.

[158] T. Matsuda and M. Mizutani, "Liquid acrylate-endcapped biodegradable poly(e-caprolactone-co-trimethylene carbonate). II. Computer-aided stereolithographic microarchitectural surface photoconstructs" *J. Biomed. Mater. Res.*, vol. 62, no. 3, pp. 395–403, 2002.

[159] I. K. Kwon and T. Matsuda, "Photo-polymerized microarchitectural constructs prepared by microstereolithography (μSL) using liquid acrylate-end-capped trimethylene carbonate-based prepolymers" *Biomaterials*, vol. 26, no. 14, pp. 1675–1684, 2005.

[160] S. Schuller-Ravoo, J. Feijen, and D. W. Grijpma, "Preparation of flexible and elastic poly(trimethylene carbonate) structures by stereolithography" *Macromol. Biosci.*, vol. 11, no. 12, pp. 1662–1671, 2011.

[161] S. Schuller-Ravoo, S. M. Teixeira, J. Feijen, D. W. Grijpma, and A. A. Poot, “Flexible and elastic scaffolds for cartilage tissue engineering prepared by stereolithography using poly(trimethylene carbonate)-based resins” *Macromol. Biosci.*, vol. 13, no. 12, pp. 1711–1719, 2013.

[162] B. van Bochove, S. Schüller-Ravoo, and D. W. Grijpma, “Photo-Crosslinked Elastomeric Bimodal Poly(trimethylene carbonate) Networks” *Macromol. Mater. Eng.*, vol. 304, no. 4, pp. 1–5, 2019.

[163] M. N. Cooke, J. P. Fisher, D. Dean, C. Rimnac, and A. G. Mikos, “Use of stereolithography to manufacture critical-sized 3D biodegradable scaffolds for bone ingrowth” *J. Biomed. Mater. Res. B. Appl. Biomater.*, vol. 64, no. 2, pp. 65–69, 2003.

[164] J. W. Lee, P. X. Lan, B. Kim, G. Lim, and D. W. Cho, “3D scaffold fabrication with PPF/DEF using micro-stereolithography” *Microelectron. Eng.*, vol. 84, no. 5–8, pp. 1702–1705, 2007.

[165] J. H. Shin, J. W. Lee, J. H. Jung, D. W. Cho, and G. Lim, “Evaluation of cell proliferation and differentiation on a poly(propylene fumarate) 3D scaffold treated with functional peptides” *J. Mater. Sci.*, vol. 46, no. 15, pp. 5282–5287, 2011.

[166] L. H. Sinh, K. Harri, L. Marjo, M. Minna, N. D. Luong, W. Jürgen, W. Torsten, S. Matthias, and S. Jukka, “Novel photo-curable polyurethane resin for stereolithography” *RSC Adv.*, vol. 6, no. 56, pp. 50706–50709, 2016.

[167] A. Bens, H. Seitz, G. Bermes, M. Emons, A. Pansky, B. Roitzheim, E. Tobiasch, and C. Tille, “Non-toxic flexible photopolymers for medical stereolithography technology” *Rapid Prototyp. J.*, vol. 13, no. 1, pp. 38–47, 2007.

[168] P. Lehtinen, M. Kaivola, H. Korhonen, J. Seppälä, and J. Partanen, “Producing parts with multiple layer thicknesses by projection stereolithography” *Int. J. Rapid Manuf.*, vol. 6, no. 4, p. 235, 2017.

[169] S. C. Ligon, R. Liska, J. Stampfl, M. Gurr, and R. Mülhaupt, “Polymers for 3D Printing and Customized Additive Manufacturing” *Chem. Rev.*, vol. 117, no. 15, pp. 10212–10290, 2017.

[170] J. H. Lee, R. K. Prud’homme, and I. A. Aksay, “Cure depth in photopolymerization: Experiments and theory” *J. Mater. Res.*, vol. 16, no. 12, pp. 3536–3544, 2001.

[171] S. J. Hollister, “Porous scaffold design for tissue engineering” *Nat. Mater.*, vol. 4, no. July, pp. 518–24, 2005.

[172] F. P. W. Melchels, J. Feijen, and D. W. Grijpma, “A review on stereolithography

and its applications in biomedical engineering" *Biomaterials*, vol. 31, no. 24, pp. 6121–6130, 2010.

[173] D. W. Hutmacher, M. Sittinger, and M. V. Risbud, "Scaffold-based tissue engineering: Rationale for computer-aided design and solid free-form fabrication systems" *Trends Biotechnol.*, vol. 22, no. 7, pp. 354–362, 2004.

[174] F. Rengier, A. Mehndiratta, H. Von Tengg-Kobligk, C. M. Zechmann, R. Unterhinninghofen, H. U. Kauczor, and F. L. Giesel, "3D printing based on imaging data: Review of medical applications" *Int. J. Comput. Assist. Radiol. Surg.*, vol. 5, no. 4, pp. 335–341, 2010.

[175] H. N. Chia and B. M. Wu, "Recent advances in 3D printing of biomaterials" *J. Biol. Eng.*, vol. 9, no. 1, pp. 1–14, 2015.

[176] K. W. Lee, S. Wang, B. C. Fox, E. L. Ritman, M. J. Yaszemski, and L. Lu, "Poly(propylene fumarate) bone tissue engineering scaffold fabrication using stereolithography: Effects of resin formulations and laser parameters" *Biomacromolecules*, vol. 8, no. 4, pp. 1077–1084, 2007.

[177] F. P. W. Melchels, B. Tonnarelli, A. L. Olivares, I. Martin, D. Lacroix, J. Feijen, D. J. Wendt, and D. W. Grijpma, "The influence of the scaffold design on the distribution of adhering cells after perfusion cell seeding" *Biomaterials*, vol. 32, no. 11, pp. 2878–2884, 2011.

[178] R. J. Mondschein, A. Kanitkar, C. B. Williams, S. S. Verbridge, and T. E. Long, "Polymer structure-property requirements for stereolithographic 3D printing of soft tissue engineering scaffolds" *Biomaterials*, vol. 140, pp. 170–188, 2017.

[179] F. P. W. Melchels, A. M. C. Barradas, C. A. Van Blitterswijk, J. De Boer, J. Feijen, and D. W. Grijpma, "Effects of the architecture of tissue engineering scaffolds on cell seeding and culturing" *Acta Biomater.*, vol. 6, no. 11, pp. 4208–4217, 2010.

[180] E. J. Mott, M. Busso, X. Luo, C. Dolder, M. O. Wang, J. P. Fisher, and D. Dean, "Digital micromirror device (DMD)-based 3D printing of poly(propylene fumarate) scaffolds" *Mater. Sci. Eng. C*, vol. 61, pp. 301–311, 2016.

[181] T. S. Karande, J. L. Ong, and C. M. Agrawal, "Diffusion in musculoskeletal tissue engineering scaffolds: design issues related to porosity, permeability, architecture, and nutrient mixing" *Ann. Biomed. Eng.*, vol. 32, no. 12, pp. 1728–1743, 2004.

[182] T. M. Seck, F. P. W. Melchels, J. Feijen, and D. W. Grijpma, "Designed biodegradable hydrogel structures prepared by stereolithography using poly(ethylene glycol)/poly(d,l-lactide)-based resins" *J. Control. Release*, vol. 148, no. 1, pp. 34–41, 2010.

[183] V. Karageorgiou and D. Kaplan, “Porosity of 3D biomaterial scaffolds and osteogenesis” *Biomaterials*, vol. 26, no. 27, pp. 5474–5491, 2005.

[184] A. Di Luca, B. Ostrowska, I. Lorenzo-Moldero, A. Lepedda, W. Swieszkowski, C. Van Blitterswijk, and L. Moroni, “Gradients in pore size enhance the osteogenic differentiation of human mesenchymal stromal cells in three-dimensional scaffolds” *Sci. Rep.*, vol. 6, no. 1, p. 22898, Mar. 2016.

[185] D. F. Williams, “There is no such thing as a biocompatible material” *Biomaterials*, vol. 35, no. 38, pp. 10009–10014, 2014.

[186] F. P. W. Melchels, A. H. Velders, J. Feijen, and D. W. Grijpma, “Photo-cross-linked poly(dl -lactide)-based networks. structural characterization by HR-MAS NMR spectroscopy and hydrolytic degradation behavior” *Macromolecules*, vol. 43, no. 20, pp. 8570–8579, 2010.

[187] A. K. Burkoth and K. S. Anseth, “MALDI-TOF Characterization of Highly Cross-Linked, Degradable Polymer Networks” *Macromolecules*, vol. 32, no. 5, pp. 1438–1444, 1999.

[188] J. A. Burdick, T. M. Lovestead, and K. S. Anseth, “Kinetic chain lengths in highly cross-linked networks formed by the photoinitiated polymerization of divinyl monomers: A gel permeation chromatography investigation” *Biomacromolecules*, vol. 4, no. 1, pp. 149–156, 2003.

[189] M. J. Kade, D. J. Burke, and C. J. Hawker, “The power of thiol-ene chemistry” *J. Polym. Sci. Part A Polym. Chem.*, vol. 48, no. 4, pp. 743–750, Feb. 2010.

[190] S. Ye, N. B. Cramer, and C. N. Bowman, “Relationship between glass transition temperature and polymerization temperature for cross-linked photopolymers” *Macromolecules*, vol. 44, no. 3, pp. 490–494, 2011.

[191] L. Cai and S. Wang, “Elucidating colorization in the functionalization of hydroxyl-containing polymers using unsaturated anhydrides/acyl chlorides in the presence of triethylamine” *Biomacromolecules*, vol. 11, no. 1, pp. 304–307, 2010.

[192] Autodesk, “Autodesk Standard Clear Prototyping Resin (PR48)” p. 48, 2015.

[193] H. Tobushi and J. Hu, *Advances in Shape Memory Materials*, vol. 73. Cham: Springer International Publishing, 2017.

[194] X. Luo and P. T. Mather, “Triple-shape polymeric composites (TSPCs)” *Adv. Funct. Mater.*, vol. 20, no. 16, pp. 2649–2656, 2010.

[195] A. Kuki, K. Czifrak, J. Karger-Kocsis, M. Zsuga, and S. Keki, “An approach to predict the shape-memory behavior of amorphous polymers from Dynamic Mechanical Analysis (DMA) data” *Mech. Time-Dependent Mater.*, vol. 19, no. 1,

pp. 87–93, 2015.

[196] M. Lei, K. Yu, H. Lu, and H. J. Qi, “Influence of structural relaxation on thermomechanical and shape memory performances of amorphous polymers” *Polymer* ., vol. 109, pp. 216–228, 2017.

[197] C. Azra, C. J. G. Plummer, and J. A. E. Månson, “Dynamic mechanical analysis for rapid assessment of the time-dependent recovery behavior of shape memory polymers” *Smart Mater. Struct.*, vol. 22, no. 7, 2013.

[198] Y. Li, Y. He, and Z. Liu, “A viscoelastic constitutive model for shape memory polymers based on multiplicative decompositions of the deformation gradient” *Int. J. Plast.*, vol. 91, pp. 300–317, 2017.

[199] K. P. Menard and N. R. Menard, *Dynamic Mechanical Analysis in the Analysis of Polymers and Rubbers*, no. 9. 2015.

[200] Q. Ge, X. Luo, C. B. Iversen, H. B. Nejad, P. T. Mather, M. L. Dunn, and H. Jerry Qi, “A finite deformation thermomechanical constitutive model for triple shape polymeric composites based on dual thermal transitions” *Int. J. Solids Struct.*, vol. 51, no. 15–16, pp. 2777–2790, 2014.

[201] O. A. Balogun and C. Mo, “Three-dimensional thermo-mechanical viscoelastic model for shape memory polymers with binding factor” *J. Intell. Mater. Syst. Struct.*, vol. 27, no. 14, pp. 1908–1916, 2016.

[202] G. Li, *Self-Healing Composites*. Chichester, United Kingdom: John Wiley & Sons Ltd, 2014.

[203] J. Gu, H. Sun, J. Fang, C. Fang, and Z. Xu, “A unified modeling approach for amorphous shape memory polymers and shape memory polymer based syntactic foam” *Polym. Adv. Technol.*, vol. 27, no. 9, pp. 1237–1245, 2016.

[204] C.-Q. Fang, H.-Y. Sun, and J.-P. Gu, “A Fractional Calculus Approach to the Prediction of Free Recovery Behaviors of Amorphous Shape Memory Polymers” *J. Mech.*, vol. 32, no. 01, pp. 11–17, Feb. 2015.

[205] Y. Li and Z. Liu, “A novel constitutive model of shape memory polymers combining phase transition and viscoelasticity” *Polymer* ., vol. 143, pp. 298–308, 2018.

[206] H. Lu, X. Wang, K. Yu, W. M. Huang, Y. Yao, and J. Leng, “A phenomenological formulation for the shape/temperature memory effect in amorphous polymers with multi-stress components” *Smart Mater. Struct.*, vol. 26, no. 9, p. 095011, Sep. 2017.

[207] S. Arrieta, J. Diani, and P. Gilormini, “Experimental characterization and

thermoviscoelastic modeling of strain and stress recoveries of an amorphous polymer network" *Mech. Mater.*, vol. 68, pp. 95–103, 2014.

[208] T. D. Nguyen, C. M. Yakacki, P. D. Brahmbhatt, and M. L. Chambers, "Modeling the relaxation mechanisms of amorphous shape memory polymers" *Adv. Mater.*, vol. 22, no. 31, pp. 3411–3423, 2010.